Alma Mater Studiorum · Università di Bologna

DOTTORATO DI RICERCA IN FISICA

Ciclo: XXVI

Settore Concorsuale di afferenza: 02/B3 - FISICA APPLICATA
Settore Scientifico disciplinare : FIS/07 - FISICA APPLICATA

Ph.D. Thesis

Development of an X-ray spectrometric system and feasibility tests of Silicon Drift Detector for medical and space applications

presented by:
Lucia Andreani

Coordinator:
Chiar.mo Prof. Fabio Ortolani

Advisor:
Chiar.mo Prof. Giuseppe Baldazzi

January, 2014

Introduction

My thesis work concerns X-ray spectrometry for both medical and space applications and is divided into two sections. The **first section** addresses an X-ray spectrometric system designed to study radiological beams and is devoted to the optimization of diagnostic procedures in medicine. A complete and detailed understanding of the X-ray spectrum is crucial to successfully optimizing the beam in order to obtain the best diagnostic images of the composed organic tissues with the lowest possible patient dose. The **second section** describes the preliminary tests that have been carried out on the first version of an Application Specific Integrated Circuit (ASIC), integrated with large area position-sensitive Silicon Drift Detector (SDD) to be used on board future space missions. This technology has been developed for the ESA project: LOFT (Large Observatory for X-ray Timing), a new medium-class space mission that the European Space Agency has been assessing since February of 2011. The LOFT project was proposed as part of the Cosmic Vision Program (2015-2025).

A brief description of the projects is provided below.

Part I: Development of an X-ray spectrometric system
The Project and Its Purpose

For more than a century, X-radiation has constituted a valuable tool for imaging the human body. This imaging capability is used extensively to detect and diagnose disease and injury, manage patient care and guide many forms of treatment. Since every X-ray procedure subjects the tissues of the

body to energy with an ionizing capability, specific action must be taken to minimize any associated risk to the patient. This can be achieved by eliminating any radiation exposure that is not strictly required for the formation of the images necessary to the clinical objective in question. Monochromatic X-ray beams represent an attractive solution for improving imaging and reducing patient doses. However, it remains very difficult to obtaining satisfactory levels of intensity with conventional monochromator systems [1, 2, 3]. As can be seen in figure 1.1, conventional radiology uses X-ray beams with a polychromatic spectrum that consists of a bremsstrahlung continuous component, with an energy band known only by means of filtration and kVp values, and fluorescence lines.

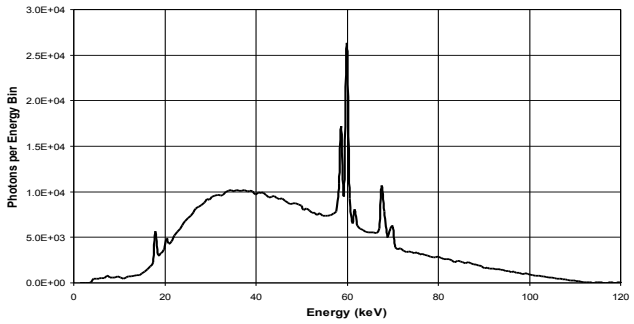

Figure 1: Spectrum from a tungsten target.

In all X-ray imaging methods, the equipment operator controls the X-ray beam administering radiation to the patient. The characteristics of the X-ray beam must be adjusted to optimize the critical balance between image quality and patient exposure.

One of the characteristics of X-radiations is fundamental in determining the quality of the radiographic image is its penetrating ability, measured in Half value layer (HVL), also known as the quality of the X-ray beam. This value indicates the thickness of material that is penetrated by one half of the radiation and is expressed in units of distance (mm or cm). It has been shown that, for any given material, the penetrating ability of an X-ray beam depends on the energy of the photons. For X-ray beams that are composed

of a spectrum of photon energies, the penetration is different for each energy. The overall penetration generally corresponds to the penetration of a photon energy located between the spectrum's minimum and maximum energy levels. This energy, designated the the X-ray spectrum's 'effective energy', is the energy of a mono-energetic beam of photons that has the same penetrating ability (HVL). The addition of filtration increases the penetration (HVL) of an X-ray beam by removing the low-energy photons. HVL values are then used to evaluate the adequacy of the filtration in order to achieve optimal imaging.

A complete and detailed understanding of the spectrum is then crucial in order to successfully use appropriate filters to optimize the X-ray beam [4]. Indeed, reducing the number of photons also contributes to reducing the dose administered to the patient in the course of the various clinical methodologies. The radiation emitted by each individual X-ray apparatus differs in terms of efficiency, anode angle and composition, inherent and additional filtration as well as the technical characteristics of the focusing electronics. It is very difficult to conduct a direct spectrometry on the diagnostic beam due to the elevated brilliance of the anode, so computer simulations can be used instead. The best methodology for simulating radiation equipment and its operations is the Monte Carlo method. However, perhaps because of their general purpose, the Monte Carlo codes [5, 6, 7, 8, 9] have been criticized in part for the fact that many operations are unnecessarily slow, thus stealing time away from more relevant activities for specific applications. A full X-ray tube simulation is a very time-consuming task because it takes into account all the physical processes involved in X-ray generation, even though most of these processes play no part in the final beam spectrum. Moreover, the EGS4, GEANT4 and MCNP4 Monte Carlo codes commonly used in medical physics use different physical models and algorithms, that were initially developed in relation to high energy [10, 11, 12]. These differences lead to a discrepancy in spectrum shape. To overcome this issue, it is possible to use many of the computing theoretical X-ray spectra that have been devel-

oped and enhanced over time [13, 14, 15]. All these models are parametric attempts to reconstruct the bremsstrahlung continuum and characteristic emission from tungsten and molybdenum anode X-ray tubes. Our idea was to use these models in order to generate the X-ray photons independently of the Monte Carlo codes, starting from parameters developed on the basis of the available X-ray beam.

The **first part** of the thesis concerns a method for reconstructing the X-ray spectra emitted from tungsten anodes used in a diagnostic field (40 - 150 keV). In addition, the simulation software for real-time reconstruction of the spectrum is also described. The focus of this section is the parametric semi-empirical model, which is able to efficiently reconstruct X-ray spectra in 'middle power' computers. The spectrum reconstruction can be divided into two main steps: the reconstruction of the spectrum shape (chapters 1,2 and 3) and the evaluation of the spectrum area (chapter 4) that physically represents the photon fluence of the X-ray beam.

- **Chapter 1** provides a state of the art review of models presented in the literature.

- **Chapter 2** presents a new method for reconstructing spectrum fluorescence lines in order to satisfactorily fit experimental and simulated data.

- **Chapter 3** describes the validation tests applied the model.

- **Chapter 4** presents a new method for evaluating the photon fluence via Air Kerma, which is capable of accurately reconstructing the spectra in terms of both spectral shape and spectral amplitude (area). This is made possible without normalization of the same area computer-generated spectra with an *in-loco* measured spectra. This chapter also goes on to outline different experimental methods of measuring the Air Kerma that can also be used during a diagnostic examination.

- **Chapter 5** describes a new detection system that is capable of performing spectrometry together with the simulation software based on the parametric semi-empirical model. A PC simultaneously performs the reconstruction of the spectrum starting from parameters developed on the basis of the X-ray beam. The goal of this work is to obtain a low-cost instrument, that can be easily installed on almost all radiological apparatuses and is capable of providing a real-time evaluation of the spectrum of any diagnostic exposure.
- **Chapter 6** describes the results obtained.
- **Chapter 7** presents the discussion and conclusion for this section of the thesis.

Part II: Feasibility tests of large area position-sensitive Silicon Drift Detectors
The Project and Its Purpose

The challenging framework of the **second part** of the thesis concerns the read out of the large area position-sensitive SDD detectors developed for use in detecting low energy X-rays (with a range of approximately 0.5 - 100 keV) for space missions and medical applications. Due to the inherent low noise of the SDD when read out with a suitable electronic device, these detectors have potential applications in the payload, where instruments capable of good energy resolution combined with position resolution and large area are needed. An ASIC designed as front-end electronics for a large area monolithic Silicon Drift Detectors (SDD) read-out has been tested with a SDD prototype possessed of a sensitive area of 4.35 $\times$ 7.02 cm^2. The SDD was designed to test both the spectroscopic and imaging performance, using different anode pitches (967 μm and 147 μm, respectively) capable of meeting the stringent constraints regarding low-noise and low-power of X-ray astronomy. The feasibility tests were performed as part of the National

Institute of Nuclear Physics (INFN) (Bologna Section) project "REDSOX - Research Drift for Soft X-rays", which is devoted to characterizing large area position-sensitive Silicon Drift Detectors for the study of X-radiation.

- **Chapter 8** describes the SDD and the specifications of the ASIC.
- **Chapter 9** presents the feasibility tests.
- **Chapter 10** outlines the experimental results.
- **Chapter 11** presents the discussion and conclusion for the second section of the thesis.

Finally, the **conclusion** of my thesis project is reported.

Contents

Part I:

Development of an

X-ray spectrometric system

Chapter 1

X-ray beam simulation

1.1 Spectrum models

Conventional radiology uses X-ray beams with a polychromatic spectrum which consists of a bremsstrahlung continuous component - with an energy band known only by means of filtration and kVp values - and some fluorescence lines, as can be seen in figure 1.1.

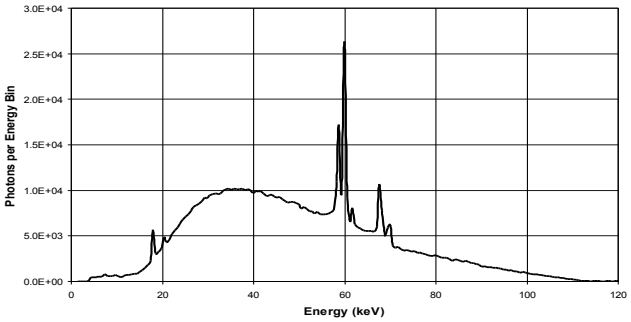

Figure 1.1: Spectrum from a tungsten target.

Monochromatic X-ray beams represent an attractive solution for improving imaging and reducing patient doses. However, it remains very difficult to obtain satisfactory levels of intensity with conventional monochromator systems [1, 2, 3].

It is probable that monochromatic beams will be the future evolution of radiology. However, this development will require arduous work and, in the meantime, a complete and detailed understanding of the spectrum is crucial in order to successfully use appropriate filters [4] to optimize the X-ray beam. Indeed, the characteristics of the beam must be adjusted to obtain the best diagnostic images of composed organic tissues with the lowest possible patient dose.

It is very difficult to conduct a direct spectrometry on the available diagnostic beam due to the elevated brilliance of the anode, so computer simulations can be used instead.

The best methodology for simulating radiation equipment and its operations is the Monte Carlo method. Many Monte Carlo codes (MCCs), originally studied for planning experiments in atomic and nuclear physics, are currently being developed to predict data for diagnostic radiology [16, 17, 18]. From the first code developed in FORTRAN (as for example EGS4), up to those in C++ (such as Geant4), simulation results have been remarkable [5, 6, 7, 8, 9].

However, perhaps because of their general purpose, the Monte Carlo codes have been criticized in part for the fact that many operations are unnecessarily slow, thus stealing time away from more relevant activities for specific applications. A full X-ray tube simulation is a very time-consuming task because it takes into account all the physical processes involved in X-ray generation, even though most of these processes play no part in the final beam spectrum. To support this idea, we carried out tests to measure the time required by a Geant4-based code to generate a set of X photons from a tungsten anode on a middle power computer. A very simple application was developed using Geant4 v9.1 on a PowerPC G4 1.25 GHz. A beam of 10^6 electrons was directed against a 1 cm thick tungsten anode at an angle of 20 degrees, drifted by a high voltage of 100 kV (usually called *kV-peak* or *kVp*). as shown in figure 1.2. All photons emerging from the anode were recorded, but the useful rays were emitted within a cone with a top angle

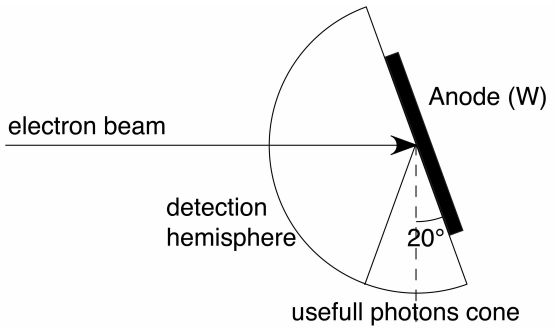

Figure 1.2: Geometrical scheme of the photon efficiency test.

of 40 degrees. The simulation ended after 20 minutes: about 12000 photons were detected, but only 2 were emitted in the desired directions.

Moreover, the EGS4, GEANT4 and MCNP4 Monte Carlo codes commonly used in medical physics use different physical models and algorithms that were initially developed in relation to high energy [10, 11, 12]. These differences lead to a discrepancy in spectrum shape.

To overcome this issue, it is possible to use many of computing theoretical X-ray spectra that have been developed and enhanced over time [13, 14, 15] can be used. All these models are parametric attempts to reconstruct the bremsstrahlung continuum and characteristic emission from tungsten and molybdenum anodes X-ray tubes.

The first model was developed by Kramers (1923) [19]. It was the first attempt to describe the spectrum of X-rays, but it was limited by many constraints and the major was that it only works for thin anodes. However this model was simple to implement and fast in computation, but not accurate.

The next major model was an evolution of the first and was proposed by Birch and Marshall in 1979 [13]. Birch and Marshall's model (B&M) was a major step forward in the description of the spectrum of X-rays because it incorporated the anode thickness contribution and a relativistic correction for the speed of the electrons. The anode absorption was modeled using the theory of Thomson-Whiddington [20]. However the semi-empirical model of B&M had the limitation to be not completely exhaustive concerning the the-

ory of electron-anode interactions, introducing ad hoc constants that should be empirically determined.
The next model was described by Tucker et al. in 1991 [14]. They extended the work of Birch and Marshall modeling parameters via the interpolation of experimental data. Although they refined the mathematical description of the K-characteristic peaks, they reported inaccuracies between the model predictions and the experimental data.
A recent model was Poludniowsky's semiempirical description of the electron-anode interactions. The model describes the theory of generation of photons very accurately by dividing the problem into two steps: electron-anode collision [21] and generation of the photon [15]. The theory described was complete and consistent and was independent of experimental data. Although this model represents the most complete mathematical description of x-ray spectra, it still needs to evaluate the two functions $P_F(u|x)$ and $P_M(u|x)$ empirically [21].
In our previous studies [22] all the models described above were tested and the model developed by Birch and Marshall (B&M) in 1979 [13] was found the fastest and the most accurate model for the purpose to simulate X-ray spectrum. This semi-empirical model was also used to implement various types of software as for example XCOMP [23] which had excellent results [24, 25]. The three required inputs for B&M model are the target angle, the tube potential and the inherent and added filtration, as detailed below.

1.2 The Birch and Marshall model

The first step in using the model is to understand what happens when an electron strikes the anode inside an X-ray tube, producing photons. It is well known that photons are mainly generated by the bremsstrahlung when accelerated electrons collide with the metal target. X-rays are produced when the electrons are suddenly decelerated upon collision with the metal target. If the bombarding electrons have sufficient energy, they can knock an elec-

tron out of an inner shell of the target metal atoms. Then electrons from higher states drop down to fill the vacancy, emitting X-ray photons with characteristic energies determined by the electron energy levels. A multiplicity of these emissions causes discrete energy lines to be superimposed on the bremsstrahlung continuum when electrons accelerated by the X-ray tube potential have energy greater than the corresponding absorption edge energy of the target material.

Birch and Marshall study these phenomena in order to reconstruct spectra generated by a tungsten target, common used in radiology.

1.2.1 Bremsstrahlung component

The model is based on the computation of the photon intensity at energy E generated by an electron traveling a distance dx inside the anode:

$$dI_\nu = Q(\frac{N}{A})\rho dx \tag{1.1}$$

where Q is a polynomial empirically determined that represents the X-ray intensity per unit energy interval per incident electron flux per atom, $\frac{N}{A}\rho$ is the number of atoms per volume unit in the target, ρ is the density of the target, N is the Avogadro's number and A is the atomic weight of the target atoms.

The intensity is obtained by integrating along the electron path to the point where the electron energy T is equal to the photon energy E, since only electrons of energy greater than E can produce a photon of this energy. Changing variables, $dx = \frac{dx}{dT}dT$, gives

$$I_\nu = \frac{\rho N}{A}\int_{T_0}^{T_\nu} Q(\frac{dT}{dx})^{-1}dT \tag{1.2}$$

where $\frac{dT}{dx}$ is the relativistic stopping power.

X-ray photons are attenuated in the anode by a factor $\exp(-\mu_\nu y)$ while emerging, where μ_ν is the linear attenuation coefficient calculated at energy E and y is the distance that the photon has to travel from its generation

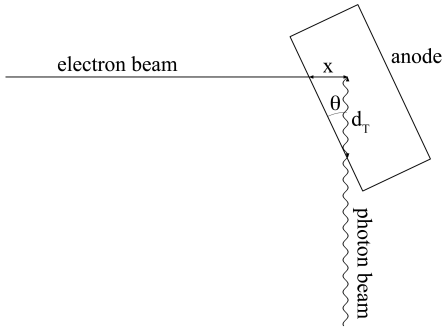

Figure 1.3: Scheme of the electrons and photons paths inside the anode. The x variable is the distance of the electron inside the anode, while d_T indicates the distance travelled by the photons to emerge from the anode. θ represents the anode slope with respect to the x-ray beam axis.

point to the anode surface. According to the geometries used in the work (see figure 1.3), the term y can be expressed as:

$$y = x \cot \theta$$

where θ is the target angle.

Birch and Marshall use the Thomson-Whiddington equation [13] to correlate the electron deepness with the energy. After penetrating a distance x into the material along the incident direction, the electron have their energy reduced to T, where

$$T = (T_0^2 - \rho C x)^{\frac{1}{2}} \tag{1.3}$$

C is the Thomson Whiddington constant that have to be tabulated for every material, ρ is the density of the target material and T_0 is the kinetic energy of the incident electrons.

Inserting the attenuation term and the term $[1 + \frac{T}{m_0 c^2}]$ to correct for relativistic effects into 1.2 gives:

$$I_\nu = \frac{\rho N}{A} \int_{T_0}^{T_\nu} (1 + \frac{T}{m_0 c^2}) Q (\frac{dT}{dx})^{-1} exp(\frac{-\mu_\nu}{\rho C}(T_0^2 - T^2) \cot \theta) dT \tag{1.4}$$

I_ν gives the energy intensity and must be divided by the photon energy to give the number of photons per energy interval and this can be used to determine the photon intensity modulation.

1.2.2 Fluorescence lines component

Birch and Marshall uses Green and Cosslett (G&C) empirical model [26], developed in 1968, to describe tungsten characteristic radiation intensity as function of the tube high voltage (*kV-peak*):

$$I_{ch} \propto (U_0 - 1)^{1.63} \tag{1.5}$$

where $U_0 = \frac{E_0}{E_k}$ and E_k is the energy required to remove an electron by the k-shell and E_0 is the electron energy.

The constant of proportionality was computed by comparison with experimental data and the energies and the relative intensities of K and L lines were obtained by the Storm and Israel Data Tables [27], compiled in 1970.

The model developed by Birch and Marshall (B&M) in 1979 [13], that was found the fastest and the most accurate model for the purpose to simulate X-ray spectrum, satisfactory fits bremsstrahlung experimental data, but does not describe the characteristic radiation with equal accuracy.

Many attempts of computing theoretical X-ray spectrum were developed and enhanced in time but, because of the relatively small contribution of characteristic radiation ($10\% - 15\%$) compared to bremsstrahlung, for electron energies of interest in X-ray diagnostic tube (10 keV to 150 keV), no rigorous computation of this component was developed in X-ray spectra major models [13, 14, 15].

This lack of an accurate description of the characteristic lines can be overcome by making specific models starting from the theoretical study of the lines formation process.

1.3 Beam geometry

To reconstruct experimental spectra, it is necessary to introduce the so-called "good geometry setup" [13, 28, 29, 30], which requires a highly collimated beam, a small field of view (FoV - typically 1 mm^2 at a source-detector distance of 1 m) with photons directed perpendicularly to the detector.

Besides, in a commercial X-ray tube beam geometry is not "good" and the beam Field of View (FoV) can be very wide, thereby changing the shape and quality of the X-ray spectra depending on the direction of emission. As stated by the different literature models, the path of the photons inside the anode is very important for the final shape of the spectrum. So the model was modified to take into account that the direction of the photons could not be perpendicular to the detector. In 1999 Bhat [31] tried to generalize the Tucker model studying the so-called off-axis contribution. Poludniowski's model also had these off-axis geometry adjustments. But these models considered only a linear collimation, i.e. a direction that is highly collimated, while the other was arbitrarily uncollimated, as shown in figure 1.4 left. Instead, to have a large FoV (figure 1.4 right) and therefore the attenuation term of the bremsstrahlung model has to be appropriately modified [22] .

When an electron enters the anode with a direction ($\widehat{p}_e$), it loses energy and emits photons in a certain direction ($\widehat{p}_\gamma$). Because photons are not generated on the anode surface, but at a depth x, they emerge through a thickness d and they will be absorbed by the anode (i.e. the anode auto-absorption) according to the attenuation law $N = N_0 e^{-\mu d}$. Thus, the core of the problem was to calculate $d = d(x, \widehat{p}_e, \widehat{p}_\gamma)$. As shown in figure 1.5 (left), with the unit vector normal to the anode ($\widehat{a}$), the two directions $\widehat{p}_e$ and $\widehat{p}_\gamma$ define two half-planes and, on each of them, the trajectories of the electron and photon draw two triangles. From figure 1.5 (right) it is clear that the two triangles have the same height (h), so:

$$\begin{cases} h = x\cos\alpha \\ h = d\cos\beta \end{cases} \quad \Rightarrow \quad d = \frac{\cos\alpha}{\cos\beta}x \tag{1.6}$$

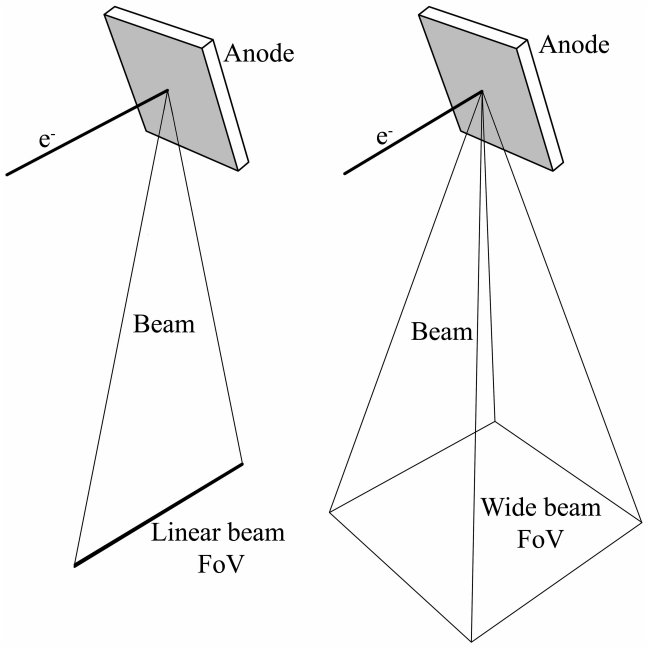

Figure 1.4: Left: shape of linear FoV described by Bath and Poludniowski. Right: the FoV shape implemented in our works.

The two cosines are the projection of the particles directions on the anode plane versor, so:

$$\begin{cases} \cos\alpha = - & \widehat{p}_e \cdot \widehat{a} \\ \cos\beta = & \widehat{p}_\gamma \cdot \widehat{a} \end{cases} \tag{1.7}$$

and substituting in equation 1.6 we find that the distance covered by the photon inside the anode is:

$$d = -\frac{\widehat{p}_e \cdot \widehat{a}}{\widehat{p}_\gamma \cdot \widehat{a}} x \tag{1.8}$$

and the photon attenuation is:

$$f(E, x, \widehat{p}_e, \widehat{p}_\gamma) = \exp\left(\mu(E)\frac{\widehat{p}_e \cdot \widehat{a}}{\widehat{p}_\gamma \cdot \widehat{a}} x\right) \tag{1.9}$$

1.3.1 Heel effect

In a X-ray tube, due to the anode auto-absorption, the photon intensity and energy change depending on the direction of photon emission. This

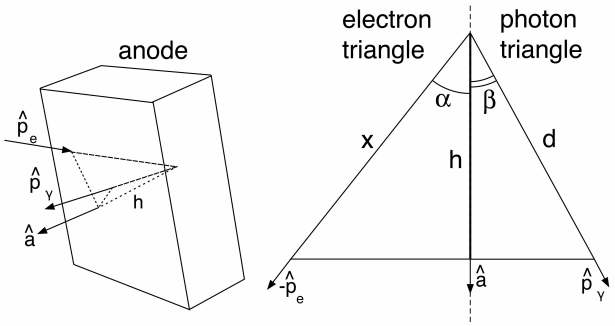

Figure 1.5: Left: geometric representation of the penetration of electrons inside the anode and the emergence of the photon. Right: scheme of interaction triangles.

phenomenon is called "heel effect". The effect on the beam quality was already incorporated within the models discussed above, so the modulation intensity was implemented as a function of the photon direction.

The model, modified according to the equation 1.9, can be used to calculate the heel effect determining the number of photons emitted in a certain direction[22] .

Defining $\widehat{p}_\gamma$ as the X-rays direction and r_γ as the x-rays path length from the source, the number of photons detected in a point of the FoV plane will be described by:

$$N(\widehat{p}_\gamma) \propto \frac{(-\widehat{p}_\gamma \cdot \widehat{n})}{r_\gamma^2} \int_0^{kVp} N(h\nu, \widehat{p}_\gamma) d(h\nu) \tag{1.10}$$

where kVp is the voltage peak of the tube, $N(E, \widehat{p}_\gamma)$ the number of photons emitted in the direction $\widehat{p}_\gamma$ with energy $h\nu$. The total number of photons detected scanning the whole FoV plane, is proportional to:

$$N_T \propto \int_{FoV} N(\widehat{p}_\gamma) d\widehat{p}_\gamma \tag{1.11}$$

Combining equations 1.10 and 1.11 it is possible to calculate the probability that a photon is emitted in the direction $\widehat{p}_\gamma$:

$$P(\widehat{p}_\gamma) = \frac{N(\widehat{p}_\gamma)}{N_T} \tag{1.12}$$

and this can be used to determine the photon intensity modulation.

1.4 Spectrum area

The spectrum area, that represents the total amount of photons in the spectrum, is another important parameter for an accurate simulation, both in terms of spectral shape and intensity. In order to calculate it, X-ray spectra major models [13, 14, 15] were normalized to the same area of literature experimental data described by Fewell in 1981 [28], used as gold standard. Due to the differences of each apparatus, in terms of efficiency, anode angle and composition, inherent and additional filtration, technical characteristic of the focusing electronics and tolerances, the relationship between the simulated area and the measured one needs to be corrected for each device. Hence the need to perform the reconstruction of the spectrum starting from parameters evaluated from the X-ray beam.

Available softwares such as XCOMP and SpekCalc, based on Birch and Marshall [13] and Poludniowski [15] models respectively, give choice to describe the spectra in terms of the number and energies of photons (photon fluence as a function of keV) or, alternatively, as the amount of photon energy deposited in a given medium, usually air (Air KERMA as a function of keV) as shown in figure 1.6.

The photon fluence (ϕ) is defined as the quotient between the number of photons (dN) crossing perpendicularly the spherical section of area da and the section itself:

$$\phi = \frac{dN}{da} \tag{1.13}$$

The unit of photon fluence is cm^{-2}.

The air KERMA quantifies the energy deposited into the medium as kinetic energy of the charged particles, usually electrons, generated by the radiation. Its unit is Grays (Gy) and it can be expressed per each photon energy, or as the integral over all the photon of the beam. It is usually evaluated as the energy transferred to the medium (dE_{tr}) per unit mass of the medium (dm)

$$K = \frac{dE_{tr}}{dm} \tag{1.14}$$

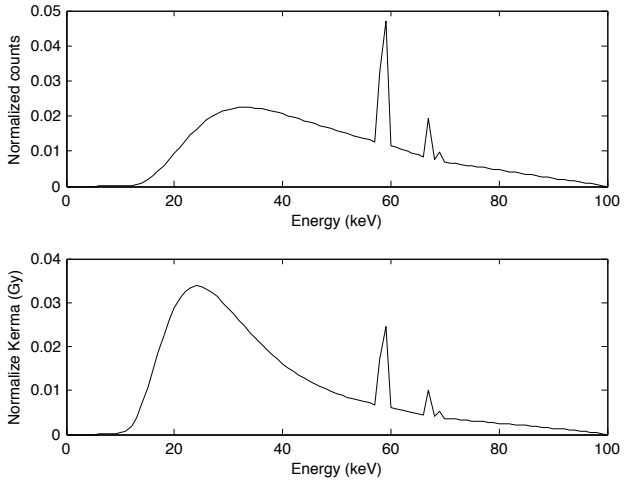

Figure 1.6: Spectrum from a tungsten target is described in terms of photon fluence as a function of keV and Air Kerma as a function of keV.

Furthermore, this approach may be useful for computing the detective quantum efficiency, DQE(f), in order to characterize an imaging system performance of X-ray detector systems [32].

The air KERMA associated with a spectrum can be calculated from the expression:

$$K = \frac{mAs}{4e\pi r^2} \int_0^{E_{max}} f(E)EN(E)(\frac{\mu_{tr}}{\rho})_{air}dE \tag{1.15}$$

where e is the electron charge, r is the distance between the tube focal spot and the ionization chamber, $f(E)$ takes into account the fraction of X-rays transmitted because of the filtration and air path length, $N(E)$ the the number of photons with energy E and $(\frac{\mu_{tr}}{\rho})_{air}$ is the mass energy transfer coefficient of air [14].

Alternatively, the exposure can be used. Exposure is defined by the ICRU as "the quotient of dQ by dm, where the value of dQ is the absolute value of the total charge of the ions of one sign is produced in (dry) air when all the electrons liberated by photons in air of mass dm are completely stopped in air" [33]:

$$X = \frac{dQ}{dm} \tag{1.16}$$

The exposure is measured in Röntgen. Exposure is the ionization equivalent of the collision kerma in air for photons and its value associated with a spectrum can be calculated as:

$$X = \frac{mAs}{4e\pi r^2} \int_0^{E_{max}} [f(E)N(E)/\psi_r(E)]dE \tag{1.17}$$

where $\psi_r(E)$ is the photon fluence per roentgen [14].

Chapter 2

Semi-empirical reconstruction of fluorescence lines

2.1 Fluorescence lines models

Many attempts of computing theoretical X-ray spectrum were developed and enhanced in time. However, due to the relatively small contribution of characteristic radiation ($10\% - 15\%$) compared to bremsstrahlung in the range from 10 keV to 150 keV, no rigorous computation of this component was developed in X-ray spectra major models [13, 14, 15]. These models satisfactorily fit bremsstrahlung experimental data, but do not describe the characteristic radiation with equal accuracy. A new method for reconstructing spectrum fluorescence lines is described in this chapter in order to satisfactorily fit experimental and simulated data.

The model developed by Birch and Marshall (B&M) in 1979 [13] is considered the fastest and the most accurate model for the purpose of simulating X-ray spectrum via Monte Carlo algorithms [22]. It uses the Green and Cosslett (G&C) empirical model [26], developed in 1968, to describe tungsten characteristic radiation as function of the tube high voltage. B&M uses also the Storm and Israel Data Tables [27], compiled in 1970, to calculate the energies and the relative intensities of K and L lines.

Another frequently used model, developed by Tucker *et al.* in 1991 [14] used the same empirical model as B&M however adjusted the exponent value (1.67 against 1.63) according to Green and Cosslett theoretical predictions [34]. Moreover, it added the term studied by Vignes and Dez (1968) [35] to take into account the depth of production of the characteristic X-rays in the thick anode and the consequent self-attenuation.

In 2007, Poludniowski [15] described tungsten X-ray spectrum basing his calculation on probability rules and dot of empirical data to obtain satisfactory results in the simulation of characteristic radiation.

This lack of an accurate description of the characteristic lines can be overcome by making specific models starting from the theoretical study of the fluorescent lines formation process.

The characteristic radiation in an X-ray spectrum corresponds to the electron transitions between two states. When the electron beam from the cathode impacts the anode, some orbital electrons are removed by collisions and can take place the so called *direct characteristic radiation* or the emission of Auger electrons; nevertheless the latter is negligible in heavy material [36]. Another process is the photoelectric absorption of bremsstrahlung photons (the *indirect characteristic radiation*). In this way the anode atoms become ionized and the vacancies may be filled by electrons from the outer shells giving rise to the emissions of characteristic radiation. In the following, a modeling of these phenomena will be described.

In order to clarify the notations, the symbol “E” refers to photon energy, “T ” is used to indicate the electron kinetic energy and “kVp” indicates the value of the X-ray tube voltage. Then the subscript “k” refers to the k-th shell (K, L, M, N) with energy E_k and the subscript “j” refers to the j-th characteristic peak (es: $K_{\alpha 1}$, $K_{\alpha 2}$, etc) with centroid energy E_j.

Spectrum models, from cited literature, considered the characteristic radiation n_j as an additional contribution to the continuum spectrum n_{br}, so

that the total spectrum n_{sp} is:

$$n_{sp}(E) = Qf(E)\left(n_{br}(E) + \sum_j \delta(E - E_j)n_j\right) \tag{2.1}$$

where Q takes into account the source-detector distance, beam collimation, tube current and exposure time (the mAs) and detection efficiency. The term $f(E)$ is the total filtration of the X-ray tube housing (inherent plus additional filtration) and depends on the photon energies. Then the Dirac delta function, $\delta(E - E_j)$, selects the peaks position in term of energy to add at the bremsstrahung continuum.

2.2 Indirect radiation

The best model of the *indirect* radiation that was analyzed here was described by Polubniowski in 2007 [15]. The amount of characteristic photons was evaluated using the fact that the ratio of direct and indirect radiation can be considered constant over a wide range of tube voltages, as stated by Dyson [36]. According to the Poludniowski model, the intensity of the indirect radiation is:

$$n_j^{ind} = p_j A_k N_{br}^{emit} \tag{2.2}$$

where p_j is the intensity of the j-th peak [37], A_k is the probability that a bremsstrahlung photon appears as indirect radiation and N_{br}^{emit} is the total number of bremsstrahlung photons emitted with energies $E > E_k$:

$$N_{br}^{emit} = \int_{E_k}^{kVp} n_{br}(T)dT \tag{2.3}$$

where n_{br} is the number of bremsstrahlung photons with energy E. This equation depends by Q that therefore does not appear in equation 2.2. Poludniowski then described the contribution of the term A_k and arrives to the final formulation of the characteristic radiation:

$$n_j = (1 + p_d)n_j^{ind} \tag{2.4}$$

where p_d is the ratio between the direct and indirect radiation. In order to have a complete reconstruction of fluorescence lines, a direct radiation model was developed.

2.3 Direct radiation

As previously stated, the other component of the characteristic radiation is the direct interaction of electrons with the anode material. This interaction could ionize the anode atoms and could generates photons with a well defined energy.

The number of ionization events (dN_o) generated by the electrons (N_i) into the anode at the depth dx can be expressed as:

$$dN_o = \frac{\rho N_A}{A} N_i \sigma_k dx \tag{2.5}$$

where $\frac{\rho N_A}{A}$ is the number of atoms per volume unit in the target, ρ is the density of the target, N_A is the Avogadro's number, A is the atomic weight of the target atoms and σ_k is the ionization cross section at the k-th shell.

Thus, to integrate this equation and determine the number of produced photons, it is necessary to choose the appropriate ionization cross section.

Some theoretical [38], semi-empirical [39] and empirical models [40, 41, 42, 43] have been proposed to evaluate the cross section for the production of atomic shell vacancies by electron impact. Most of them describe the total ionization cross-section referred to as thin target, so it is necessary to extend those models for thick anodes.

The first model, considered in the present work, was described by Casnati *et al.* in 1982 [40]. This empirical model describes the ionization cross section of atomic K-shell by electron impact and fits experimental data and theoretical results in the ranges of $6 \leq Z \leq 79$ and $1 \leq T/E_k \leq 20$.

The next considered model was described by Hombourger in 1998 [41]. This is also an empirical model to describe the K-shell ionization cross sections by electron impact, with a wide range of validity: $6 \leq Z \leq 79$ and $1 \leq T/E_k \leq 10^4$.

Empirical models have simple algorithms but are approximations and have limits of validity, as showed in the text. Anyway the two presented models are perfectly usable in the range of application of this work.

In order to have a complete evaluation of the models presented in literature, theoretical models were also considered. A major theoretical model was developed by Gryzinski (1965) [38]. It was a classical theoretical attempt to describe the ionizations of atoms by electrons, based on Coulomb scattering of electrons using exclusively parameters describing the target system. The model is based on a relatively simple analytical formula of the cross section which can be completed with a relativistic correction factor for high energies of the incident electron [44] and can be used for all shells. Although L lines are not interesting because they are at low-energy, they can also be obtained by the Gryzinski model.

To integrate equation 2.5 two ways are possible: the first considered the approximated procedure described by Birch and Marshall [13] and also used by Tucker *et al.* [14], while the other is to consider the detailed description of the electrons interactions described by Poludniowski and Evans [21].

Although the Poludniowski-Evans procedure is the most accurate from a theoretical point of view, it is constrained by a set of data specifically designed for tungsten and has a loss of generality. Thus, because one of the aims of this work is to have a fast computational model of the characteristic radiation, the Poludniowski approach results too slow [22]. On the contrary the Birch and Marshall approximation results the most simple, it does not lose generality for different materials and it is of faster computational implementation. So, in this article, the direct radiation is modelled using the B&M approach. According to the adopted procedure, the penetration of the electron inside the anode and the consequent energy lost can be expressed as:

$$dx = \left(\frac{dT}{dx}\right)^{-1} dT \tag{2.6}$$

so dx depends on the inversion of the total electron stopping power in the anode material. Replacing and integrating between E_k and kVp, the equation

2.5 becomes:

$$N_o = \frac{\rho N_A}{A} N_i \int_{E_k}^{kVp} \sigma_k(T) \left(\frac{dT}{dx}\right)^{-1} dT$$

The ionization events are then divided into the single lines and the corresponding photons are generated and attenuated by the anode while emerging. So, the direct radiation photons per electron ($N_i = 1$) is:

$$n_j^{dir} = Q f_j p_j B_k \left[\frac{\rho N_A}{A} \int_{E_k}^{kVp} \sigma_k(T) e^{-\mu_j d_T} \left(\frac{dT}{dx}\right)^{-1} dT \right] \tag{2.7}$$

where μ_j is the linear attenuation coefficient of the anode material calculated at energy E_j. The term B_k is the probability that a ionization event produces a direct radiation photon and it is strictly dependent by the ionization cross section models. Because the integration approach used is an approximation, the parameter B_k takes into account all the stochastic phenomena, including secondary scattering of the electrons, multiple scattering events leading to energy straggling, etc., that are involved in the photon production process.

The term d_T is the distance that the photon has to travel from its generation point to the anode exit surface (figure 2.1).

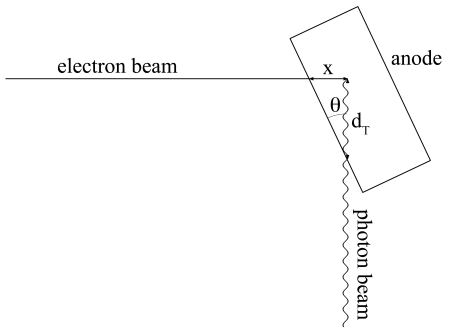

Figure 2.1: Scheme of the electrons and photons paths inside the anode. The x variable is the distance of the electron inside the anode, while d_T indicates the distance travelled by the photons to emerge from the anode. θ represents the anode slope with respect to the x-ray beam axis.

Bremsstrahlung models discussed in literature use the Thomson-Whiddington equation [13] to correlate the electron deepness with the energy. The used equation depends on the Thomson-Whiddington constants that have to be tabulated for every material. According to the geometries used in this work, the term d_T can be expressed as:

$$d_T = x \cot \theta$$

where θ is the anode angle and x is the electron deepness evaluated using the Thomson-Whiddington relation. A more general formulation of this equation is presented in [22].

Thus the number of characteristic photons is:

$$n_j = (1 + p_i) n_j^{dir} \tag{2.8}$$

where p_i is the ratio between the indirect and direct radiation contributions.

2.4 Radiation contribution evaluations

The contribution of direct and indirect radiation, and the related parameters (A_k, B_k, p_i and p_d), can be evaluated through a series of spectra experimentally acquired. The experimental spectra, as described before are affected by additional filter and setup parameters ($f(E)$ and Q) and have to be corrected prior ("back-filtration") using them. It is particularly necessary to erase the contribution of the total filtration $f(E)$. This can be done dividing $f(E)$, or f_j in the equations 2.1, 2.2, 2.3 and 2.7. This mathematical correction could be critical at energies with low photon fluence, such as after the k-edge, where the Signal-Noise Ratio of the spectra is low. This is true, but the correction at these energy intervals is so reduced that possible errors can be neglected. Nevertheless a correction is needed to have more reliable results. Then, because desired parameters are not a function of the photon energy, it is more useful to work with the integral of the characteristic photons than with individual peaks. Then, because desired parameters are not

a function of the photon energy, it is more useful to work with the integral of the characteristic photons than with individual peaks. This can be allowed by the fact that the sum of the contributions of all peaks photons emerging from the anode eliminates the dependence from p_j and maintains only the dependence from "k". So, the total number of photons will be indicated as

$$N_k = \sum_j \frac{n_j}{f_j} \tag{2.9}$$

where n_j was defined from equations 2.2, 2.4, 2.7, 2.8. With this definition,Êit is possible to find the value of the parameters:

$$(1 + p_d)A_k = \frac{N_k}{N_{br}^{emit}}$$

and this does not depend on the experimental setup (Q). As the evaluation of the term A_k is fully described by Poludniowski it is possible to evaluate p_d and consequently p_i:

$$p_d = \frac{1}{A_k}\frac{N_k}{N_{br}^{emit}} - 1 \tag{2.10}$$

$$p_i = \frac{1}{p_d} \tag{2.11}$$

The direct radiation contribution is determined from these quantities.

The last step evaluates the term B_k in equation 2.7.

To evaluate B_k it is useful to indicate the cross section contribution to the direct radiation as:

$$N_k^{ion} = \frac{\rho N_A}{A} \sum_j \left[p_j \int_{E_k}^{kVp} \sigma_k(T) e^{-\mu_j d_T} \left(\frac{dT}{dx}\right)^{-1} dT \right] \tag{2.12}$$

Depending on the model of ionization cross section (σ_k) earlier described, it could have different values according to the specific model. Combining the equations 2.7, 2.8, 2.11 and 2.12 the term QB_k is:

$$QB_k = \frac{N_k}{(1 + p_i)N_k^{ion}} \tag{2.13}$$

The correct value of QB_k can be operatively evaluated through a linear fitting of N_k as a function of $(1 + p_i)N_k^{ion}$ for every tube tension.

The term Q cannot be determined and remains an empirical parameter because there are not data available. Therefore B_k cannot be fully evaluated. The only thing that can be stated is that due to B_k being a probability it must be presented as: $B_k \leq 1$, so $Q \geq \frac{1}{(QB_k)}$. Due to Q being independent of the cross section models, in order to evaluate it, the greatest of the QB_k values was used.

Chapter 3

Validation tests

3.1 Experimental apparatus

The performances of the characteristic radiation models were evaluated with respect to their efficiency and agreement with experimental data. Each cross section model and the direct radiation photons emission (equations 2.7 and 2.8) were implemented using a computer program written in LabView language. Models were experimentally verified acquiring the spectra of a conventional X-ray tube and evaluating the measured peak areas. The source, detector and geometrical parameters used are summarized in table 3.1.

In order to compare X-ray spectra simulations with experimental data, the simultaneous acquisition of spectra, and the waveforms of the high voltage and anode current taken out from the inverter generator of the radiological system was necessary. The system used for the acquisition of the parameters is represented by the following block diagram 3.1.

From the figure it can be easily seen the two acquisition channels of the waveforms and the spectrometer, both in operation simultaneously. The following are general descriptions of them.

Tube :	MHF160
Generator :	CHF 225 kV, 1.6kW
Manufacturer :	Gilardoni spa,
	Mandello del Lario (LC), Italy
Anode angle :	20 deg
Total filtration :	0.8 mmBe
Nominal focal spot size :	0.4 mm
Current :	1 mA
Emission time:	620 s
Tension range (kV) :	90, 100, 110, 120, 130, 140, 150
Detector :	GLP-10180/07-P
Manufacturer :	Ortec,
	Oak Ridge (TN), USA
Energy resolution (FWHM) :	Measured, (Shaping)
at 26.34 keV, ^{241}Am :	270 eV, ($6\mu s$)
at 59.54 keV, ^{241}Am :	360 eV, ($6\mu s$)
at 122 keV, ^{57}Co :	480 eV, ($6\mu s$)
Preamplifier :	7611 Spectroscopy Amplifier
Manufacturer :	Silena spa,
	Rome (RM), Italy
MCA model :	MCS8000A, 1024 channels
Software :	ADMCA v2.0.0.5
Manufacturer :	Amptek Inc,
	Bedford (MA), USA
Live time :	600 s
Dead time :	$< 1\%$
Source-detector distance :	(558 ± 2)cm Air

Table 3.1: List of the experimental setup parameters of the spectra acquisitions.

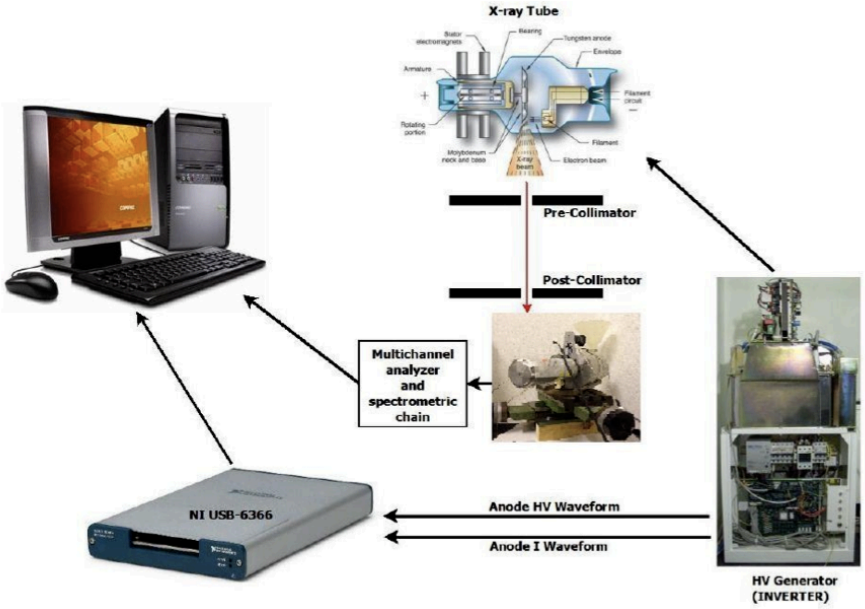

Figure 3.1: Acquisition diagram block.

3.1.1 High voltage waveform channel

The acquisition line of the waveforms is constituted by an inverter generator (High Voltage generator), a resistive divider, an Analogic to Digital Converter (ADC), and a data processing program written using LabView (version 10, National Instruments, Austin, TX, USA). The waveforms of the high voltage and the anode current are taken directly from the resistive divider from the inverter generator that produces an output voltage proportional to its input voltage. As shown in figures A.4 and A.5 in the appendix A, the high voltage (0 to 200 kV) was mapped in a range of 0V to 5V, in order to have 40kV per Volt in output. As before, the current was mapped from 0 to 1000mA to 0V to 5V, in order to have 200mA per Volt in output. The outputs of the inverter generator were directed to the resistive divider to make them readable from the ADC as previously described. The waveforms were then sampled by the National Instruments NI USB-6366. A buffer is present Inside the ADC, since data enters with a speed greater than the speed

at which the USB output works. The buffer stores the input data until the memory is full and then downloads them to the PC via the USB 2.0 output. The main features of the ADC are:

- 8 simultaneous analog inputs at 2 MS/s/ch with 16-bit resolution; 16 MS/s total Al throughput;
- onboard memory (32 or 64 MS) to ensure finite acquisitions, even with competing USB traffic;
- two analog outputs, 3.33 MS/s, 16-bit resolution, range of ±10 V;
- 24 digital I/O lines (8 hardware-timed up to 1 Mhz);
- four 32-bit counter/timers for PWM, encoder, frequency, event counting, and more;
- advanced timing and triggering with NI-STC3 timing and synchronization technology.

Two of the 8 analog inputs are used for the high voltage waveforms and the anode current. The sampling rate was set at 100 kS/s. At this frequency, waveforms fluctuations, due to the action of the feedback loops, are widely being oversampled, since the time constant is 0.1 ms.

3.1.2 Spectrometric channel

A reference set of spectra was taken with an ORTEC high purity germanium (HPGe) planar detector (size of $10 \times 10 \times 10 mm^3$ with thin beryllium window) characterized by the efficiency calibration curve shown in 3.2 and with standard NIM electronics for pulse shaping and multichannel analysis. The spectrometric system was accurately calibrated, in terms of energy, with γ reference sources.

Spectra was obtained placing the HPGe detector at 5.58 m of distance from the focal spot of the X-ray tube and collimating the beam. The collimation system consisted of the two 2 mm diameter pre-collimators composed

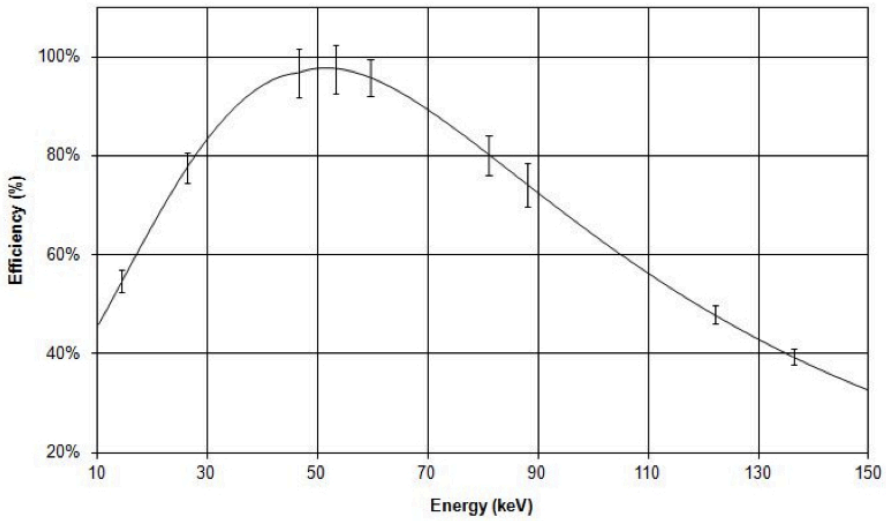

Figure 3.2: HPGe detector efficiency calibration curve.

of a Pb block 3 mm thick, a 1 cm diameter central collimator of a Pb block 8 mm thick and a sandwich post-collimator. The system consisted of different layers composed of Cu, Sn and Pb 9 mm thick with a diameter that decreased from 2 mm to 0.8 mm.

3.2 Acquisition data

In order to avoid ripple adjustments of the tube voltage and current, the beam was active for a time of 620s. The detection started after 10s after the beam activation and ended 10s before the deactivation. An additional time of 30s passed between two subsequent measures in order to avoid spectra modification due to anode temperature effects. Together with the experimental acquisitions of the spectra, simulations using different cross section models were performed.

The first test on the experimental spectra concerned the determination of the direct and indirect radiation contributions described in the previous section, and the evaluation of the parameters Q, A_k, B_k, p_d and p_i. The direct

radiation model was then used to test its prediction power of the peaks areas.

Then the uncertainties of the results were estimated by evaluating the fit parameters using the least square method and by applying the error propagation to the model equations.

Model accuracy was then tested by comparing the measured net area of the peaks with the corresponding values provided by the models, sampled to 1 keV. The comparison was made using the root mean square deviation (RMSD). The model with the lowest RMSD value was chosen as the most accurate. To have an other validation of the models effectiveness, the spectra taken from literature (Fewell *et al.* [30, 28] and Bath-Pattison [29]) were compared with the model described. Bremsstrahlung spectrum was simulated using the Birch&Marshall model, while the K-lines were evaluated using the most effective cross section model in equation 2.8.

Chapter 4

Spectrum area evaluation

4.1 The X-ray Air Kerma

In order to reliably and accurately reproduce the available X-ray spectrum, the HV waveform was sampled at frequency f and a simulation was created for each time value of the voltage. At the end of the period, all the spectra were added together to obtain the total spectrum. The total photon fluence of the real spectrum was measured with a high-resolution HPGe detector ORTEC cooled with liquid nitrogen and compared to the simulated spectrum. The relationship between two values was used by the software, written in LabVIEW, to reconstruct the X-ray spectrum.

Due to the differences of each apparatus presents in terms of efficiency, anode angle and composition, inherent and additional filtration, technical characteristic of the focusing electronics and tolerances, the relationship between the simulated area and the measured area must be corrected for each device. Alternative methods capable of directly measuring parameters are described later in this chapter.

The shape of the spectrum depends on the sampling frequency f and other model parameters. A value of $f\,60kS/s$ has been experimentally identified as good for the three different X-ray apparatuses studied. An anti-aliasing filter with a frequency of $20kHz$ and a slope of $12dB/octave$ was added. This fil-

ter also functions to reduce the wide fluctuations in both the waveforms (see Figure 4.1). Most of these fluctuations are due to the electric noise transmitted or irradiated from the inverter oscillator at $12kHz$. In fact, the noise can be greatly reduced by using the Fourier analysis and cutting harmonics multiples of $12kHz$. We calculated a standard deviation for these reduced fluctuations of 6% for the kV and 18% for the mA. As Ia increases, the fluctuations decrease. This is typical behavior for a clinical X-ray apparatus that functions in a limited operational range. Despite this, the tube output, measured in mGy with the CAPINTEC dosimeter, is stable within only 2%.

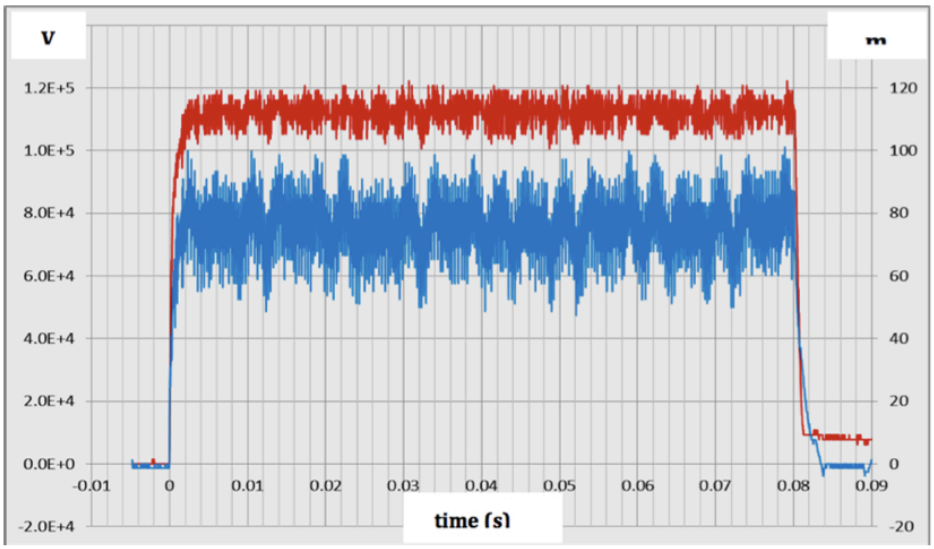

Figure 4.1: One of the X-ray tube anode high voltage waveforms (red) and anode current waveforms (blue) acquired with the NI USB-6366 digitizer during measuring (120 kVp, 100 mA, 80 ms). The characteristics of this X-ray apparatus are summarized in Table 4.1.

The spectrum area was then calculated by evaluating the total photon fluence of the real spectrum using the Air KERMA measurements for each X-ray beam. The total Air KERMA (mGy) can be calculated from the number of photons per Energy bin with the expression [14] :

$$K = \frac{mAs}{4e\pi r^2} \int_0^{E_{max}} EN(E)(\frac{\mu_{tr}}{\rho})_{air} dE \tag{4.1}$$

where e is the electron charge, r is the distance between the tube focal spot and the ionization chamber, $N(E)$ is the the number of photons per Energy bin E and $(\frac{\mu_{tr}}{\rho})_{air}$ is the mass energy transfer coefficient of air [14].

The total air KERMA of the available diagnostic beam can be easily measured with a calibrated ionization chamber of the kind commonly used in quality assurance, under conditions of electron equilibrium. It can be experimentally obtained by interposing an equivalent medium of sufficient thickness between the tube focal spot and the ionization chamber. Under these conditions the gas-produced electrons that are lost to the wall medium are compensated for by electrons produced in the medium and absorbed in the ionization chamber. We used the PM30 (CAPINTEC Inc., USA), calibrated as a secondary reference with ISO X-ray series (LAT n. 065), to provide a traceable standard.

The relationship between the total Air Kerma measured and the corresponding simulated amount was used to calculate the total photons fluence of a real spectrum through the simulated one normalized at 1 photon fluence.

Two different methodologies for efficiently reconstructing the X-ray beam fluence spectrum in a personal computer were tested and compared. The characteristics of the X-ray tube used in this experiment are listed in Table 4.1.

DC tube	RTM 101 HS, IAE Milan (Italy)
anode material	RTM (Rh, W, Mo)
anode angle	12.5 deg
nominal focal spot size	1.3 mm
tension frequency	12 kHz
inherent filtration	1.5 mmAl at 150 kVp

Table 4.1: Tube characteristics and settings used in the total Air Kerma measurement.

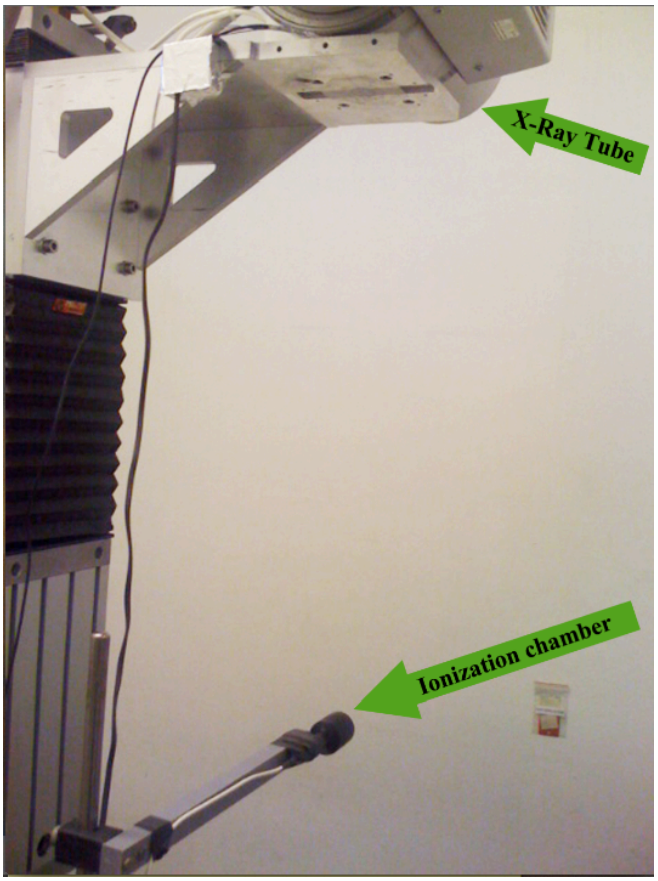

Figure 4.2: The Capintec ionization chamber used to measure the total Air Kerma of the available diagnostic X-ray beam.

4.2 Tube output as a function of voltage

The first method for reconstructing the X-ray beam fluence spectrum of the available X-ray beam is based on the measuring the HV and Ia waveforms taken out from the X-Ray tube generator, as indicated in Fig. 4.3.

To avoid real-time tube output measurements, these waveforms were used to fit the $mGy/(mA \cdot min)$ with a polynomial curve as a function of kV.

The focal spot-detector distance was $(66.7 \pm 0.5)cm$. In order to ensure the correct data, the tube output was analyzed in the range of diagnostic interest (high voltage from 40 kVp to 140 kVp and additional filtration from 0 mm Al to 4 mm Al), thereby simulating different radiological conditions. The data consisted of a collection of 40 acquisitions taken every 10 kVp from 50 kVp to 140 kVp, with 40 mAs (125 mA, 320 ms) of anode current and time and an additional filtration of 0, 2, 3 and 4 mm of high purity aluminum. The air KERMA data were then normalized to $mGy/(mA \cdot min)$ at 1 m from the focal spot. The output intensity (I) decreases with the square of the distance (d) from the focal spot according to the relationship:

$$I_2 = I_1(\frac{d_1}{d_2})^2 \tag{4.2}$$

The high voltage and anode current waveforms from the inverter generator were acquired simultaneously. They were sampled and digitized using a National Instruments NI USB-6366 (National Instruments Inc., Austin, TX, USA). The average values were calculated and the total Air KERMA values were fitted as a function of the measured kV with a third degree polynomial curve, as established in [32]. The standard deviation of the residuals was then used as an estimate of the uncertainty for this experiment.

The manufacturing companies consider the method of taking the high voltage and anode current waveforms directly from the radiological systemÕs inverter generator to be excessively intrusive. In order to avoid intervening directly on the radiological system hardware, which could cause problems with the apparatuses that are already installed, an alternative technique

using silicon PIN diode detectors was developed.

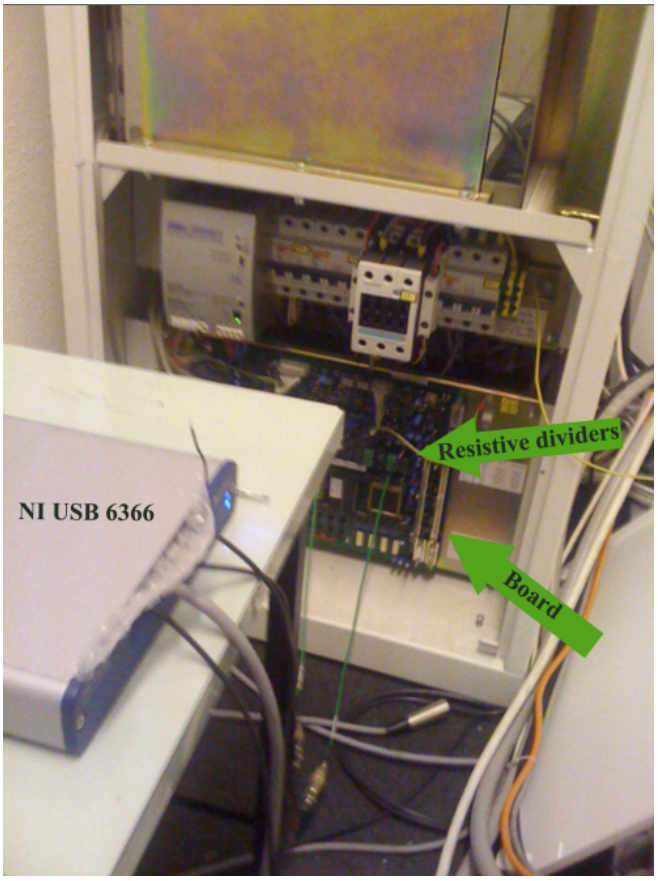

Figure 4.3: The high voltage and anode current waveforms are taken directly from the radiological system's inverter generator.

4.3 Silicon PIN diode detectors

During the last decades, there has been a great deal of effort dedicated to developing silicon PIN diodes applications for medical use [45, 46, 47] and radiological imaging in particular, due to their low production costs, high stability in the face of radiation damage and the possibility of growing large active areas. These properties together with their cost effectiveness make these devices useful as small dosimeters for rapid and real-time dose evaluation.

Two different diode responses for measuring the X-ray total air KERMA are presented in order to calculate a dosimetric parameter directly from the available X-ray beam. A naked Si-PIN diode and a Si-PIN diode + CsI(Tl) scintillator were tested and compared as radiological dosimeters. Other authors [48] have analyzed the spectrometric capabilities of Si-PIN detectors, by studying energy resolution and linearity at different energy levels. However, in order to achieve a rapid dosimetric system that can be used with commercial X-ray tubes, the detector properties must be analyzed by exposing it to a polychromatic X-ray field as well. For these reasons, we exposed diodes to different X-ray spectra, that had been obtained with different high voltages and different thickness of aluminum filtration to simulate varying radiological conditions. Both of the detector outputs were calibrated using a secondary reference standard (CAPINTEC PM 30 dosimeter), so that the dose and the energy dependence of the detectors could be analyzed and discussed in the range of radiological interest (tube voltage: 40-140kVp and additional filtration: 0 mm Al to 4 mm Al).

The basic structure of a PIN diode is shown in figure 4.4.

The measurement of radiation is based on the production of electron-hole pairs during the interaction of radiation with the detector material and the further collection of charges. There PIN diodes can be operated in two different ways: in photovoltaic mode, without the application of bias voltage, and in photoconductive mode, with the application of a reverse bias voltage to create a depletion zone inside the intrinsic region [45]. For the purposes of

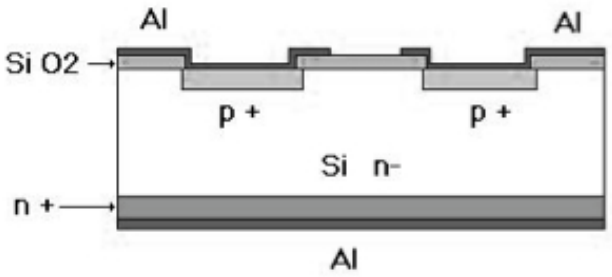

Figure 4.4: Scheme of a semiconductor PIN diode.

this research, a reverse voltage of 2.5V was applied in order to increase the collection efficiency of the charges with a greater thickness in the depletion region. Electrons and holes formed within this region drift under the influence of the corresponding electric field, and current is measured through an external circuit that is connected across the junction. When in photoconductive mode, the PIN diodes have the disadvantage of providing a less energetic dynamic range. To overcome this difficulty, an appropriate resistance value was selected in the feedback of the operational amplifier. As is true of any semiconductor diodes, PIN diodes are very sensitive to light: the detection efficiency is approximately 100% for photons of even a few keV, decreasing to approximately 2% at 60 keV for a 300 μm thick PIN diode [49].

In order to enhance the detector efficiency in the energy range of interest [50], a small-sized inorganic scintillator CsI(Tl) coupled with the silicon PIN diode was tested. Scintillator crystals take the energy deposited by an X-ray and convert it into light. When coupled to a silicon PIN diode, these scintillations can be converted into current signal that can be electronically analyzed to provide information about the photon fluence of the incident radiation. The scintillation mechanism depends on the energy states, which are determined by the crystal lattice of the Cesium Iodide. In order to enhance the probability that a visible photon will be emitted during the de-excitation process, small amounts of Tallium impurity are added to the Cesium Iodide. As a result, energy states are created within the forbidden

gap (the intermediate band between the valence and the conduction bands) that the electron can use to de-excitate back to the valence band. One important consequence of luminescence through activator sites is the fact they crystal can be transparent to the scintillator light [49]. This scintillation light is collected, converted to electrons by a silicon PIN photodiode.

Two small silicon PIN diodes of $2.7 \times 2.7mm^2$ were used, one coupled with a 5 mm thick CsI(Tl) crystal. A very thin layer of transparent epoxy resin was used to attach the polished CsI(Tl) to the PIN diode. The diodes were selected for a dark current of approximately $2nA$.

The total air KERMA was also acquired using an air ionization chamber (CAPINTEC) calibrated (LAT n. 065) with an ISO X-ray series to obtain a traceable secondary standard. Images of the dosimeter prototypes are provided in figures 4.5 and 4.6, in both configurations.

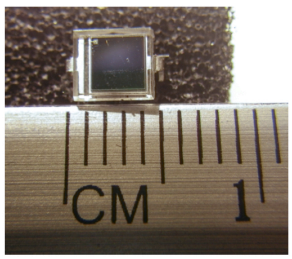

Figure 4.5: An image of the Si-PIN diode detector .

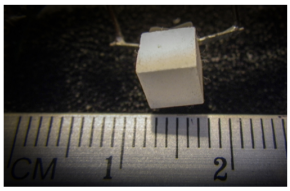

Figure 4.6: An image of the Si-PIN diode + CsI(Tl) scintillator detector.

The X-ray tube used for this research is a diagnostic type with an inverter generator. Its nominal capabilities are 150 kVp anode high voltage and 800 mA anode current. The characteristics of the X-ray tube are outlined in Table 4.1. All of the internal filters were removed so the inherent filtration was the

only form of filtration present and we were able to have full control over all effective additional filtration. The anode HV and current were acquired during measuring.

This method of taking two sets of measurements was fundamentally aimed at comparing how efficiently the detectors were able to evaluate the KERMA. The diode was mounted on a custom-made electronic readout implementing a classical transimpedance amplifier circuit (figure 4.7) to read the X-ray output and arranged in a charge sensitive configuration to extend the dynamical range. The same circuit specifically assigned to this purpose was used for both detectors.

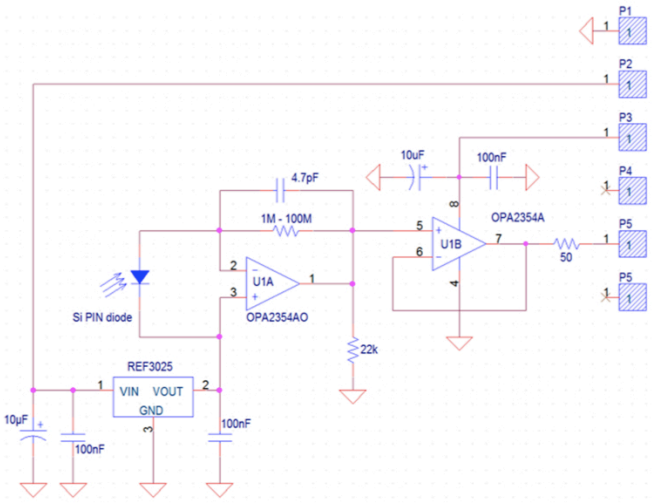

Figure 4.7: Schematic of transimpedance detector readout

Due to voltage ripple, to obtain an accurate characterization of the rate of KERMA, the tension waveform was measured using a current preamplifier applied to the diode and the signal was digitalized using the NI USB-6366. The calibration measurements for the Si-PIN and the Si-PIN + CsI(Tl) were performed at different tube voltages (from 40 kVp to 140 kVp) and anode currents (from 40 to 630 mA or until detector saturation) at the tube emission time of 63 ms. An additional aluminum filtration with thicknesses of 0, 2, 3 and 4 mm of was used to evaluate the effects of beam quality on detector

response.

The tube-detector distance was set at (75.2 ± 0.5)cm and the room temperature at 24°C. The diode response (mVs) was calculated as the area of the measured waveform. The data were then normalized at a distance of 1m from the focal spot size. The calibration between the total air Kerma (mGy) and the diode output (mVs) was calculated. The plots were fitted with a least-squares linear method and the uncertainties regarding the calibration parameters were evaluated [51].

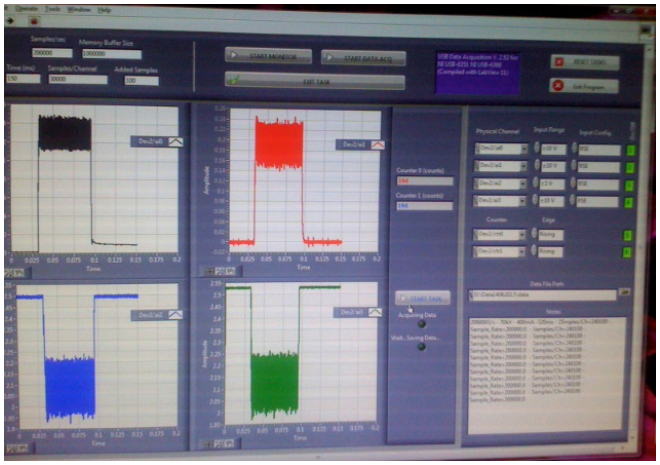

Figure 4.8: The high voltage and anode current waveforms and the diode outputs were acquired simultaneously and visualized on a personal computer.

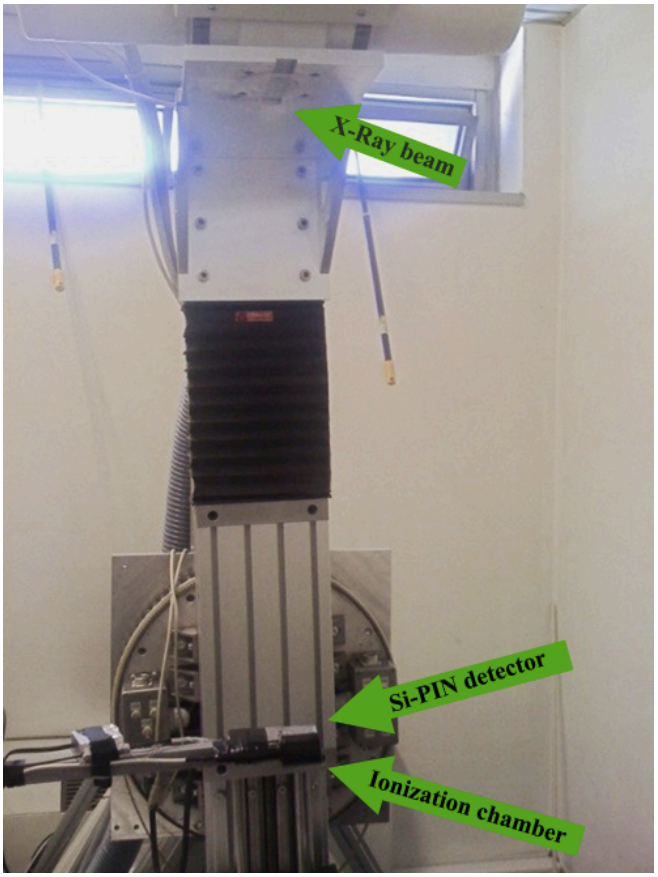

Figure 4.9: For the calibration measurements, the diode radiation detector and Capintec ionization chamber were positioned at the same distance from the X-ray tube focal spot.

Chapter 5

Real time spectrometry

5.1 Real time detector system

The X-ray spectrum simulation software, which is based on the parametric semi-empirical model and the previously described methods of reconstructing the spectrum area via the Air Kerma, was written in LabView. In clinical practice, this software can be used to provide a real-time evaluation of the spectrum of any diagnostic exposure that occurs.

The methodologies developed and tested in this research are capable of measuring model parameters directly from the available X-ray beam and the high voltage generator and can easily be applied to almost all existing radiological apparatuses. During the diagnostic examination, a PC runs the reconstruction of the spectrum, starting from experimental parameters. This makes it possible to design composed filters in a way that limits the energy bandwidth and results in higher quality images. The system can also implement a microchip-equipped patient dosimetric card in which the anatomic region in question, FOV dimension and focal spot-patient distance (which can be automatically measured to calculate the skin air KERMA) can be automatically registered together with the photon fluence spectrum. This collection of information guarantees that the patient dosimetry is accurate and the diagnostic exam is precisely repeatable. In order to fully employ

the method, it is necessary to develop an apparatus (Compton camera) that periodically verifies the calibration of the online spectrometer. This can be achieved by reading the X-ray beam spread that results from the Compton effect at a precise angle and reconstructing it.

5.2 The software tool

The reconstruction algorithm of the spectrum was originally based on the Birch and Marshall semi-empirical model. However, this model was subsequently changed and improved in the multiple ways described in the first three chapters to meet the demands of the detection system and to implement new features.

The spectrum area, which physically represents the X-ray beam photon fluence was calculated by evaluating the total photon fluence of the real spectrum via the Air Kerma, as described in chapter 4. In order to obtain a real-time measurement of the air KERMA during diagnostic examination, information from two alternative sources is needed (see fig. 5.1). The most important sources are the waveforms of high voltage (HV) and anode current (Ia) generated by the radiological system's inverter (see fig.5.1 right and Fig. 5.2). They can be directly acquired from the inverter using the NI USB-6366 sampled, digitalized and passed on to the software. The PC then runs a reconstruction of the spectrum during the diagnostic examination starting from these experimental parameters and the previously estimated polynomial fit coefficients of the X-ray tube output $mGy/(mA \cdot min)$ as a function of kV, as described in section 4.2. This method is very precise but, as previously mentioned, it is difficult to carry out and is too intrusive for the hardware. In order to avoid intervening in the radiological system hardware, which can cause problems for the apparatuses that have already been installed, we developed and validated a second innovative and alternative method. This method, based on a detection system that can be installed inside the collimators group, works by intercepting a small outer section of the beam

(see Fig. 5.1 left and Fig. 5.3). The resulting information is used to calculate parameters for a spectrum photon fluence simulation.

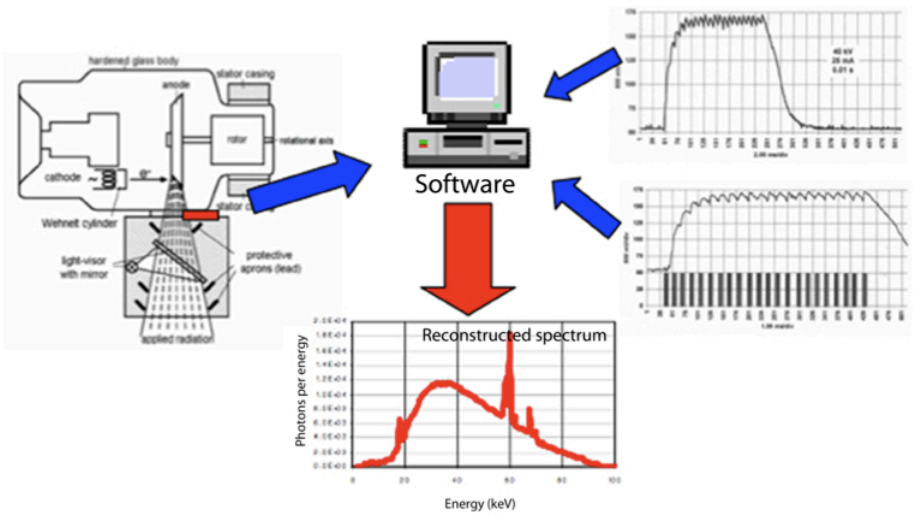

Figure 5.1: A schematic representation of the method used for evaluating X-ray beam parameters.

The detection system, which was composed of 4 detectors to optimize performance in the energy range of interest, was developed and tested (fig. 5.4 and fig. 5.5). The experiment employed two bare Si-PIN diodes and two Si-PIN diodes coupled to a 5 mm-thick CsI(Tl) scintillator to increase efficiency while reducing dynamical range. The diodes were mounted on a classical transimpedance circuit (fig. 4.7) to read the X-ray output and placed in a charge-sensitive configuration to extend the dynamic range. The PC runs the reconstruction of the spectrum during beam emission starting from the diode output acquired using the NI USB-6366 and the calibration curves (mGy as a function of diode output ($mV \cdot s$)) previously calculated for the available X-ray tube, as described in section 4.3.

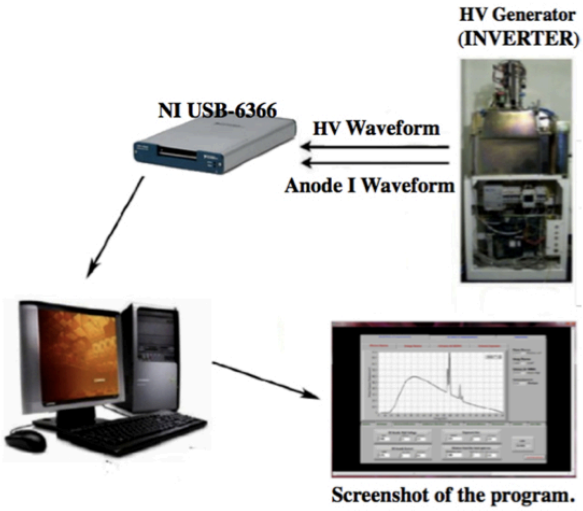

Figure 5.2: A schematic representation of the method used for evaluating the X-ray Air Kerma, based on tube tension and the anode current waveform measurement.

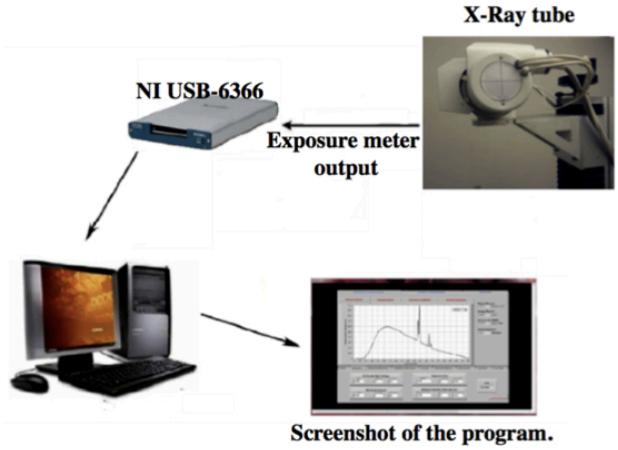

Figure 5.3: A schematic representation of the method used for evaluating the X-ray Air Kerma, based on a custom-designed exposure meter system mounted at the exit window of the X-ray tube located inside the collimator system.

Figure 5.4: An image of the custom-designed exposure meter system.

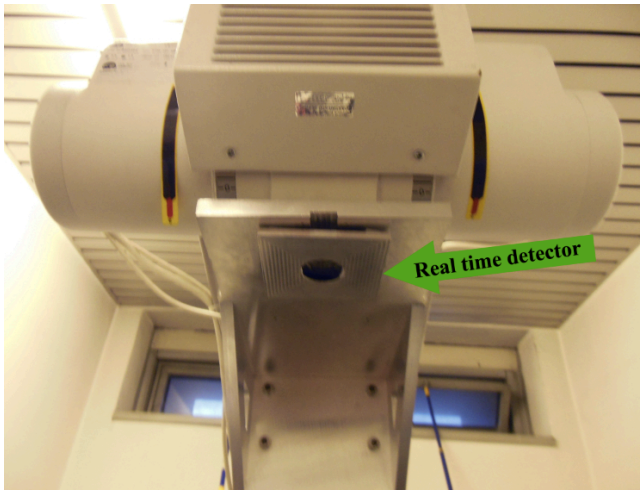

Figure 5.5: An image of the detection system mounted at the exit window of the X-ray tube.

5.3 Portable Compton Selection Chamber

As previously mentioned, it is not feasible to carry out a spectrometry of the diagnostic X-rays beam on-site because the anode brilliance is always too high to be read by any spectrometric detector. To overcome this difficulty in periodically verifying the calibration of the real-time spectrometer, we used a portable detection system based on a miniaturized Compton selection chamber (CSC) associated with a Si-PIN detector, as developed by Baldazzi in 2004 [52]. The primary X-rays beam strikes a suitable graphite target and photons scattered inside an angle of ($90° \pm 1.5°$) are detected. By reducing the photon intensity by a factor of $10^9 - 10^{11}$, it thus becomes possible to obtain a spectrometric analysis. The Compton scattering spectrometer is a thick (0.8 mm) Si-PIN detector. A specially formulated software algorithm was used to reconstruct the scattered spectra. This algorithm provides a reconstruction of the primary spectra using a simplified, experimentally determined scattering matrix that describes scattering processes for a polychromatic X-rays beam. Full details regarding the design, functionalities and reconstruction algorithm of the Compton Camera prototype are presented in [52].

5.4 Experimental validation

The reconstructed spectra was validated by acquiring a reference set of spectra from a conventional X-ray tube and comparing them with a measured set of spectra. The characteristics of the X-ray tube used for this are listed in table 4.1, while the characteristics of the ORTEC high purity germanium (HPGe) detector and the NIM electronics are listed in Table 3.1. The spectra in question were obtained by placing the HPGe detector at a distance of 4.80m from the focal spot of the X-ray tube and collimating the beam. The collimation system consisted of two 2 mm-diameter pre-collimators composed of a 3 mm-thick Pb block, a 1-cm diameter central collimator composed of an 8 mm-thick Pb block and a post-collimator sandwich. The system consisted of different layers composed of 9 mm-thick Cu, Sn and Pb with a

diameter that decreased from 2 mm to 0.8 mm. The experimental spectra were acquired at an anode current of 320 mA, an emission time of 100 ms and a high voltage of 80, 100 and 120 kVp. Model accuracy was then tested by comparing the measured net area of the spectra to the corresponding values provided by the software. The comparison was carried out using the root mean square deviation (RMSD).

Chapter 6

Results

6.1 Fluorescence lines models validation

The measured spectra are shown in figure 6.1 where, for clarity, only a sample are plotted: 90, 110, 130, 150 kV. The experimental energy resolution was evaluated to be $0.5keV$.

The peak areas and the total bremsstrahlung photons measured from experiments are showed in table 6.1.

	$(E_j \pm 0.5)$ keV			
kVp	58	59.5	67	69
90	193	339	112	—
100	306	695	279	90
110	663	1328	264	193
120	1091	2065	690	163
130	1687	3092	909	126
140	2335	4159	1366	399
150	2903	5449	1725	209

Table 6.1: Experimental peak area (n_j).

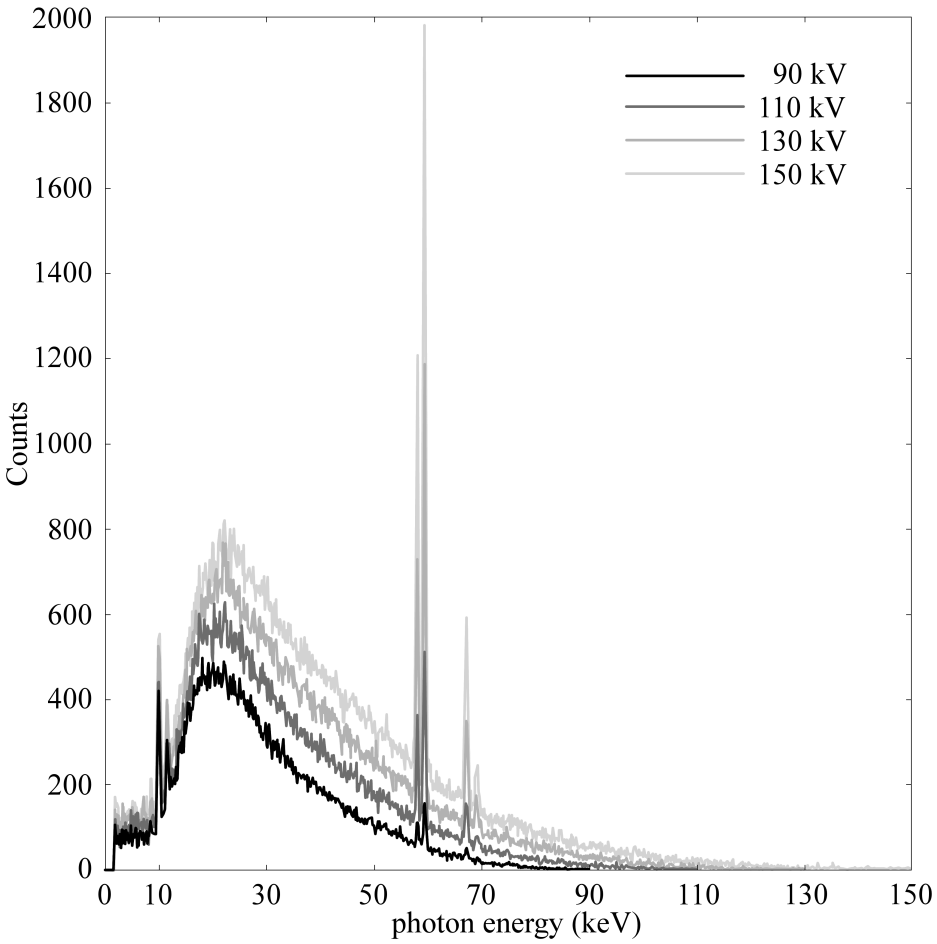

Figure 6.1: Example of the spectra measured.

Unfiltered peak area and summation is showed in table 6.2.

	$(E_j \pm 0.5)$ keV					
kVp	58	59.5	67	69	N_k	N_{br}^{emit}
90	221	388	127	—	736	1061
100	351	795	317	102	1565	2526
110	760	1520	300	219	2799	4962
120	1251	2364	784	185	4583	8370
130	1934	3539	1033	143	6649	12243
140	2677	4760	1552	453	9442	16607
150	3328	6236	1960	237	11762	22102

Table 6.2: Unfiltered experimental peak area (n_j/f_j). The last columns are the total number of peak photons (N_k) and the total back-filtered photons emitted with energy $E > 69.52$ keV (N_{br}^{emit}).

Figure 6.2 shows the correlation between the number of photons with energy $T > 69.52$ keV (K-edge of tungsten) and the number of photons emitted as K-peaks.

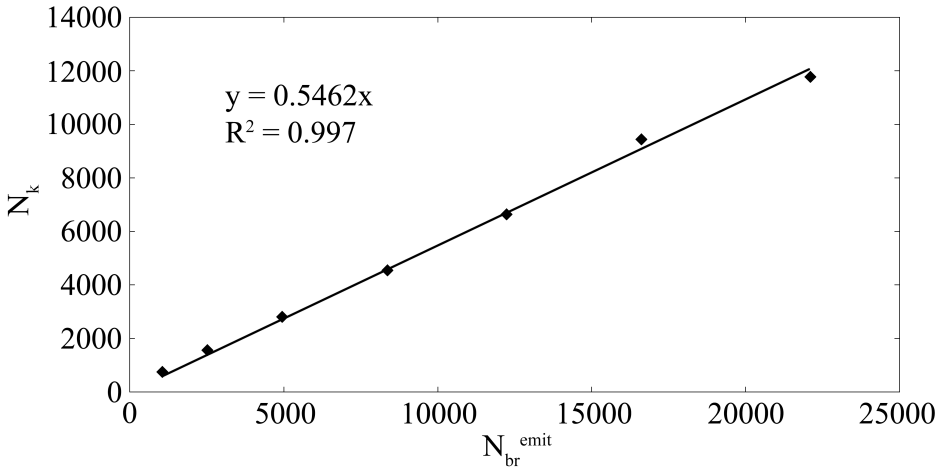

Figure 6.2: Plot of the number of photons with $T > 69.52$ keV (N_{br}^{emit}) and the N_k.

The figure shows an excellent linear correlation in agreement on what was

stated by Dyson [36] and Poludniowski [15]. On the basis of these results, and estimating the value of $A_k = 0.36$ for K-edge tungsten from Poludniowski, it is possible to evaluate the values of p_d and p_i as shown on table 6.3.

$(1 + p_d)A_k$	p_d	p_i
0.546 ± 0.007	0.50 ± 0.02	1.98 ± 0.08

Table 6.3: Values estimated for $(1 + p_d)A_k$, p_d and p_i.

The calculated value of p_i is then used to estimate the number of peak photons of direct radiation using equation 2.8 as shown in table 6.4.

kVp	$N_{k-dir} \pm 4\%$	$N_{k-ind} \pm 4\%$
90	247	490
100	524	1040
110	938	1860
120	1540	3050
130	2230	4420
140	3160	6280
150	3940	7820

Table 6.4: Number of direct (N_{k-dir}) and indirect radiation (N_{k-ind}) as a function of the tube tension estimated using equations 2.8, and 2.4 and the parameters estimated for p_d and p_i.

The trends of direct and indirect radiation as a function of the tube tension are showed in figure 6.3.

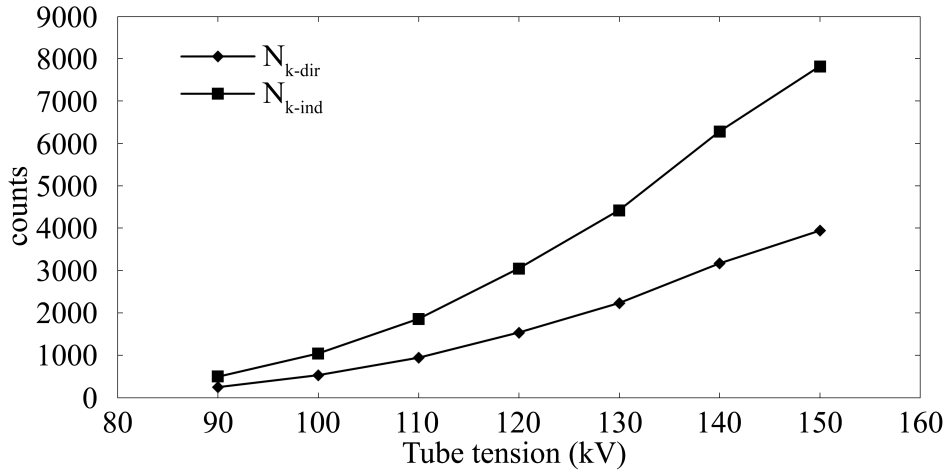

Figure 6.3: Plot of the direct and indirect radiations as a function of the tube tension.

The last result concerns the calculation of the parameter B_k, that is the probability that a ionization event generates a characteristic photon. Table 6.5 shows the evaluations of the integral in equation 2.13 according to the different considered cross section models.

kVp	Gryzinski	Casnati et al.	Hombourger
90	$1.24 \cdot 10^{-4}$	$1.10 \cdot 10^{-4}$	$1.98 \cdot 10^{-4}$
100	$3.27 \cdot 10^{-4}$	$2.45 \cdot 10^{-4}$	$4.39 \cdot 10^{-4}$
110	$6.44 \cdot 10^{-4}$	$4.28 \cdot 10^{-4}$	$7.68 \cdot 10^{-4}$
120	$10.82 \cdot 10^{-4}$	$6.53 \cdot 10^{-4}$	$11.77 \cdot 10^{-4}$
130	$16.39 \cdot 10^{-4}$	$9.11 \cdot 10^{-4}$	$16.56 \cdot 10^{-4}$
140	$23.10 \cdot 10^{-4}$	$11.96 \cdot 10^{-4}$	$21.93 \cdot 10^{-4}$
150	$30.88 \cdot 10^{-4}$	$15.01 \cdot 10^{-4}$	$27.80 \cdot 10^{-4}$

Table 6.5: Values of N_k^{ion} (equation 2.12) as a function of the tube tension for each model.

Figure 6.4 shows the trend of N_k as a function of $(1 + p_i)N_k^{ion}$. Also the figure shows the best fit line for each of the three cross section model.

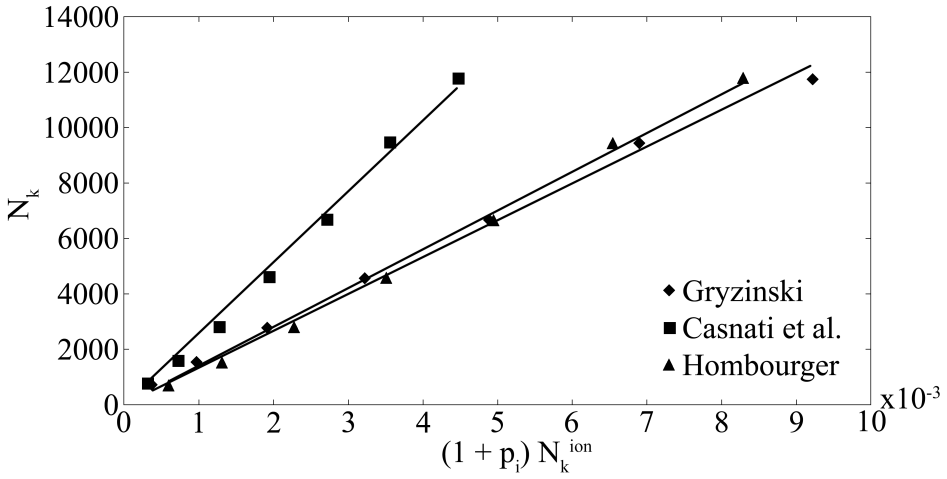

Figure 6.4: Plot of N_k as a function of $(1 + p_i)N_k^{ion}$.

The linear fitting of the data showed in figure 6.4 results for each model are showed in table 6.6.

	Gryzinski	Casnati et al.	Hombourger
$QB_k \pm 2\%$	$1.33 \cdot 10^6$	$2.56 \cdot 10^6$	$1.39 \cdot 10^6$
	$Q \geq 2.56 \cdot 10^6 \pm 2\%$		
$B_k \leq$	$0.52 \pm 4\%$	$1.00 \pm 4\%$	$0.55 \pm 4\%$

Table 6.6: Values of QB_k evaluated by fittind N_k and $(1 + p_i)N_k^{ion}$ for each cross section model as described in equation 2.13 and estimations of the parameters Q and B_k.

Models root mean square deviations (RMSD) at each tube tension are shown in table 6.7.

Tension (kV)	90	100	110	120	130	140	150	mean
Gryzinski	87	83	119	111	130	100	112	99
Casnati et al.	16	98	128	92	44	115	238	86
Hombourger	13	91	116	79	47	108	205	79

Table 6.7: Models RMSD results at different tube tensions.

Looking at table, the Homburger model is the most accurate followed by Casnati *et al.* and Gryzinski. For this reason the Hombourger model was chosen as the most accurate and useful to evaluate the direct radiation with equation 2.7 and the K-peak lines using equation 2.8.

The last test considered in the comparison of the spectra described in literature and the model of K-lines generated using the Hombourger model. The results of the comparison as shown in figures 6.5 and 6.6 and the comparison of the peak areas are shown in table 6.8.

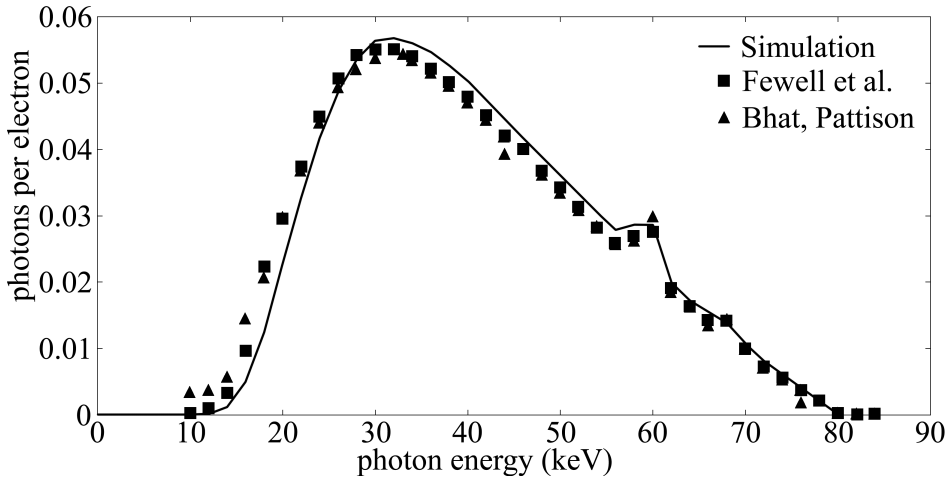

Figure 6.5: Comparison of the experimental and simulated spectra at 80kV of tube tension. The areas of the spectra are normalized.

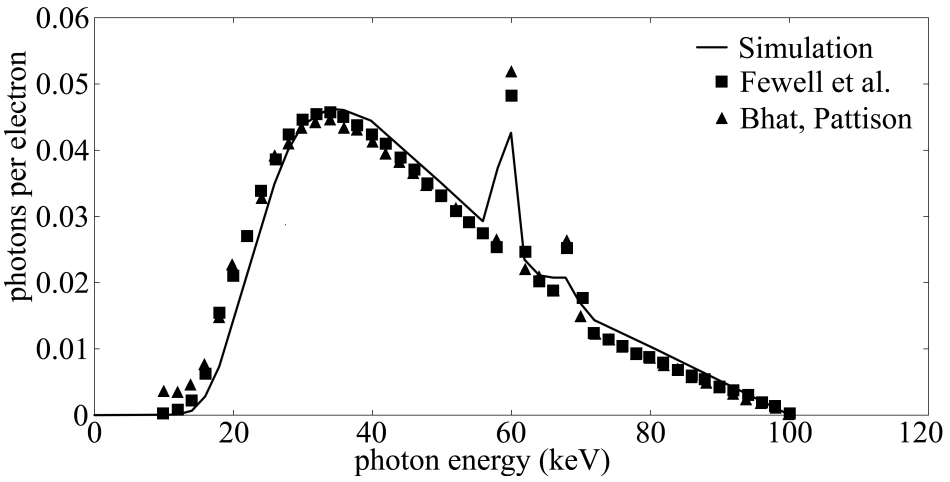

Figure 6.6: Comparison of the experimental and simulated spectra at 100kV of tube tension. The areas of the spectra are normalized.

	keV	Sim ±2%	Fewell *et al.*	Bath-Pattison
	60	$9.4 \cdot 10^{-3}$	$9.569 \cdot 10^{-3}$	$11.779 \cdot 10^{-3}$
80 kV	68	$2.00 \cdot 10^{-3}$	$1.940 \cdot 10^{-3}$	$3.018 \cdot 10^{-3}$
	70	$0.484 \cdot 10^{-3}$	$0.360 \cdot 10^{-3}$	$0.610 \cdot 10^{-3}$
	60	$26.8 \cdot 10^{-3}$	$23.262 \cdot 10^{-3}$	$29.064 \cdot 10^{-3}$
100 kV	68	$5.5 \cdot 10^{-3}$	$8.519 \cdot 10^{-3}$	$10.754 \cdot 10^{-3}$
	70	$1.31 \cdot 10^{-3}$	$2.946 \cdot 10^{-3}$	$1.854 \cdot 10^{-3}$

Table 6.8: Comparison of the experimental peak areas and simulations using the Hombourger model in equation 2.7.

6.2 Total Air Kerma function of anode voltage

The total air KERMA as function of tube HV and filtration is shown in Figure 6.7 .

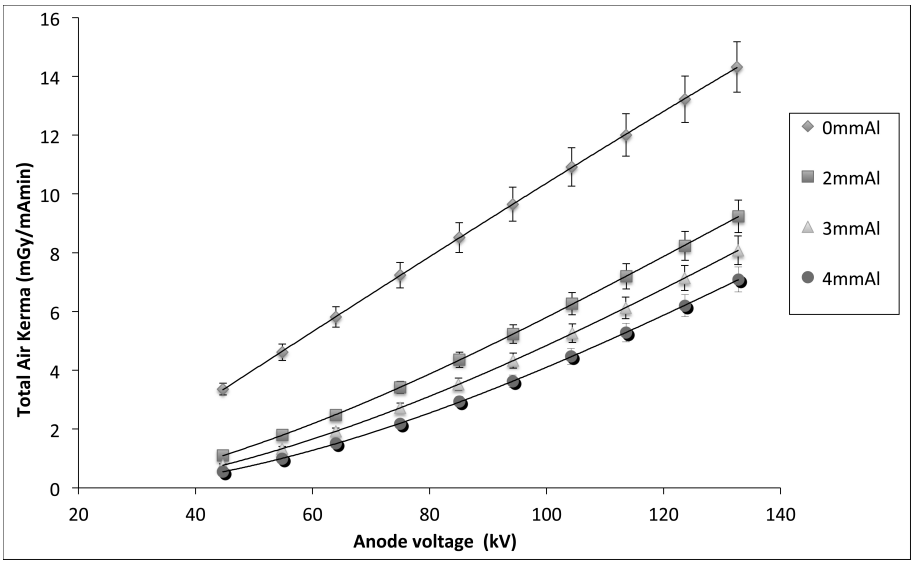

Figure 6.7: Total Air Kerma per unit workload (kV) at 1m.

The polynomial fit coefficients of the X-ray tube output as a function of kV are shown in the Table 6.9. The uncertainty has been estimated to be 6%.

mmAl	a_3	a_2	a_1	a_0
0	$-3.3619 \cdot 10^{-7}$	$2.2555 \cdot 10^{-5}$	$1.2934 \cdot 10^{-1}$	-2.4572
2	$-1.9279 \cdot 10^{-6}$	$7.5527 \cdot 10^{-4}$	$7.5080 \cdot 10^{-3}$	$-5.7318 \cdot 10^{-1}$
3	$-1.4099 \cdot 10^{-6}$	$6.7703 \cdot 10^{-4}$	$-1.0427 \cdot 10^{-3}$	$-4.1166 \cdot 10^{-1}$
4	$-1.5863 \cdot 10^{-6}$	$7.4043 \cdot 10^{-4}$	$-1.6695 \cdot 10^{-2}$	$-4.4388 \cdot 10^{-2}$

Table 6.9: The polynomial fit coefficients of the X-ray tube output $(mGy/(mAmin)@1m)$ as a function of kV, according to the equation: $mGy/(mAmin)@1m = a_3kV^3 + a_2kV^2 + a_1kV + a_0$.

6.3 Si(PIN) detector curve response

The calibration curves of the Si-PIN with respect to total air Kerma measured by the CAPINTEC dosimeter at different Aluminum filtration are shown in Figures 6.8,6.9,6.10 and 6.11.

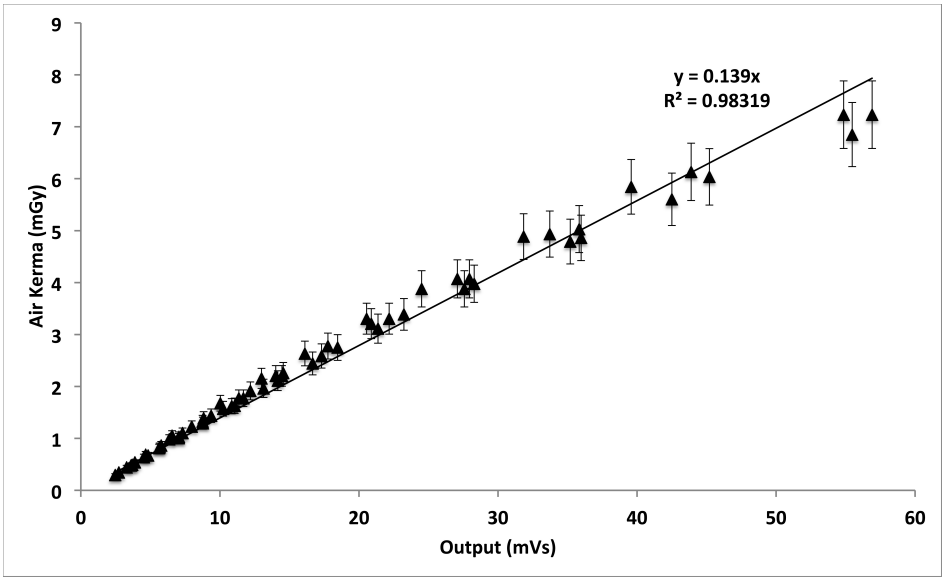

Figure 6.8: Calibration fit of the Si-PIN detector output respect to total Air Kerma at 1m for spectra with an additional filtration of 0 mm of Aluminum.

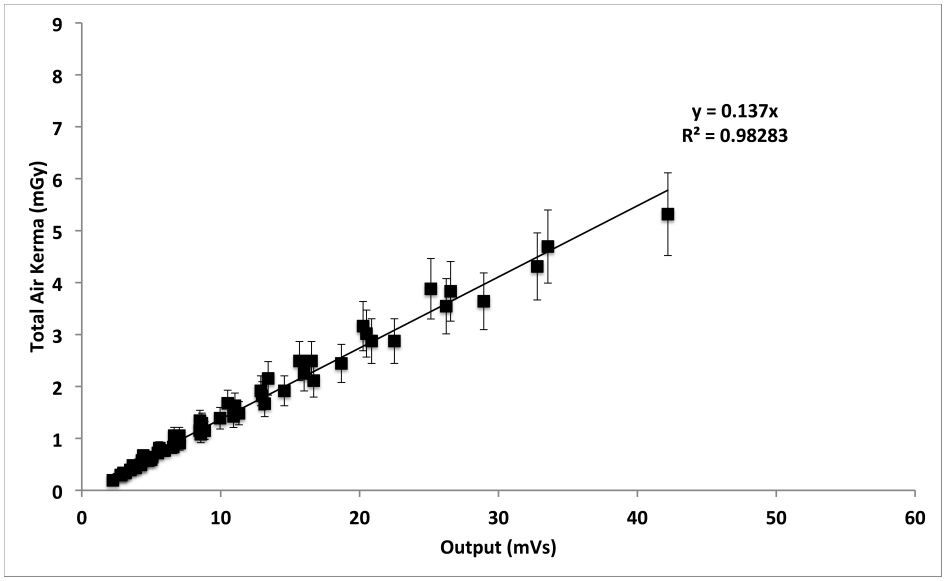

Figure 6.9: Calibration fit of the Si-PIN detector output respect to total Air Kerma at 1m for spectra with an additional filtration of 2mm of Aluminium.

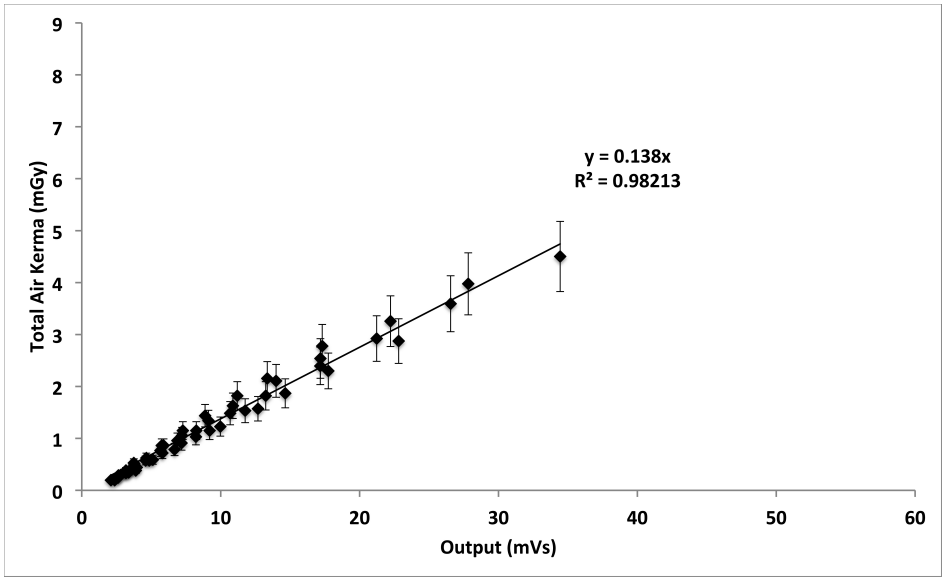

Figure 6.10: Calibration fit of the Si-PIN detector output respect to total Air Kerma at 1m for spectra with an additional filtration of 3mm of Aluminium.

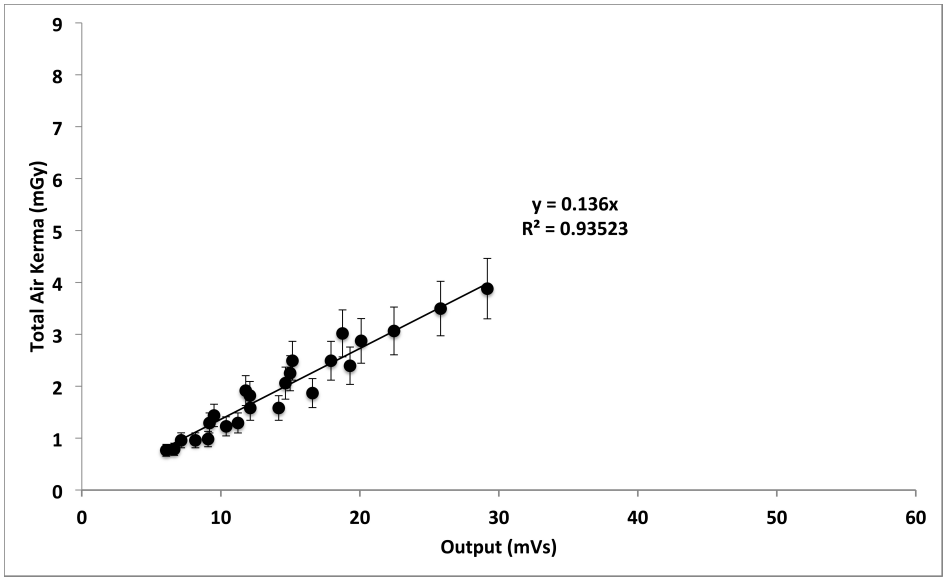

Figure 6.11: Calibration fit of the Si-PIN detector output respect to total Air Kerma at 1m for spectra with an additional filtration of 4mm of Aluminium.

The uncertainty of the measured KERMA values has been estimated to be 8% for unfiltered spectra, and 15% for spectra with added filtration. The slopes of the calibration lines as a function of the filtration are listed in Table 6.10.

Filtration (mm Al)	Slope (mGy/mVs)
0	0.139 ± 0.001
2	0.137 ± 0.002
3	0.138 ± 0.002
4	0.136 ± 0.003

Table 6.10: List of the detector response calibration parameter as a function of the additional filtration.

6.4 Si(PIN) + CsI(Tl) scintillation detector curve response

The calibration of the Si(PIN) + CsI(Tl) with respect to total Air Kerma is shown in Figures 6.12,6.13,6.14 and 6.15. Given the difference of energy response of the Si-PIN+CsI(Tl) and the ionization chamber in the energy range of interest, multiple sets of different data were plotted for the scintillator calibration.

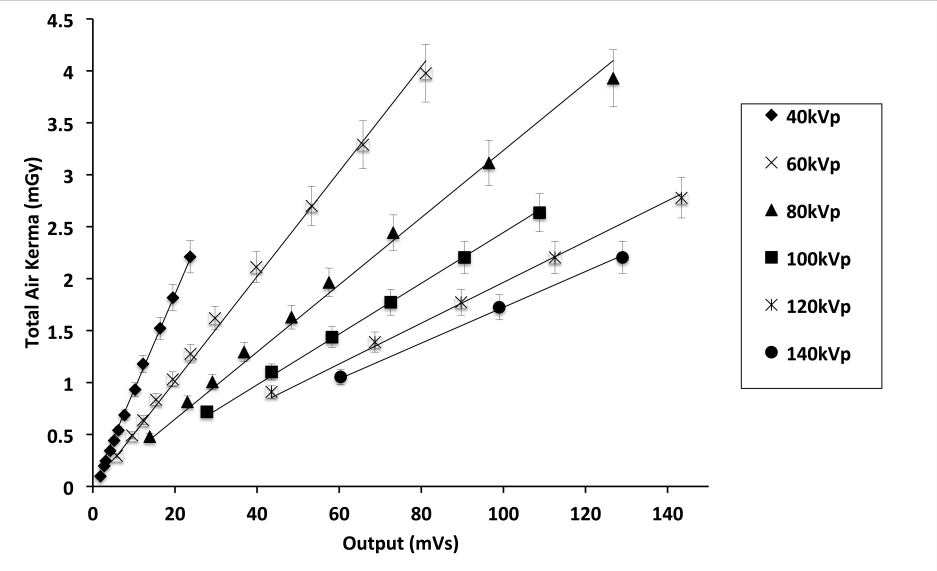

Figure 6.12: Calibration fit of the Si-PIN diode + CsI(Tl) scintillation detector output respect to total Air Kerma at 1m for spectra with an additional filtration of 0mm of Aluminium.

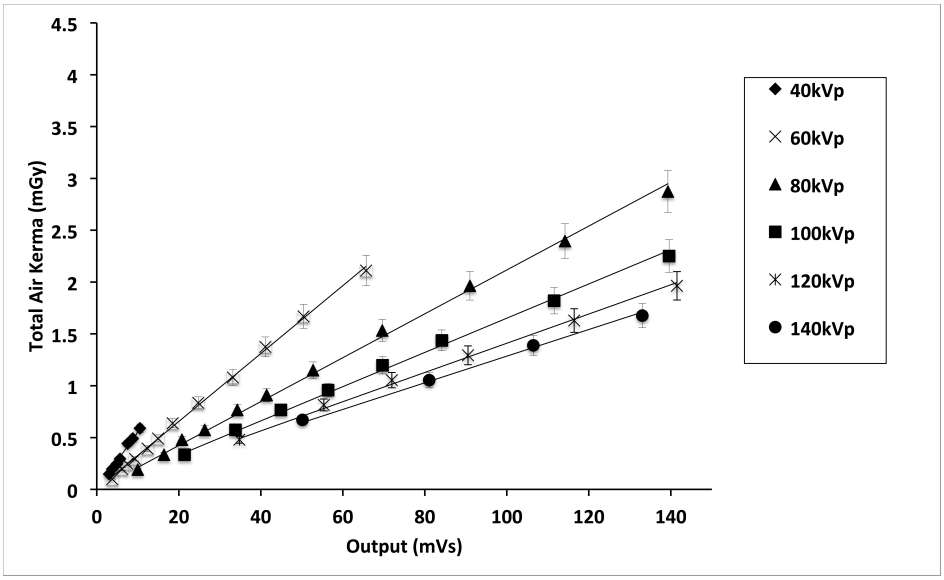

Figure 6.13: Calibration fit of the Si-PIN diode + CsI(Tl) scintillation detector output respect to total Air Kerma at 1m for spectra with an additional filtration of 2mm of Aluminium.

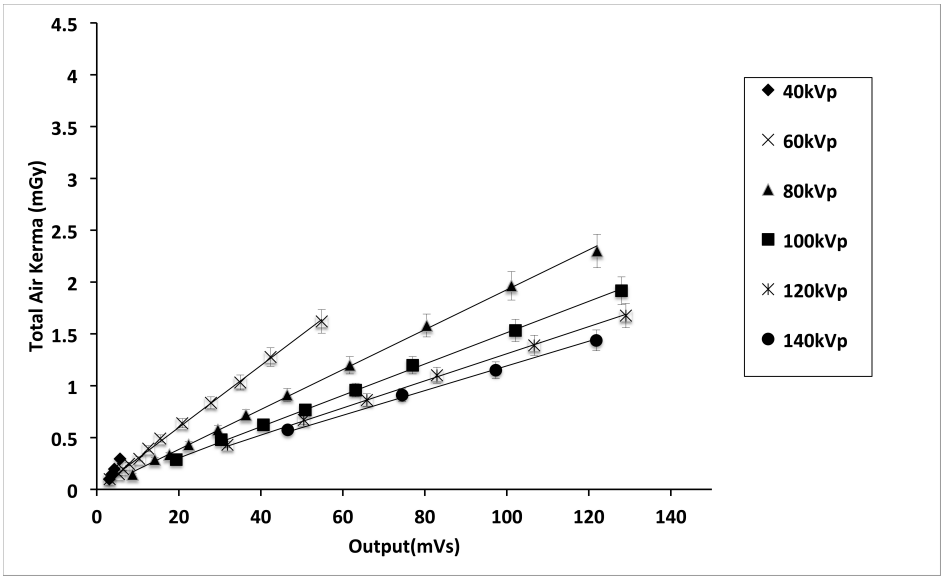

Figure 6.14: Calibration fit of the Si-PIN diode + CsI(Tl) scintillation detector output respect to total Air Kerma at 1m for spectra with an additional filtration of 3mm of Aluminium.

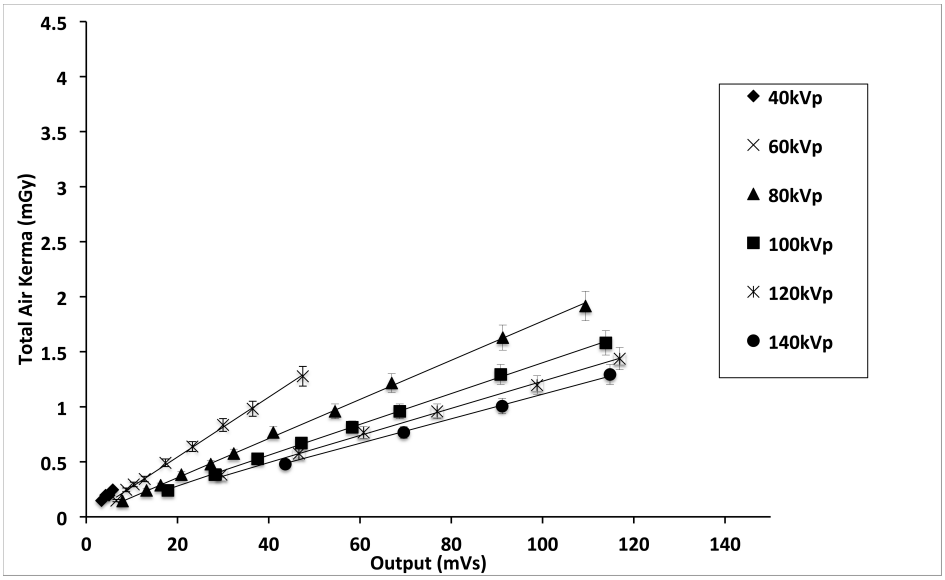

Figure 6.15: Calibration fit of the Si-PIN diode + CsI(Tl) scintillation detector output respect to total Air Kerma at 1m for spectra with an additional filtration of 4mm of Aluminium.

The uncertainty if the experimental data has been estimated to be 7%. In the case of diode-scintillator calibration, it is evident that the slope of the output of the diode depends on the tube tension. Thus, as previously, the detector response as a function of the tube tension and of the additional filtration is shown in Table 6.11.

	0 mm Al	2 mm Al	3 mm Al	4 mm Al
40 kVp	0.092	0.0554	0.046	0.042
	±0.001	±0.001	±0.004	±0.001
60 kVp	0.0490	0.0328	0.0299	0.0272
	±0.0007	±0.0002	±0.0002	±0.0002
80 kVp	0.0323	0.0212	0.0193	0.0178
	±0.0005	±0.0002	±0.0001	±0.0001
100 kVp	0.0228	0.0165	0.01512	0.01400
	±0.0008	±0.0002	±0.0008	±0.0007
120 kVp	0.0196	0.0141	0.01309	0.01232
	±0.0002	±0.0001	±0.00006	±0.00008
140 kVp	0.0172	0.0129	0.0119	0.01114
	±0.0001	±0.0001	±0.0001	±0.00007

Table 6.11: Matrix of the Diode-Scintillator response as a function of the tube tension and additional filtration. The cell of the matrix contain the values of the slope of the calibration curves (mGy/mVs).

This dependency is also shown in Figure 6.16, were the slopes are plotted as function of the tube tension (kVp). The solid line represents a fit of the slopes.

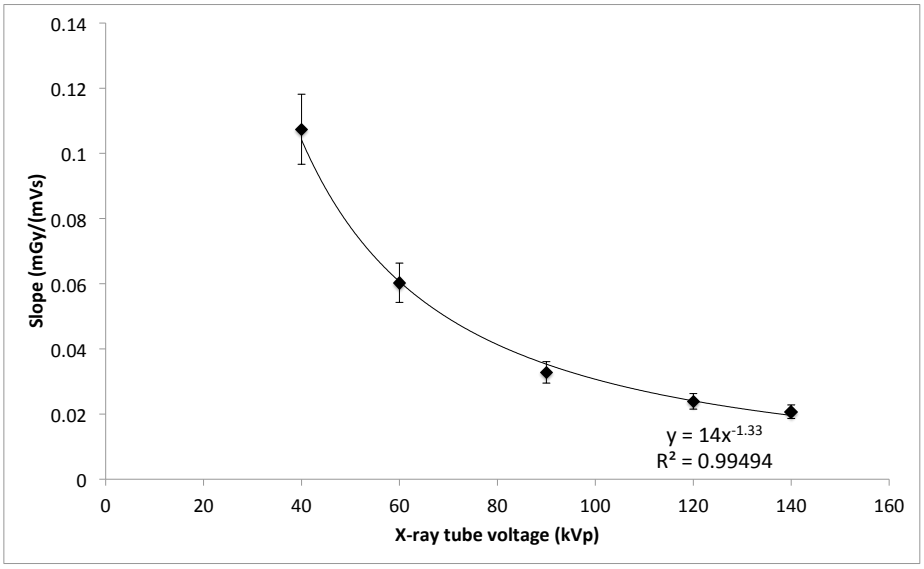

Figure 6.16: The slope of the calibration fit as a function of kVp.

6.5 Real time spectrometer validation

Figures 6.18 and 6.20 show the screenshots of the software interface. In order to estimate errors, the calculated spectrum shape has been compared with the reference spectrum acquired with the HPGe detector (see Fig. 6.17 and Fig. 6.19) and it is very good: the calculated curve differs from that measured by less than 3%.

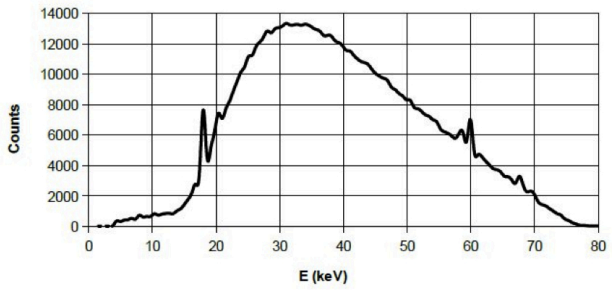

Figure 6.17: Spectrum measured by HPGe at a distance of 480 cm, collimating the beam. Tube voltage 80 kVp, anode current 320 mA and emission time 100ms.

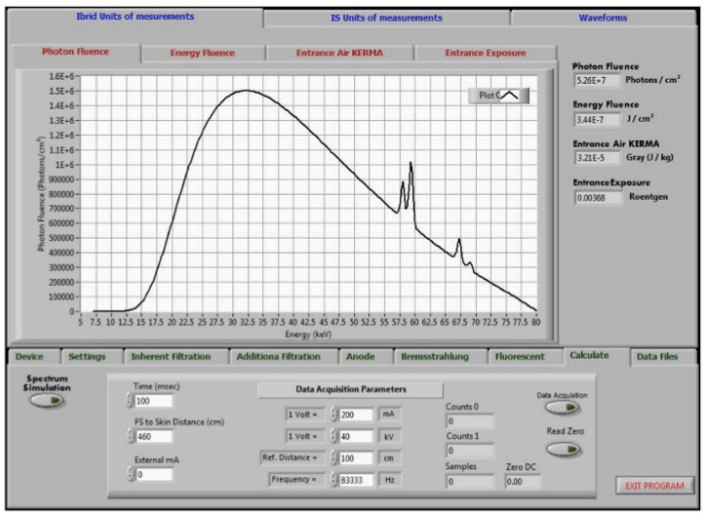

Figure 6.18: Screenshot of the program. Tube voltage 80 kVp, anode current 320 mA and emission time 100ms.

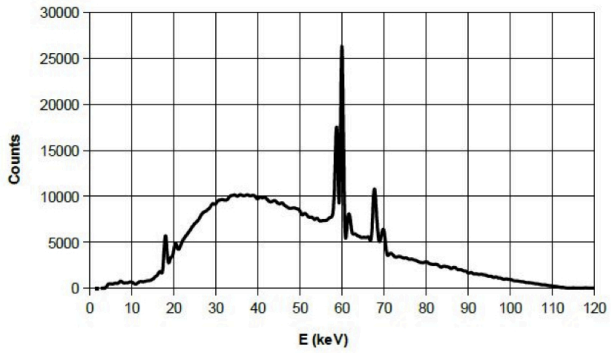

Figure 6.19: Spectrum measured by HPGe. Tube voltage 120 kVp, anode current 320 mA and emission time 100ms.

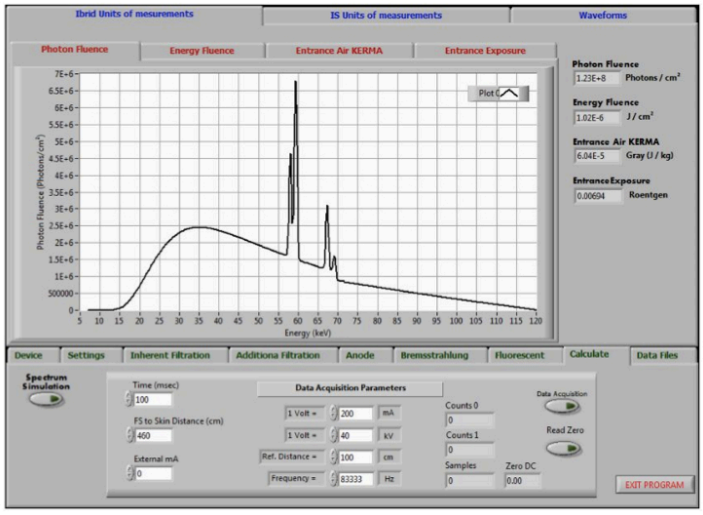

Figure 6.20: Screenshot of the program. Tube voltage 120 kVp, anode current 320 mA and emission time 100ms.

Chapter 7

Discussion and conclusion

7.1 Fluorescence lines reconstruction

The results presented in the previous chapter gives information about the behavior of direct and indirect radiation that emerges from the anode of an X-ray tube. This work started by the analysis of the k-characteristics models described in literature that use the indirect radiation (table 6.3). Then a direct radiation model was developed and a review of the principal models of electron ionization cross sections was performed. The parameters needed to describe the peaks were evaluated from literature and from experimental tests performed. In this way a detailed description of the direct and indirect radiation has been presented (table 6.4 and figure 6.3). Then the model was validated using other spectra described in literature (table 6.8, figures 6.5 and 6.6).

Looking at figure 6.2 it possible to see that the experimental data are in excellent agreement with linear correlation described by Poludniowski and Dyson and represented in equation 2.2. This allows to evaluate the parameter p_d with a great precision (4%). Other models of bremsstrahlung considered the knowledge of this parameter as empirically determined, depending on the experimental conditions. In this case, instead, the value is independent of the experimental conditions and is related to the anode material. From these

evaluations the contribution of the direct and indirect radiation was determined. Table 6.4 and figure 6.3 show that the contribution of direct radiation to the K-peaks is much lower than the indirect, according to Tothill results [53], based on Green and Cosslett theoretical model [34]. The results of the partition between direct and indirect radiation were then used to evaluate the performances of the cross section models. So it was possible to evaluate the parameter QB_k. Figure 6.4 shows an excellent agreement in the range 90kV to 150kV between the considered data and the calculated photon production by ionization using equation 2.12. This is a strong validation of the hypothesis in equation 2.7 of linearity between the number of ionization and direct radiation through B_k. It also represents a validation of the meaning of the parameter Q. Both these parameters are independent of the peaks energies (E_j) and B_k depends only on the atomic number (Z) and the edge energy (E_k) of the anode material. Similarly, Q depends only on the experimental parameters and setup. Although these parameters are very important it was not possible to split their contributions using the data available, not from the experimental tests, neither from literature data. The only determination which could be done were limiting estimations of the allowed values as shown in table 6.6. The parameter Q has a very huge lower limit. This can be explained looking at its meaning: depending on the geometrical setup, it also contains data about the total number of electrons impacting the anode (600 mAs represents a very huge number of electrons). The fact that $B_k \leq 1$ can be explained considering the photon production by ionization process. It is not generally true, and the models of Gryzinski and Hombourger show that all the ionization events create a detectable direct radiation photon. This can be explained considering the ways of interaction of the electrons with the ionization hole in a shell. There are two main ways of interactions: decay from outer shells, or interaction with free electrons. The first phenomenon is what is commonly accepted as direct characteristic line [36, 37]. However not every ionization is followed by a decay from the outer shells due to an external recombination with free electrons can happen. This recombination refers to

the second way of interaction. Not all free electrons have a probability to fill the ionization hole. Only those electrons with energy lower that E_k can do this. However not all the produced photons have enough energy to emerge from the anode. This reduces the probability that every ionization produces a k-photon, so $B_k < 1$. After calibrating the direct radiation models, a final test was performed to choose the best cross section model. As can be seen by table 6.7 the Hombourger model was the most accurate. This did not surprise as it is the most recent model and takes into account the correction needed to modify the Gryzinski and Casnati models. Therefore the measurements in this article confirms what was stated by Hombourger and validate its model.

The last validation test concerned the comparison of independent data taken from literature. As shown in figures 6.5 and 6.6 and in table 6.8 there is an excellent agreement with the data of Fewell *et al.* and Bhat-Pattison.

In conclusion, this work presents a methodology to evaluate the characteristic photons without considering the knowledge of the bremsstrahlung spectrum. This had the advantage to make the peak calculation independent of the continuum spectrum. The results showed an excellent validation of the models hypotheses and very good ability to evaluate the peaks of experimental spectra. Moreover the direct radiation based peak calculation depends only on physical parameters easily available in literature, so it is relatively simple to implement them.

The incoherence in our model, which is common to others in literature, is the fact that the electron energy loss is modeled using the replacement 2.6, that is the CSDA range, while the auto-attenuation of the anode uses the Thomson-Whiddington relation. Next works have to resolve this incoherence in order to unify the calculation of the electron penetration and energy loss. Further studies are necessary to study the behavior of B_k as a function of Z and a way to evaluate the term Q.

7.2 Spectrum total photon fluence measurement

In order to reliably and accurately reproduce the spectrum area, two different methodologies for efficiently reconstructing the X-ray spectrum fluence of the available diagnostic beam were presented.

The first method is based on measuring the HV and Ia waveforms taken out from the radiological system's inverter. The software, written in LabView, reads them and reconstructs the shape from the HV waveform and the area using the Ia waveform and the air KERMA. The relation $mGy/(mA \cdot min)$ as a function of the average HV measurement was evaluated. As shown in Figure 6.7, when the beam is not filtered, the fitting curve appears linear, but as the filtration increase it bends because of absorption of the low energy photons by the Al filters that causes a lower interaction of the beam with the detector. So the total air KERMA slowly increases with the tube HV. This method is sufficiently precise. The error on the spectrum area has been measured as $\pm 6\%$, but a specific calibration for any apparatus is required. It was then thought that the method is too intrusive.

The second method is based on measuring the total Air Kerma of the available diagnostic beam with two different silicon diode detectors. With the data recorded by the detectors, the software is able to provide the X-ray spectrum area. The results of the naked diode calibration presented in the previous chapter (figures 6.8,6.9,6.10 and 6.11) show a very coherent response independently from the additional filtration (table 6.10). On the contrary, the coupling with the scintillator evidently splits the curves and highlights the tube tension and the additional filtration dependency of the response. Of course these differences in the detector behavior are due to the scintillator. In the case of the naked diode, in fact, the detector has low quantum efficiency and the sensitivity is reduced. For this reason the differences due to the tube tension are hidden and the curves appear overlapped (figures 6.8,6.9,6.10 and 6.11). For the same reason the calibration slopes as

a function of the filtration are consistent and the values are actually the same within the uncertainties. On the contrary, the interaction between the beam and the scintillator dramatically affects the detector response. This is due to the conversion from X-rays to optical photons that optimizes the detector quantum efficiency. The luminosity of the scintillator increases the number of photons on the diode surface. This increases the detector sensitivity, but makes the detection response more complex to analyze (figures 6.12,6.13,6.14 and 6.15), due to the beam quality (tube tension, and filtration) becomes a fundamental parameter. In addition, the CsI(Tl) is affected by the afterglow that depends on the dose rate and the detector exposure time [54]. It can be seen in table 6.11 that the addition of the filtration reduces the detector response (see figure 6.16) and the lines become closer (e.g. compare figures 6.12 and 6.15). This means that cutting the soft X-rays reduces the quantum efficiency, then the number of converted optical photons, and thus the response tends to be flat as in the case of the naked diode.

In conclusion, the presented methods contributes to the field by presenting an improved simulation of a realistic X-ray beam emerging from a common diagnostic X-ray tube with a complete and detailed spectrum that lends itself to further studies of added filtration, thus providing an optimized beam for different diagnostic applications in medicine.

7.3 Real time spectrometer

Two naked Si-PIN diodes and two Si-PIN diode + CsI(Tl) scintillators previously described were used on the custom detection system, mounted between the X-ray tube and the collimators group, that intercepts a little outer section of the beam. The components of the detector are commonly used in medical application [45, 55], but the proposed solution is original and totally not intrusive for the radiological device. Detectors measure the output of the X-ray tube with different time constants and different dynamic ranges. Using the data recorded by the detector, the software is able to

evaluate the HV(t) and the Ia(t) and a series of parameters to introduce in the parametric model of the X-ray spectrum. The operator has only to insert the values of nominal kVp and mA in order to reduce the working interval and running time. Figures 6.18 and 6.20 show some screenshots of the software interface. This method furnishes the spectrum fluence with an error estimated practically similar to that obtained from the method based on measuring the HV and Ia waveforms. It is important to note that, in order to estimate errors, the calculated spectrum shape has been compared with the reference spectrum acquired with the HPGe detector (see Figures 6.17 and 6.19) and it is very good: the calculated curve differs from that measured by less than 3%. The principal component of the error is due to the measurement of the spectrum area that is the total fluence. This is due to the necessity of a strong collimation and a distance of approximately 5 m from the source in the spectra acquisition with the HPGe. The areas subtended to the measured spectra are therefore very small with respect to the real one so the error is too high. For this reason the well calibrated ionization chamber has been introduced. The error on the area is now due to the calculation of the photon fluence starting from the air KERMA. The chamber calibration was performed with primary standards at $\pm 3\%$ and ISO beams.

Part II:

Feasibility tests of large area position-sensitive Silicon Drift Detectors

Chapter 8

Large area Silicon Drift Detectors and front-end electronics

8.1 Large area position-sensitive Silicon Drift Detectors (SDDs)

Silicon Drift Detectors (SDDs) of small dimensions (up to 1 cm^2) have been successfully employed in X-ray spectroscopy due to their small anode geometry, which allows to minimize the electronic noise due to the read-out device. Many applications, however, require large sensitive areas to be covered, so that these detectors are effectively not useful. Large-area SDDs [56, 57] coupled with a very low noise integrated front-end electronics (FEE) are very promising for several applications, where large sensitive areas combined with excellent energy resolutions are required, such as high-energy astrophysics instrumentation (X-ray All-sky Monitor, large-area X-ray timing, Gamma Compton Camera), and Single-Photon-Emission Computed Tomography systems based on a Compton Camera for medical imaging. The low anode dark current of the SDDs attainable at temperatures between -20°C

and -50°C makes it possible to achieve a very low noise detection system by keeping the parallel noise component at low levels. However, the achievable performance depends not only on the quality of the detector itself, but also tightly derives from the performance of the FEE. Therefore, a sophisticated design of the integrated FEE circuit is required to achieve high spectral resolutions.

In this section of the thesis, the preliminary tests with a low-noise and low-power ASIC designed and optimized for analog pulse processing of signals from monolithic large-area SDDs, coupled to a 30.5 cm^2 SDD (fig. 8.1) are described. They are performed as part of the National Institute of Nuclear Physics (INFN) (Bologna Section) project "REDSOX - Research Drift for Soft X-rays". It is devoted to the characterization of large-area position-sensitive Silicon Drift Detectors for X-radiation study and it is aimed to:

- the development large surface Silicon Drift Detectors for X-ray astrophysics;
- the evolution of the SDD tecnology in collaboration with FBK CMM Trento;
- the development of high energy resolution detectors for soft X-rays;
- the development of detectors for Advanced Light Sources.

Moreover, large-area SDDs with a low-noise, low-power ASIC readout are the fundamental keys to LOFT, the Large Observatory for X-ray Timing, a new medium-class space mission currently that the European space Agency has been assessing since February of 2011. The LOFT project was proposed as part of the Cosmic Vision Program (2015-2025).

Very large-area multi-anode SDD were developed for particle tracking applications such as LHC-ALICE experiment at CERN [58, 59, 60], demonstrating very good performance in localizing the impact point of ionizing particles in a high multiplicity environment [61, 62]. Based on the large experience coming from ALICE SDD development (by INFN-Trieste, in collaboration with Canberra Industries Inc.) a new large area SDD optimized

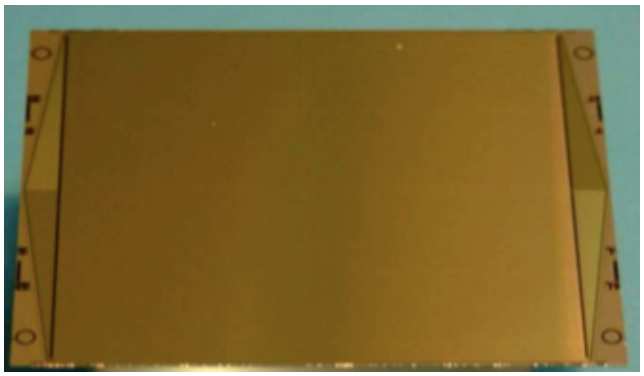

Figure 8.1: An image of a large area position-sensitive Silicon Drift Detectors prototype having a sensitive area of 4.35 x 7.02 cm^2.

for X-ray applications was realized in the framework of a new *R&D* activity with a strong collaboration between INFN-Trieste and FBK in Trento, Italy. This detector features a thickness of $450\mu m$ and a sensitive area of 30.5 cm^2 divided in two halves. The anodes placed at the edges of the two detector halves have different pitch, $147\mu m$ and $967\mu m$, with an anode capacitance of about 80 fF and 350 fF, respectively. A negative HV potential supplies power to the detector from its central cathode, while several integrated voltage dividers provide both the scaled potentials to create the constant drift field and the bias of the guard cathodes placed at the sides of the drift region. The latter are used to scale down the drift potentials to ground at the edge of the SDD in a controlled way (fig. 8.2). The X-ray photon absorption creates a cloud of electron-hole pairs. The electrons are quickly focused in the middle plane of the detector, thanks to the sideward depletion technique [63], and then carried towards the anodes thanks to the drift field. Because of diffusion, the size of the electron cloud increases with time before reaching the collecting anodes (fig. 8.3) . This phenomenon has important consequences on the energy resolution of the detector, degrading the spectroscopic performances with increasing drift lengths, when the electron cloud involves more than one anode. In this case the evaluation of the total charge is affected by the so-called signal leakage. Therefore in this work we only considered

single-anode events (i.e. all the charge is collected by one anode), in order to estimate the best inherent noise performances of large area devices. The noise measurements were performed with the largest anode pitch (967 μm) only.

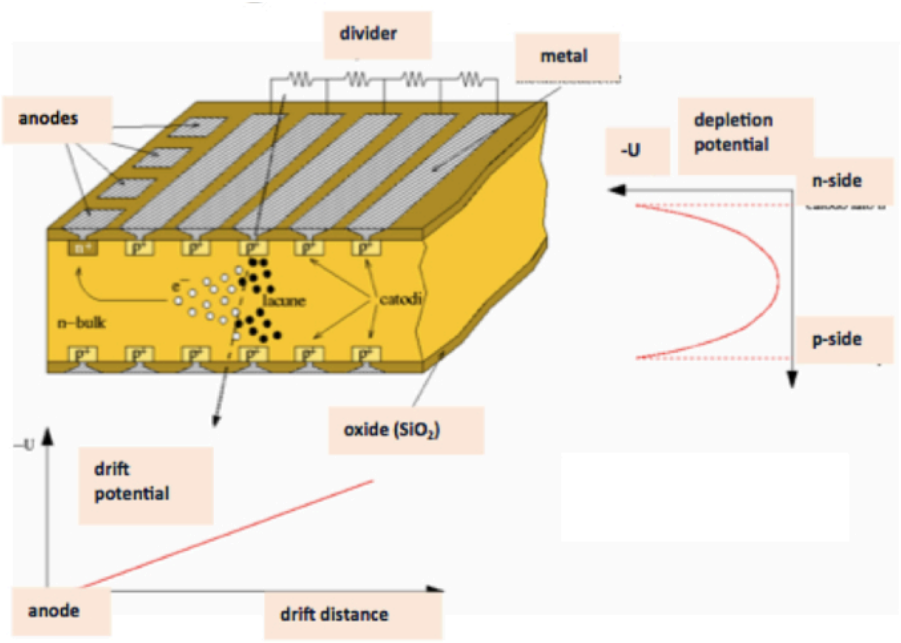

Figure 8.2: A depletion and a drift potential are applied to the SDD.

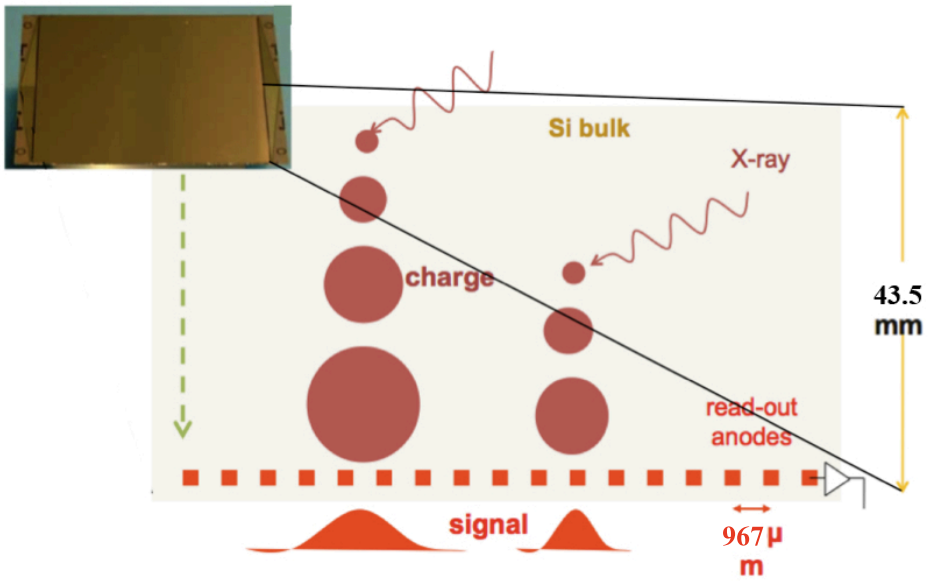

Figure 8.3: An image of the electron cloud, which increases with time before reaching the collecting anodes.

8.2 The ASIC Outline

The experimental setup for the preliminary tests on the first version of the ASIC for the LOFT project was performed at the INAF-IASF section of Bologna, in collaboration with the INFN of Bologna. The characterization of the ASIC for reading-out a Multi-Anode Silicon Drift Chamber, to be used for the detection of low energy X-ray (with a range of approximately 0.5 - 100 keV) is described. The ASIC has been designed in an AMS $0,35\mu m$, 4-metal, 2 polysilicon, CMOS technology. Figure 8.4 shows the block diagram of the complete ASIC. In order to better understand the system a detailed description of the *read-out pixel cell* (RPC) is given first. Here will be considered only the Pre-amplifier and the Shaper. Full details on the design and the functionalities of the ASIC are presented in [64]. Figure 8.5 shows the block scheme of the RPC. An inner view of each block will be given.

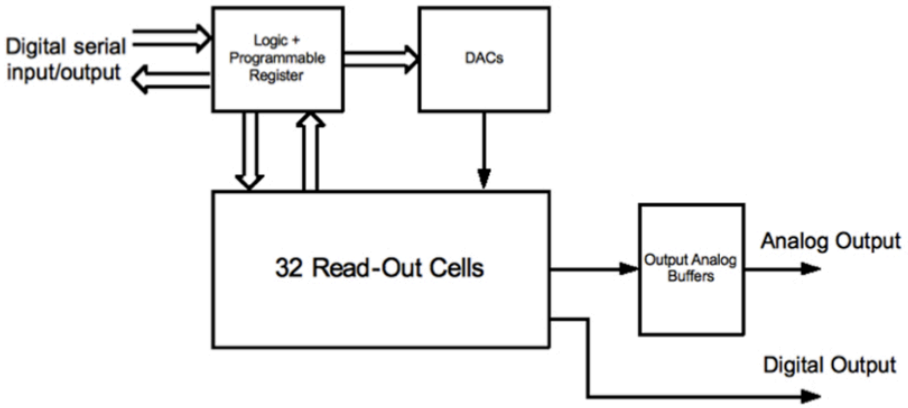

Figure 8.4: Block diagram of the ASIC.

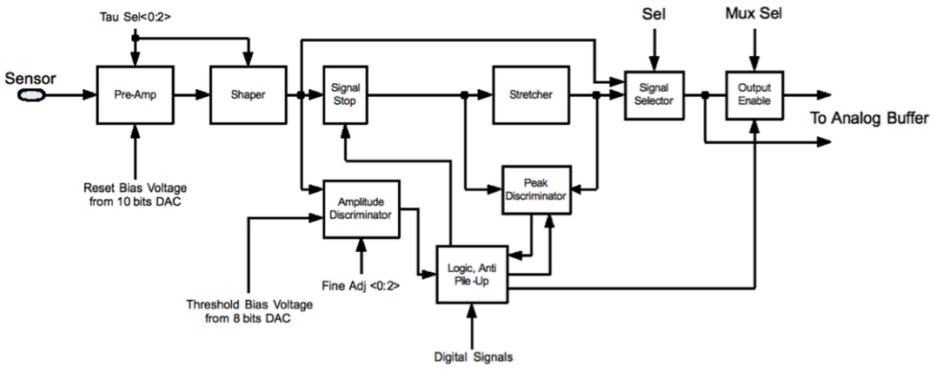

Figure 8.5: Block scheme of the RPC.

8.2.1 RPC: Pre-Amplifier

The pre-amplifier consists of two stages, as shown in Figure 8.6. The first stage is based on a classical amplification configuration using a p-MOSFET input transistor (MP75) in a folded-cascode architecture with active load. The following low-impedance output stage is instead a source follower. The input transistor is connected to a dedicated 2 V power supply to avoid interference from the main 3.3 V power supply and to properly bias the feedback PMOS. The size (W/L=100/0.4 μm) and the bias current of the input MOSFET are the result of an optimization which takes into account, as first priority, the minimization of the noise, with constraints on the power consumption and area occupation. The feedback (or 'reset') MOSFET is a P-channel device with size W/L=0.4/240 μm. Minimization of C_f is required to reduce the value (and so the area) of the coupling capacitance $C_1 = G \cdot C_f$ between the first and the second stage, while maintaining a high gain G = 40, which is necessary to minimize the second stage noise contribution, while ensuring a full scale output voltage range at the output of the shaper of 1.12 V with 27000 e^-. The Pre-Disable function (PRE_DIS active high) performs the following operations:

- the input of the first stage is put in a low-impedance configuration by a transmission gate (MP55 and MP56), shorting C_f;
- the second stage and the input stage of the shaper are turned off. Each of the 32 RPC can be turned off independently.

8.2.2 The Second Stage

The lower section of Figure 8.6 shows the structure of the second stage which performs the following functions:

- compensation of the signal-dependent shape of the preamplifier response (due to possible time-variant conductance of the feedback MOSFET);

- introduction of the first pole for signal shaping given by the product RC with 8 different values of C selectable by 3 control bits (BIT_TAU<0:2>).

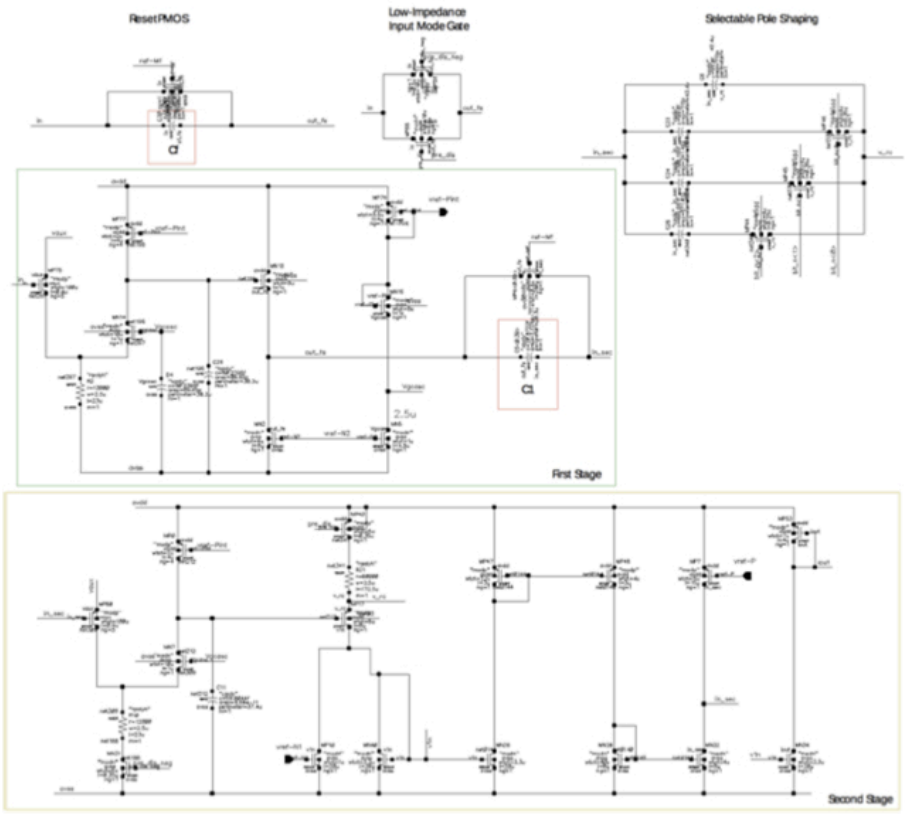

Figure 8.6: Pre-amplifier schematic.

8.2.3 Noise Considerations

Noise simulations have been done to find out if the solution shown in Figure 8.7 would decrease the noise of the input section. It has been calculated that an increase by four of the current flowing in R_2, produces only a reduction of almost 10% of the total electrical noise. In fact the main contributor of noise in the preamplifier, is the reset P-MOS. To increase the tunability of the preamplifier, the pin of R_2 will be taken out of the ASIC anyway. Linearity simulation over the full input range has been done to verify if this solution would decrease the overall channel performance. Figure 8.7b shows that the linearity is comparable to that from Monte Carlo simulations which was calculated without the dedicated ground. Figure 8.8 shows the input noise in respect to the leakage current of the detector and the shaping time. These simulations have been done without the dedicated ground of resistor R_2. For small values (a few pA) of the leakage current the main contributor to the total noise is the noise of the input PMOS whose transfer function is inversely proportional to the shaping time. For higher values the noise is dominated by the noise of the reset PMOS whose transfer function is directly proportional to the shaping time.

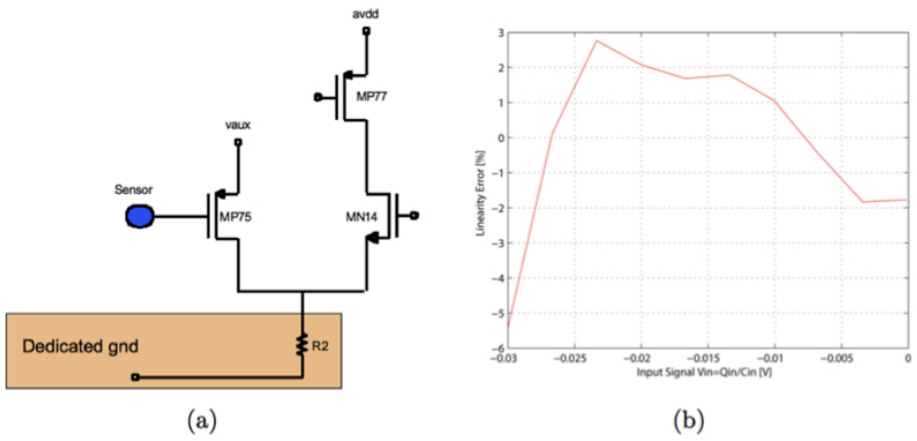

Figure 8.7: (a) Possible noise solution. (b) Linearity of the RPC with the R2 dedicated ground sets at -1.5 V.

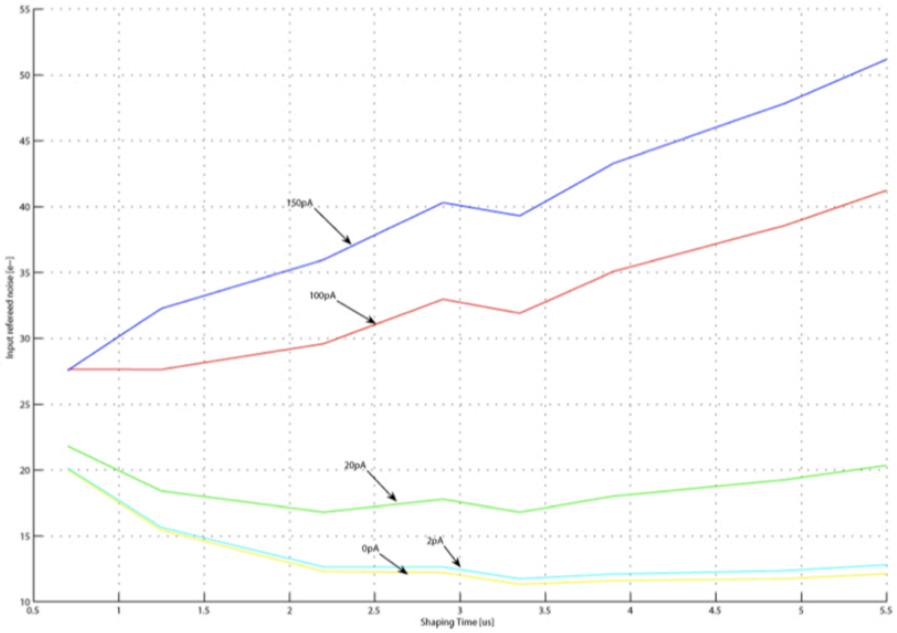

Figure 8.8: Input noise in respect to the leakage current and the shaping time.

8.2.4 RPC: Shaper

The shaping stage works in current-mode and consists of four parts: the first one equalizes the gain of the stage at the different shaping times, the second part cancels the DC component of the previous stage output, the third one introduces a real pole whose time constant is selectable by three bits and the fourth one introduces a negative feedback for DC signals, in order to set and stabilize the DC output voltage of the shaper. The schematic of the developed shaper is shown in Figure 8.9. The first block (gain equalizer) is part of a current mirror which takes the output current of the second stage of the pre-amplifier. The equalization is performed by changing the current mirror multiplication factor by means of the three bits selecting the shaping time. The second part is a multiple current mirror which cancels the DC component superimposed to the signal. The third part is a 'R-lens filter' stage. The fourth part reads the shaper output voltage by means of a differential amplifier, and compares it with a reference voltage applied externally to the chip, which is common to all RPC's. The signal generated by the differential stage is filtered by a low pass filter and applied at the gate of MN17. The current of MN17 is mirrored at the input node N of the 'R-lens filter' and is subtracted from the constant current generated by MP67, thus determining the bias current of the shaping stage and its output DC voltage. The shaper input stage is disabled when PRE_DIS is high.

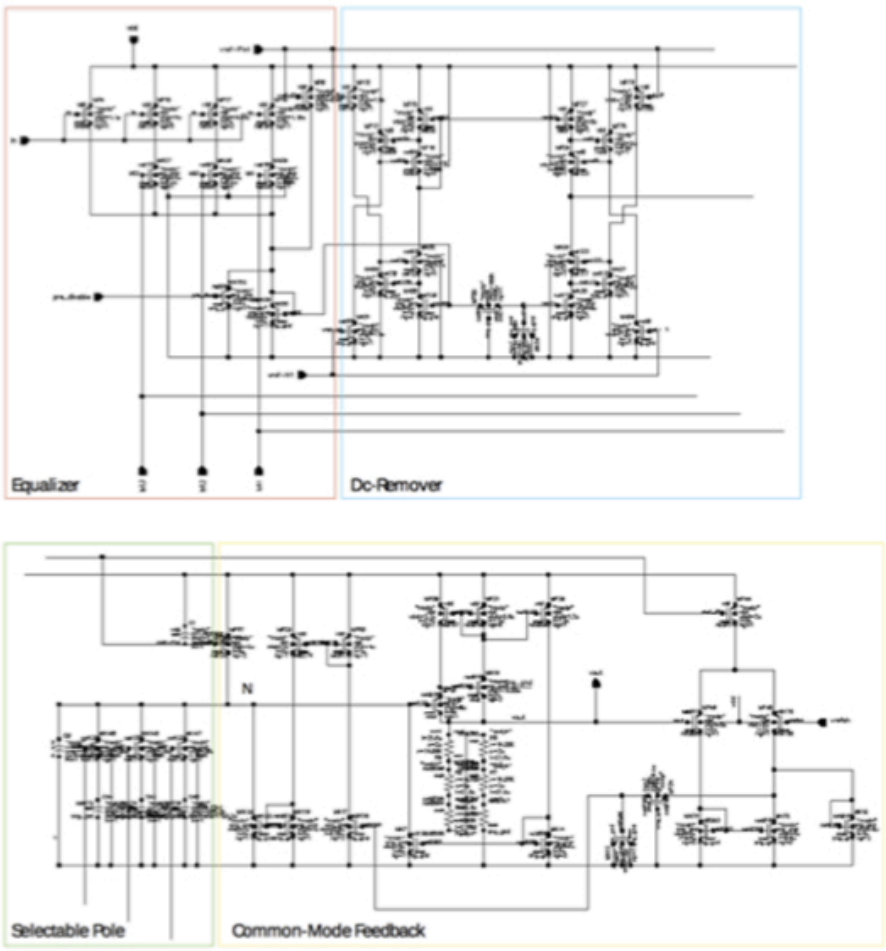

Figure 8.9: Shaper schematic.

8.2.5 RPC Summary

Table 8.1 summarizes the input and output signals for any RPC.

Signal	Type	Note
in	Analog in	From sensor
EXT_TRG	Digital in	Trigger from outside the chip
OR_CHANNEL	Digital In	OR of the 32 RPC triggers
SEL_EXT	Digital In	Selects which ext trigger is active
TRG_MODE	Digital In	Selects if the trigger is internal or external to RPC
PRE_DIS	Digital In P. for each RPC	Disables the amplification stage
DISC_DIS	Digital In P. for each RPC	Disables the amplitude discriminator
BIT_TH< 0 : 2 >	Digital In P. for each RPC	Fine tuning of the amplitude discriminator threshold
DAC_th	Analog In/Out	Defines the threshold
EOC	Digital in	Reset signal (from ext ADC)
RESET	Digital in	Asyncronous reset
channel_trg	Digital Out	Going to the 32 RPC triggers OR gate
OUT_EN	Digital In P. one hot logic	One-hot mux signal
out	Analog Out	Output after mux
out_pre_mux	Analog Out	Output before mux (8 central RPCs)
SIG_SEL	Digital In P. (common to all 32 RPC)	Selects whether shaper output or stretcher output should be connected
DAC_reset	Analog In	Reference voltage for the reset p-MOS of the pre-amplifier
BIT_TAU< 0 : 2 >	Digital In P. (common to all 32 RPCs	Select the shaping time constant

Table 8.1: Summary of the RPC signals (P. stands for programmable).

Chapter 9

Preliminary Tests for the SDD ASIC

9.1 The feasibility tests

The packaged ASIC previously described is mounted on a board made by INFN-Bo and tested. This chapter focuses on the preliminary tests performed at the INAF-IASF section of Bologna, in collaboration with the INFN of Bologna.

As described in Figure 9.1, the PCB was projected to be connected to a National Instrument board, in order to configure properly the ASIC and record the results. The main features are:

(a) the Input pins for the ASIC configuration;

(b) the connector for the I/O configuration and handshaking commands to the NI board;

(c) the I/O pins for the handshaking commands;

(d) In test pulses, with a capacitance of 0.25 pF;

(e) the Output channels pins without buffers;

(f) the Output buffered channels for the NI connection.

In order to work properly, some modifications needed: the value of the resistor buffers were changed and some voltage regulator were moved on an adjacent board. In this first version only 8 out of 32 channels were bounded in the chip's package, as we can see in Figure 9.2. For the pin list of the packaged ASIC please refer to Appendix B.

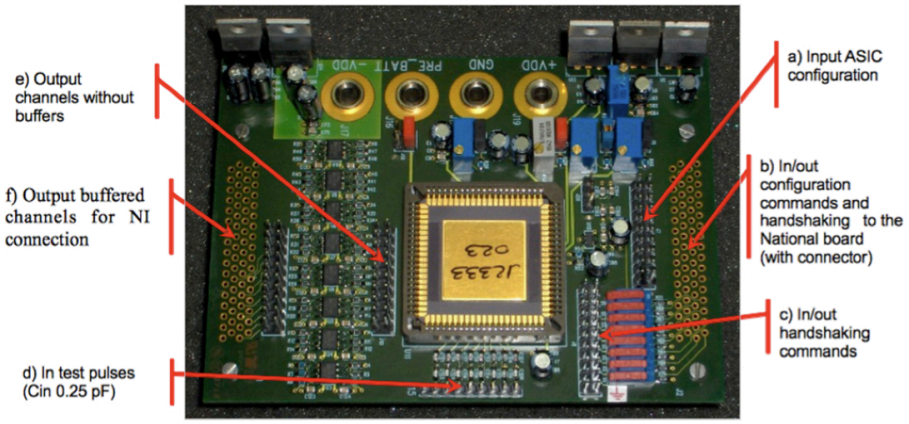

Figure 9.1: The board for the ASIC testing with the NI connectors.

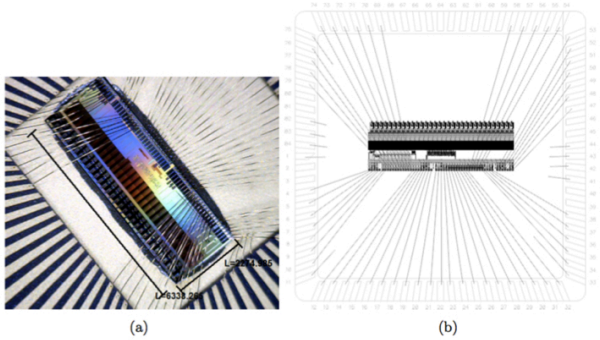

Figure 9.2: (a) bonding onto the ceramic socket and (b) relative bonding scheme.

9.1.1 Operating Method of the ASIC

In order to make the ASIC working properly, these operations are needed.

1. Setting the configuration register of the ASIC.

   This is done by sending a 216-bit word on the configuration connector pins (Figure9.1a,b). The pins interested in this operations are:

   - EN_WR
   - CK
   - DATA_SERIAL_IN

   The word is send on pin DATA_SERIAL_IN following the time scheme reported in Figure 9.3. On the positive edge of the CK signal the DATA_SERIAL_IN is read by the register. On the negative edge the DATA_SERIAL_IN can change with the successive value.

2. Handshaking for *Data Reading*.

   - This can be done when the internal Trigger is ON. If the DISC_DIS is inactive (i.e. the discriminator is active), and the input signal exceeds the threshold, a Trigger signal is emitted by the ASIC;
   - Depending on the ASIC configuration, on the output connector (Figure 9.1e) there is the proper signal (if the PRE_DIS is inactive), that is at the shaper or stretcher output.
   - a RESET signal is sent to the ASIC. This signal has an offset of 1.5 V and amplitude of 370 mV.

If the configuration is set for *shaping mode*, the reset has no effect. On the output pin there is the signal out of the channel amplifier. If the configuration is set for *stretching mode*, the output of the shaper is held at the relative input amplitude until the reset is given to the ASIC. **Note:** the ASIC provides two input for the reset signal: one is the $ASYNC\_RESET$ that reset all the channels; the other one is the EOC (End Of Conversion) signal.

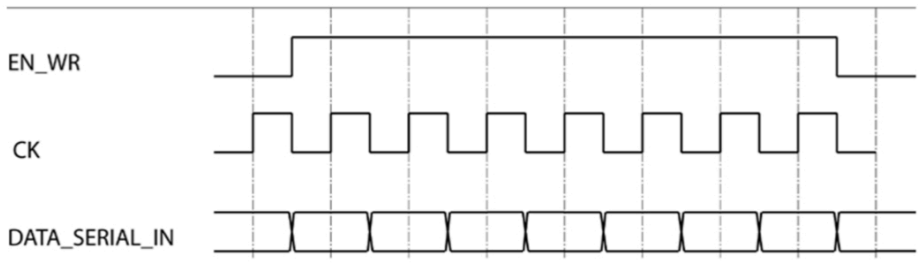

Figure 9.3: Timing of the digital signal

9.1.2 Signal Generation

In order to test the ASIC properly, for this first phase tests we did not used the SDD detector. In order to simulate the charge produced by the SDD detector, at the input stage (Figure 9.1) there are two series capacitors of 0.5pF each, for each input channel (8 in this ASIC version). Then, a signal generated from a negative pulse generator (BNC) is sent to the input stage. The signal generated for these measurements has the following characteristics:

Parameter	$Value$
Polarity	$Negative$
Raise time	$1\mu s$
Fall time	$1ms$
Frequency	$250Hz$

Table 9.1: Signal characteristics at the ASIC input stage.

9.1.3 The National Instrument Test Equipement (TE)

The "official" Test Equipment (TE) is realized with two National Instruments board. As shown in Figure 9.4, the TE is composed of:

- a board with digital I/O for the ASIC configuration and the control of the ASIC's MUX. The output signals range between 0 to 5 V;

- a board with digital and analog I/O (8 inputs) and an FPGA that has to control the handshaking protocol and the ADC conversion of the output channels;

- the buffers for driving the TRIGGER_MUX_OUT signal to the NI board and the adaption for the ASYNC_RESET signal.

A dedicated software was developed for the NI board control and data acquisition. The ASIC Test Equipment Software (TE) is implemented with the graphical development environment LabView National Instrument. The TE software design is based on *event-driven* programming and *state machines*. The recurrent structure is driven by a state machine capable of: initializing; waiting for an event generated by the user; data saving; panel closing. The presence of the FPGA requires FIFO communication buffers. In order to avoid communication errors between the TE and the ASIC, the configuration was splitted in two distinct processes: the storage of the configuration word on the FPGA; the bitstream transmission from the FPGA to the ASIC.

The main panel (Figure 9.5) opens when the TE software runs. From this panel it is possible to choose one of the four possible actions:

- *Application Configuration.* It opens the control panel for the software configuration.

- *ASIC Configuration.* It opens the ASIC configuration panel where is possible to choose the word to be load in the ASIC shift register.

- *Start Acquisition.* It stars the data acquisition from the ASIC.

- *Quit Application.* It stops the application.

- *Settings Fixed/Manual.* It chooses whether to load a previous ASIC configuration or to access manually.

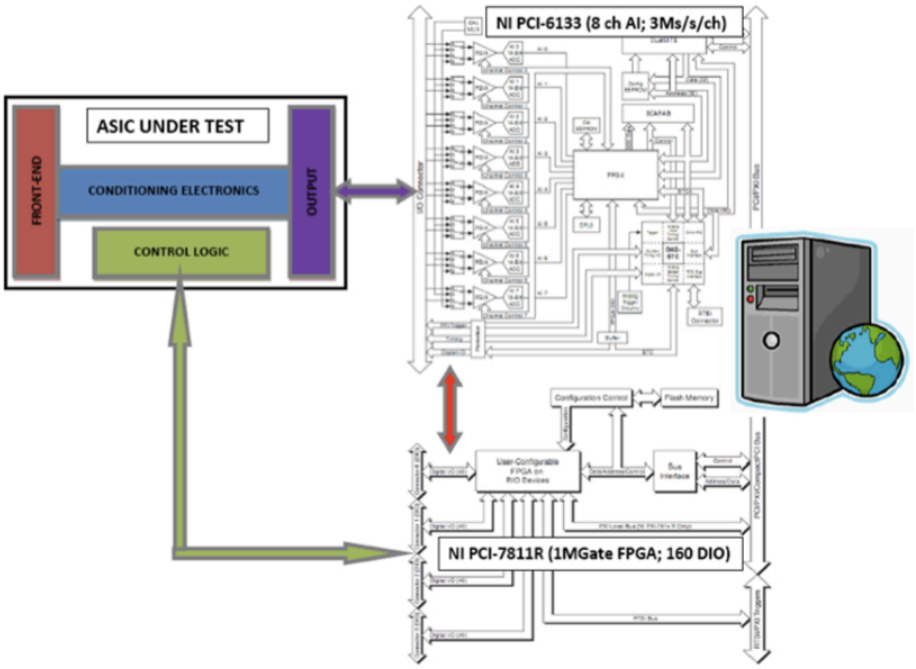

Figure 9.4: Logic diagram of the NI Test Equipment.

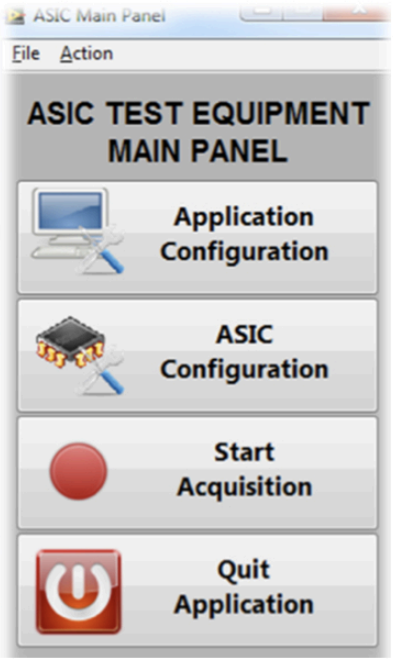

Figure 9.5: Test equipment main panel.

Application Configuration. As we can see in Figure 9.6, in this panel it is possible to configure the software options.

- *Data Folder.* Selects the folder where data acquired from the ASIC are saved.
- *ASIC Configuration File Path.* Selects the folder where the ASIC configuration file is saved.
- *Save Changes.* Saves the options in the software configuration file.
- *Close panel.* Closes the software configuration panel.

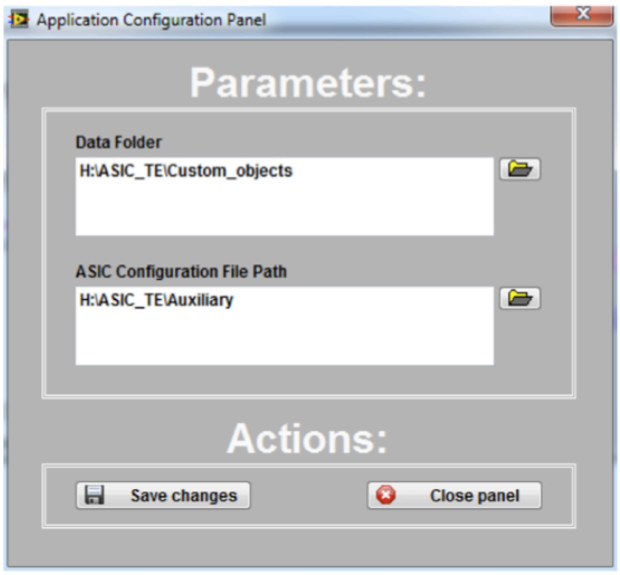

Figure 9.6: Configuration panel of the general software options .

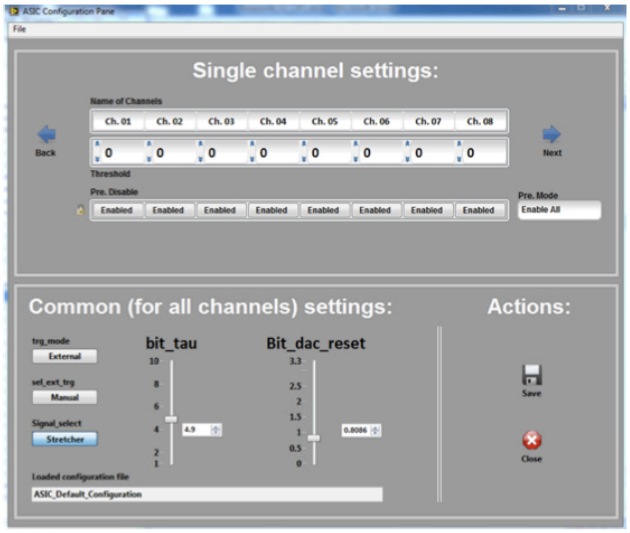

Figure 9.7: ASIC configuration panel.

ASIC Configuration Panel. The Figure 9.7 represents the ASIC configuration panel. The chosen parameters are sent to the ASIC by the digital output of the NI PCI-7811R board equipped with an FPGA. The controls are divided in two groups: *Single Channel Settings*, where it's possible to choose for each channel which pre-amplifier and threshold- discriminator are active and the value of the fine threshold value; *Common*, where it's possible to choose the parameters common to all channels:

- *trg_mode.* selects the internal or external trigger;
- *sel_ext_trg.* when the external trigger is selected, itÕs possible to choose the kind of trigger used (manual or 32-channel-OR);
- *signal_select.* selects which signal is send to the output of the ASIC, from the stretcher or shaper;
- *bit_tau* selects one out of eight shaping time;
- *bit_dac_reset* selects the value of the parameter bit_dac_reset.
- *threshold* selects the value of the main threshold.

In the graph at the bottom of the figure it is possible to see the bitstream sent to the ASIC shift register, from the MSB to the LSB. From the save button it is possible to save the configuration. When the panel is closed from the close button, the bitstream is sent to the ASIC and it is possible to start the acquisition.

Acquisition Panel. Once the ASIC configuration process is done, then it's possible to start the data acquisition. The acquisition is performed by the NI PCI-6133 board, with 8 analog inputs working up to a frequency of 3MHz. The acquisition is synchronized by a trigger signal from the ASIC: this signal is sent to the FPGA that store the temporal information in a counter, hence to the NI PCI-6133 that performs the acquisition. Due to the presence of a MUX output on the ASIC, the first channel of the NI board is wired to the MUX output, that has to be controlled by five digits from the FPGA, acquiring 32 times for each acquisition process. The other seven channels of the NI board are wired directly to the seven outputs of the ASIC. When *Acquisition Start* button is pressed, a screen as shown in Figure 9.8 appears. The graph shows the selected output from a menu on the top of Figure 9.8. The different colors refer to the different channels and the MUX channel. It is possible also to set the reset delay and duration, the acquisition time and the path and file name to save data.

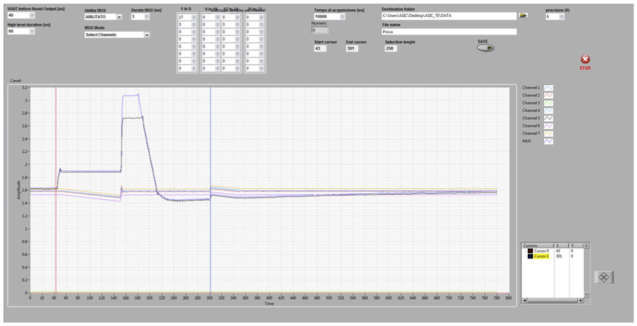

Figure 9.8: Screenshot of the acquisition panel window.

9.1.4 Pattern Generator Test Equipment (PG)

In order to have the possibility to limit any possible disturbance that the TE may introduce, we have held another simpler Test Equipment setup. This test equipment is composed of:

- *Pattern Generator.* (from now we'll refer to this with PG, to differ from the National test equipment, called TE) that send the configuration bitstream to the input pins on the PCB (Figure 9.2). The timing sequence is the same as the one in Figure 9.3;
- *BNC.* the pulse generator.
- *PH.* a pulse generator for the ASYNC_RESET signal, with an offset of 1.5 V and amplitude of 400 mV.
- an *oscilloscope* for recording the data.

9.2 Qualitative Behavior of the ASIC with the TE

In this first test measurements we tested the different functionalities of the ASIC and software. First we saw that the software works properly: the ASIC responds correctly to the different configuration settings (shaping time, threshold, enabling/disabling the different channels, shaping/stretching mode). Then we valued the behavior of the ASIC in a common operating situation (ref to Table 9.3), with an input at the middle of the dynamic range. Once the ASIC has been configured and the acquisition starts, we have a graph as shown in Figure 9.8. In this figure we can see the output of the eight channels bonded to the ASIC. The blue line is the output of the channel 16, the one tested. We can immediately notice two unexpected behaviors: first, the presence of on *offset* of about 0.8 V; second, a sort of *"saturation"* effect on the output signal after a certain period of time. In

order to better understand this, we configured the ASIC in *shaping* mode. We can see the result in Figure 9.9. In the image taken with the oscilloscope, we can see the signal out of the shaper (yellow line) and the trigger generated by the ASIC (blue line). On the rising edge of the trigger, we can see that there is a coupling between the analog and digital signals. This results in lowering the output signal. Instead, on the falling edge, that corresponds to the rising edge of the reset signal, the output signal rises, until it reaches the maximum. So we refer to this effect as a "saturation" effect. This behavior reflect the one that we see in stretching mode (Figure 9.8), suggesting that the stretching mode works properly. In order to try to better understand this issues, we used the PG experimental setup.

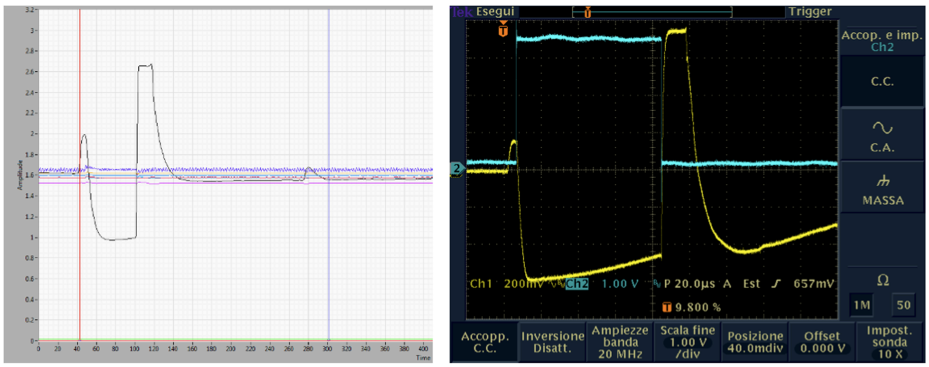

(a) (b)

Figure 9.9: Signal in shaping mode taken with the TE (a) and with an oscilloscope (b) in two similar conditions.

9.3 Qualitative Behavior of the ASIC with the PG - Part I

After the first analysis of the ASIC with the TE, we have seen some disturbs in the output signals. In order to exclude the TE as a source of disturbance, we used the PG Test Equipment. In this case, the PG is wired to the input configuration pins (Figure 9.1a), sending digital signals of 0 V and 3.3 V. The TRIGGER_MUX_OUT signal is taken directly from the I/O handshaking commands pins (Figure 9.1c) and sent as input to the PG for the ASYNC_RESET. We have performed preliminary tests for the ASIC functions:

- *Shaping Mode* with several values of shaping time;
- *Stretching Mode*
- pulse reset effects;
- effects of the *amplitude input signal* on the reset length for the baseline restoration;
- effects of the BIT_DAC_RESET (that affects the polarization of the input FET).

9.3.1 Shaping Mode.

We are now testing:

channel	♯16
BIT_DAC_RESET	0110100000
threshold	255(max)
shaping	*active*

Table 9.2: Test setup.

In Figure 9.10 we can see the output signal (yellow line) and the input pulse (blue line). The shaping time is configured as 010.

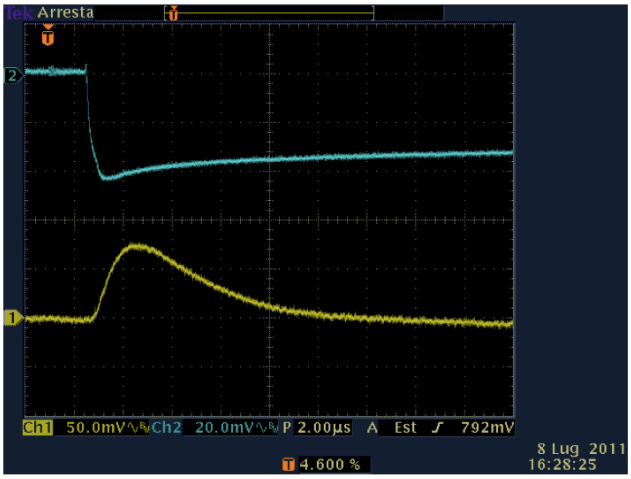

Figure 9.10: Input signal (blue line) and output signal (yellow line) with shaping time 010.

From this first picture we see that the output signal has a good shape and the gain is about 3.1. In the next figures we have the output signal (yellow line) and the reset signal (blue line), generated with the PH, for several values of shaping time. The input signal is kept under the threshold, hence we never see the reset signal. We can see from Figure 9.11f that the input signal exceeds the threshold. The TRIGGER_MUX_OUT signal of the ASIC triggers the PH, giving the proper reset signal. We can also appreciate the effect of the ASIC trigger on the signal of the shaper. We will discuss it later.

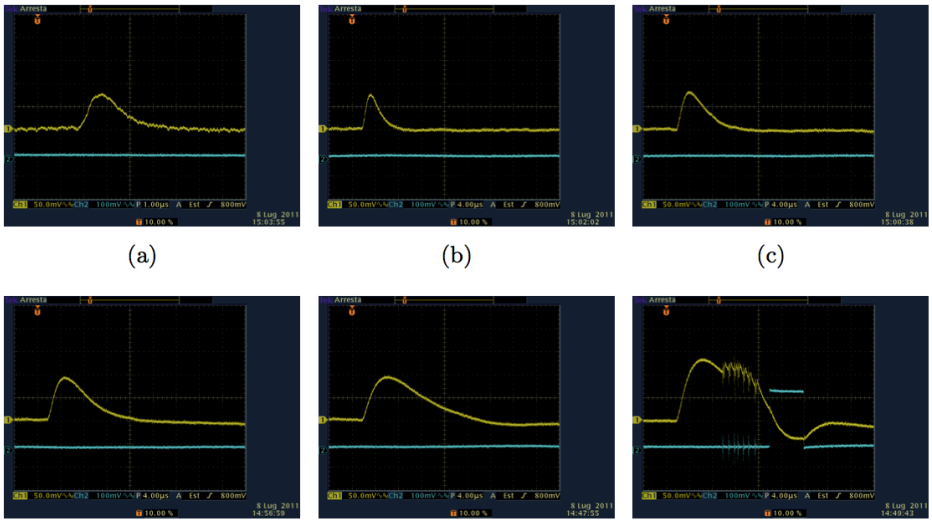

(a) (b) (c)

(d) (e) (f)

Figure 9.11: Output signal (yellow line) and the reset signal (blue line) for a shaping time of (a) 000, (b) 001, (c) 010 , (d) 100 ,(e) 111, (f) 111. The signal of (e) is under threshold, the one of (f) is upper threshold.

9.3.2 Stretching Mode.

We are now testing:

channel	♯16
BIT_DAC_RESET	0110100000
threshold	255(max)
shaping	010
stretching	*active*

Table 9.3: Test setup.

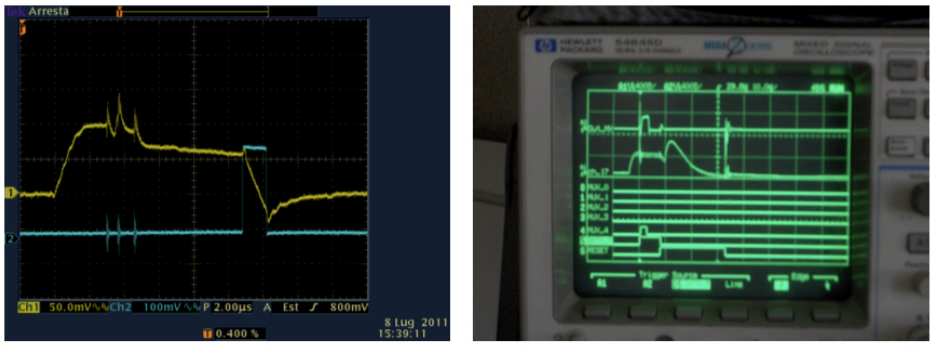

(a) (b)

Figure 9.12: Comparison between the *stretching mode* of the PG (a) and TE (b).

In Figure 9.12a we see with the yellow line the signal out of the stretcher and the signal reset with a blue line. The ASIC seems not to stretch correctly. As a comparison we have in Figure 9.12b the stretched signal with the TE, where the first oscilloscope channel is the output of the MUX, the second one is the output of the channel under test (that correctly stretch the signal, but then saturate); the first five digital signals are the MUX address bits, than there are the TRIGGER_MUX_OUT signal and the RESET (of tenth microseconds length). Two issues arises from these PG measurements:

- the ASIC under test with the PG seems not to stretch correctly. The graphs

suggest that one possible cause may be the TRIGGER_MUX_OUT signal used for triggering the PH: it is necessary to introduce a buffer stage in order to have a correct load of the signal by the PH in order to avoid this disturbance.

- the ASIC under test with the TE seems to stretch correctly (with the trigger signal properly buffered), but with the reset signal the output channel "saturate", and needs a reset duration of more than $50\mu s$ to avoid this oscillations.

9.3.3 Effects of the *reset length* on the output signal

In the next pictures (Figure 9.13) we have the output signal (yellow line) and the reset signal (blue line). We valued the effect of the reset duration on the output signal.

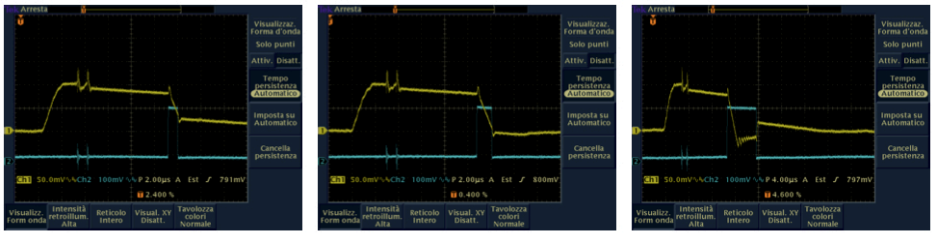

(a) (b) (c)

Figure 9.13: Effect of the reset length on the output signal (Cif. Table 3)

bit_dac_reset	shaping time	reset length (μs)	Figure 9.13
0110101011	010	0.8	(a)
0110101011	010	1,6	(b)
0110101011	010	5	(c)

Table 9.4: Different reset length values for the Figure 9.13

9.3.4 Effects of the *amplitude input signal* on the reset length for the baseline restoration.

In the next figures (Figure 9.14) we can see with the yellow line the output signal and with the blue line the input pulse on the capacitance of 0.25 pF. The bit_dac_reset value is 0110101011 and the shaping time 010.

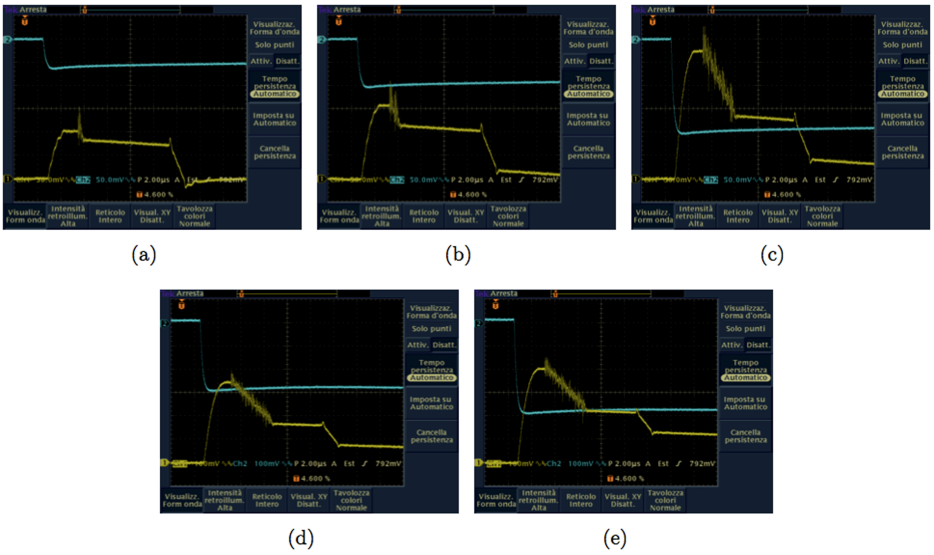

Figure 9.14: Effect of the amplitude signal on the output signal.

9.3.5 Effects of the bit_dac_reset value.

We present (Figure 9.15) the effect of different bit_dac_reset values on the output signal of the shaper, with a shaping time of 010 and an input signal under threshold in order to avoid the disturbance of the trigger signal.

bit_dac_reset	Figure 21
0110101011	(a)
0110100000	(b)
0110000000	(c)
0100110000	(d)
0100000000	(e)

Table 9.5: Different bit_dac_reset values for the Figure 9.15.

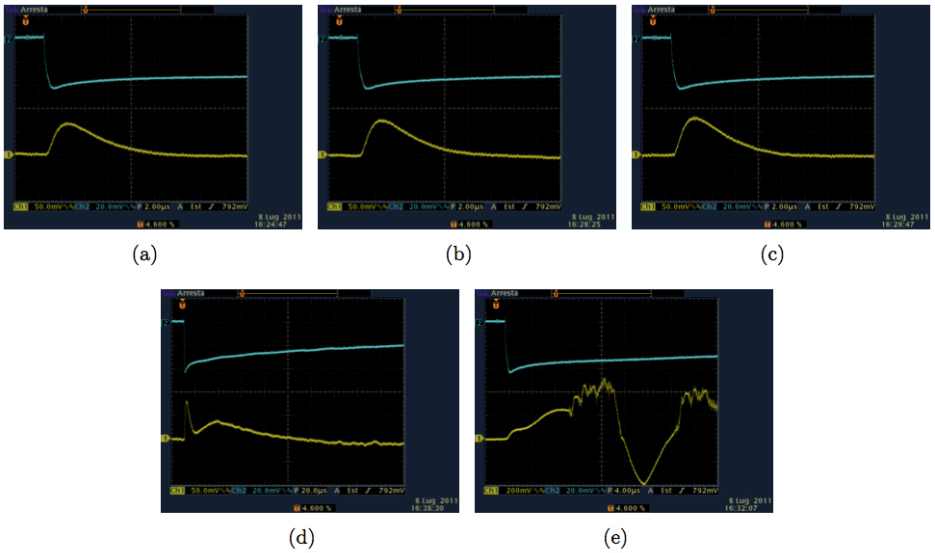

Figure 9.15: Effect of the bit_dac_reset on the output signal.

In conclusion, with the PG test equipment we tried to avoid any kind of disturbance that the experimental setup may introduce, as seen with the National Instrument TE. Although this, we still see this disturbance. One of these is the effect of the TRIGGER_MUX_OUT on the output signal: if we don't use a buffer stage at the exit of the ASIC we see that the PH load too much the signal, introducing disturbance. Another important effect, that we have already see with the TE, is the effect of "saturation": when the ASIC receive a signal upper threshold, it generates the TRIGGER_MUX_OUT signal. This signal couples with the analog line, producing an effect of saturation on the output signal.

9.4 Qualitative Behavior of the ASIC with the PG - Part II

We see from the previous section that the main causes of disturbance on the output signal are the TRIGGER_MUX_OUT signal and the absence of a buffer stage before the PH for the generation of the ASYNC_RESET signal. In order to avoid the latter one, we decided to not take anymore the TRIGGER_MUX_OUT signal directly from the ASIC, but rather to impose a fixed delay on the PH, that take the trigger signal from the BNC directly. In this way we can reproduce the same conditions as taking the trigger signal from the ASIC, but completely avoiding any disturbance on the output signal. With this little change, we saw a similar behavior as with the TE. For this testing we had also another ASIC to test3: in this version the pins 23, 35, 37 are directly bonded to a proper digital supply directly on the ASIC package, instead making some modify on the PCB. From now we'll refer to the latter ASIC as the *Second* ASIC, and to the other one as the *First* ASIC.

9.4.1 ASIC Configuration

For this series of tests we used the following configuration:

sel_ext_trig	1
trig_mode	0
threshold	11111111
bit_dac_reset	0110101011
bit_tau	101

Table 9.6: ASIC configuration for the PG-Part II tests.

We decided to analyze several behavior for both the ASICs, and for simplifying the notation we divided this procedure in **STEPS:**:

- **STEP 0:** the signal out of the *shaper* with the pre_disc set to 1 for *all the channel* (i.e. disabling the discriminator and so the logic part for all the channels);
- **STEP 1:** the effects of the TRIGGER_MUX_OUT and ASYNC_RESET signals at the shaper output;
- **STEP 2:** comparison between the EOC and ASYNC_RESET signals;
- **STEP 3:** behavior of the shaper output with the reset signal;
- **STEP 4:** 'saturation' effect during time.

For this tests we just valued the qualitative behavior of the ASIC, so we used an input signal in order to be at about half of the output range or in such a way to emphasize the effect. In all the next pictures the yellow line represents the output signal.

9.4.2 First-ASIC Testing

Step 0. We started valuing the output of the shaper by disabling the discriminator (pre_disc set to 1 for all the channels).

As we can see from Figure 9.16, the output signal has the correct shape. By varying the input signal with the BNC, the output amplitude varies as well, keeping the same shape (not shown here).

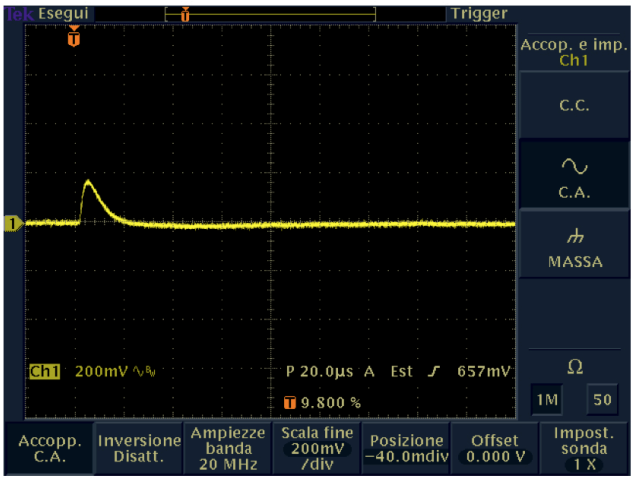

Figure 9.16: Output of the shaper disabling the discriminator..

Step 1. We now enable the discriminator.

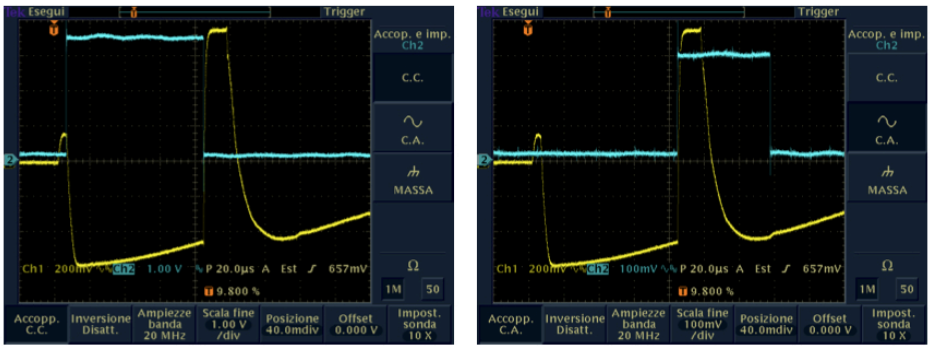

(a) (b)

Figure 9.17: Output of the shaper enabling the discriminator (yellow line) with (a) the TRIGGER_MUX_OUT and (b) the ASYNC_RESET signals (blue line).

The signal now exceeds the threshold, and the ASIC produces the TRIGGER_MUX_OUT signal (Figure 9.17a). As we can see from the picture, the rising edge of the trigger signal affects the output of the shaper, by lowering the signal for all its duration. After a certain delay, the PH generates the reset pulse: the TRIGGER_MUX_OUT signal correctly goes down on the

rising edge of the reset, but again the output signal is disturbed, showing that saturating behavior as already mentioned.

Step 2. For all the other test we only used the ASYNC_RESET signal. By sending the reset on the EOC pin, we can see from Figure 9.18 that the effect is the same.

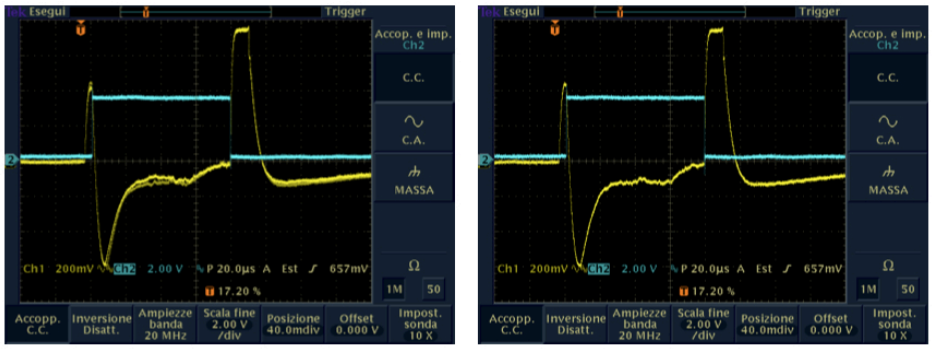

(a) (b)

Figure 9.18: Comparison between (a) the ASYNC_RESET and (b) EOC signals (blue line).

Step 3. We now consider the shaper output.

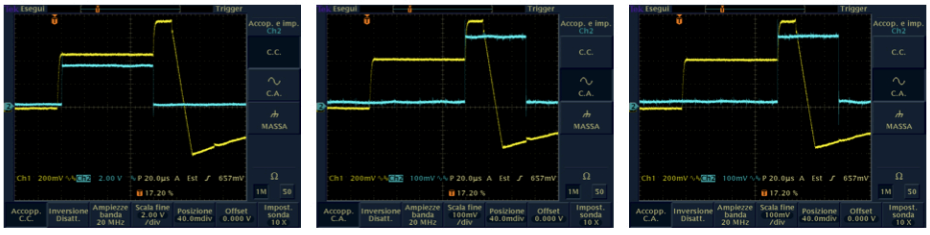

(a) (b) (c)

Figure 9.19: Output of the shaper with (a) the TRIGGER_MUX_OUT, (b) ASYNC_RESET and (c) EOC signals (blue line).

This effect is the same as seen with the TE (Figure 9.12b). By comparing Figure 9.19a with Figure 9.18a we see that the ASIC stretches correctly: when the trigger is high, and the output of the shaper goes down, the stretched signal keeps its value; on the rising edge of the reset the shaped signal saturates,

as well as the stretched one. The effect of the ASYNC_RESET and EOC signals are the same. Another aspect not reported in this figures is that if we set a reset length too short, the saturated signal doesn't discharge completely, and the signal goes down with the characteristic time of the component (the capacitor C_f).

9.4.3 Second-ASIC Testing

We have made the same measurements with the second ASIC. We found the qualitative behavior was the same. We now summarize the images of the several steps (Figure 9.20). We omitted the ones of step 2 because are the same as Figure 9.18.

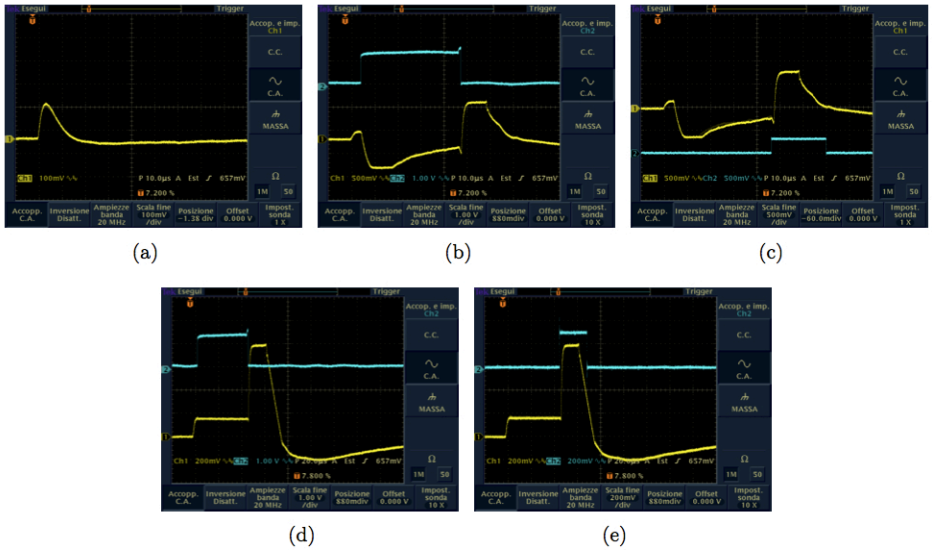

Figure 9.20: Second-ASIC testing results: (a) step 0, (b) and (c) step 1, (d) and (e) step 3.

Step 4. For this ASIC we made another analysis in order to test the behavior saw with the first ASIC with the TE. By turning on the power supply of the ASIC and then configuring it, we can see that the shaper works properly, without the saturating effect. After a certain period of time (few minutes) we can see a disturbance growing on the output of the stretcher, leading to the saturation. In Figure 9.21 we have the signal out of the shaper. The images are taken at about 20" one to each other, starting from the left. This behavior is the same as we saw with the first ASIC with the TE.

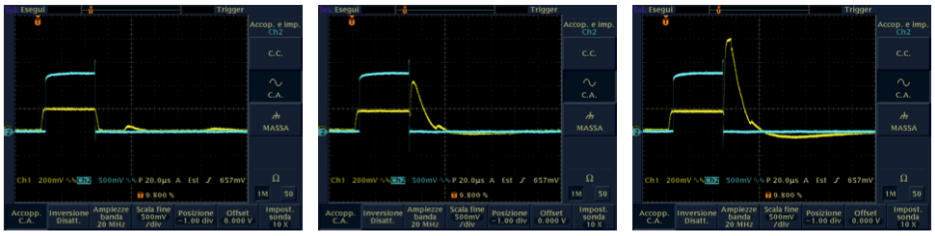

(a) (b) (c)

Figure 9.21: Effect of the second ASIC during time. Images are taken 20 one to each other starting from the left.

Chapter 10

Results

10.1 Noise Measurements

This chapter presents the noise, linearity and gain results, performed with the setup previously described.

For the noise measurements we used the multichannel analyzer MCA-8000A by Amptek, in order to valuate the FWHM of the peak amplitude of some input signals after the preamplifier. To do so we disabled all the discriminators of all channels of the ASIC (also to avoid the disturbance induced by the trigger signal). The MCA accepts signals of at least 15 mV amplitude, in a range of 0 to +5 V (Z_{in}=200 kΩ) or 0 to +10 V (Z_{in}=2 kΩ). We used the first one.

Our first issue is to adapt the output signal of the ASIC with the MCA. Indeed, the output signal has an *offset* of about 0.81 V and an amplitude of hundreds mV. We did in two ways: the one first using two dual-sum-inverter amplifier (DSIA), using both the positive and negative outputs after the buffer stage on the PCB (Figure 9.1f) making the proper connections; the second one by making a dedicated circuit (Figure 10.1) with two operational amplifier (OP37) and taking the signal at the output stage without buffers. The main features of the circuit are:

- the V_{offset} is made with a voltage divider from a +8 V source;

- capacitors for stabilizing the Source Voltages;

- a complessive gain of 25 ($5 \cdot 5$).

With this two configurations we have the proper signal (shifted and amplified) ready to be analyzed by the MCA. For each configuration we acquired three or four input signals with the MCA (depending of the MCA range). Each signal was taken for *every shaping time* (i.e. 8 values). The *resolution energy* of the system, that is defined as

$$R = \frac{\Delta E}{E} \tag{10.1}$$

where ΔE is the FWHM of the signal. In order to determine E correctly, that is the channel number of the MCA, we performed a linear fit of the data. Finally we calculated the ENC.

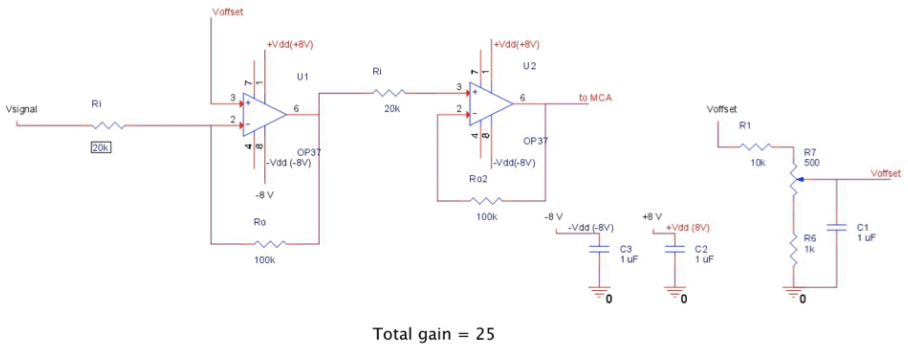

Figure 10.1: Adapting circuit for the output signal to the MCA.

First Configuration - DSIA. We used four input signals: 30, 60, 90 and 150 mV input signal. For each input signal, the MCA acquired for 60 seconds. In Table 10.1 we have summarized the results.

30 mV		60 mV		150 mV		300 mV	
($4.6811 \cdot 10^4$ e$^-$)		($9.3622 \cdot 10^4$ e$^-$)		($2.3406 \cdot 10^4$ e$^-$)		($4.6811 \cdot 10^4$ e$^-$)	
FWHM (e$^-$)	R (%)	FWHM (e$^-$)	R (%)	FWHM (e$^-$)	R (%)	FWHM (e$^-$)	R (%)
7710	19.3	12719	12.8	12921	5.0	13620	3.0
5784	18.0	5476	5.7	6073	2.4	8609	1.9
6523	20.8	5896	6.2	6808	2.6	8191	1.8
8952	34.4	6856	7.4	7255	2.8	8439	1.9
8531	31.1	7074	7.6	7179	2.8	9497	2.1
10209	39.2	7867	8.5	8714	3.3	8799	1.9
10234	39.4	9820	10.6	8399	3.2	10471	2.3
11354	45.7	11739	12.8	9096	3.5	10376	2.3

Table 10.1: Noise measurements using the DSIA configuration (60" per input pulse).

For each input value we report the relative FWHM and resolution (percentage). Then we calculated the ENC.

As we can see from the plots of Figure 10.2 we have the best noise performances for middle shaping times and middle input charge. The ENC presents a minimum, but the value in the best case is too much (2000 e$^-$r.m.s.).

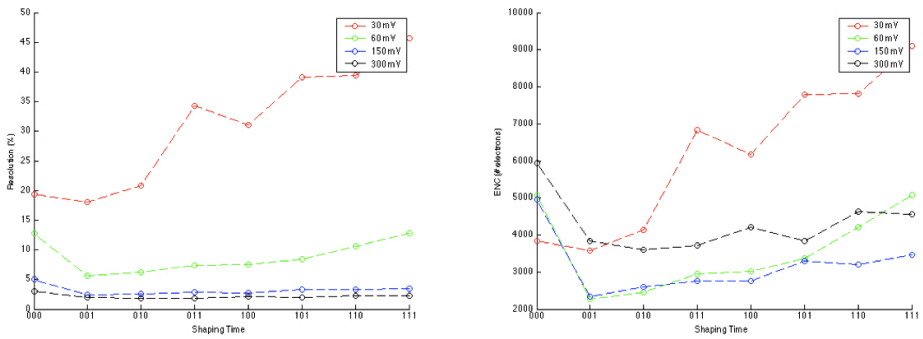

(a) (b)

Figure 10.2: Resolution (a) and ECN (b) for each input signal.

Second Configuration - OP In order to perform a better measurement, we implemented the circuit sketched in Figure 10.1. Now we have a different amplification factor. Hence we found other voltage input values and we changed also the dynamic range of the MCA, switching to 10 V scale. For these measurements we used an acquisition time of 120 seconds.

15 mV		30 mV		75 mV		150 mV	
(3.75 fC)		(7.5 fC)		(18.75 fC)		(37.5 fC)	
FWHM (e^-)	R (%)	FWHM (e^-)	R (%)	FWHM (e^-)	R (%)	FWHM (e^-)	R (%)
4168	18.4	5581	11.8	6472	5.4	6350	2.7
3416	16.9	3592	7.6	3689	3.0	4136	1.8
3546	17.6	3881	8.2	3911	3.2	4455	1.9
4168	21.4	3633	7.8	3869	3.1	4519	2.0
4166	20.9	4137	8.8	4254	3.5	4276	1.8
4260	21.5	4281	9.1	4610	3.7	4719	2.0
4762	24.4	4596	9.8	4916	4.0	5170	2.2
5318	27.6	4764	10.1	5236	4.2	5482	2.4

Table 10.2: Noise measurements using the OP37 configuration (90" per input pulse).

As before, we calculated the resolution and ENC. The graph results can be seen in Figure 10.3.

With this experimental setup we have both better resolution and ENC values. For high input values we have a quite good energy resolution (few point percents), but became worst as the input charge decrease. This is probably due to the presence of the offset: with an input signal of 15 mV we have an output quite near to the offset value (we roughly estimated a lower limit of few mV). Thus, this offset limits the dynamic range of the system. The ENC calculation shows now a better shape, with a clearer minimum around 1μs (that is bit_tau=001). In the best case we have an average of 1600 e^- r.m.s., that is better than the previous measure, but quite far from the desired value (almost 2 order of magnitude).

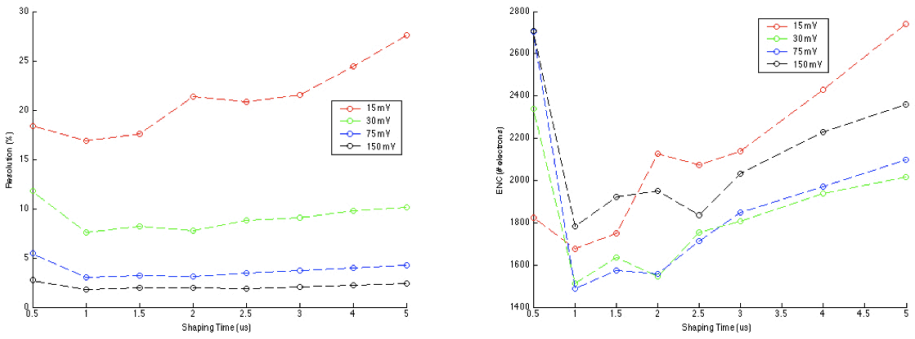

(a) (b)

Figure 10.3: Resolution (a) and ECN (b) for each input signal.

10.2 Linearity

We valued the linearity of the system for the different shaping times. We used the following values:

Input Pulse (mV)	Q (fC)	Energy on Si (keV)
15	3.75	84.5
30	7.5	169
75	18.75	422.5
150	37.5	845

Table 10.3: Input test values.

As an example we report the result for one shaping time ($\tau = 0.5\mu$ s). We summarize the results in the table 10.4.

Shaping time (μs)	χ^2
0.5	0.14
1	4.21
1.5	4.43
2	4.26
2.5	3.26
3	3.57
4	3.12
5	2.71

Table 10.4: Summary of the results for the linearity test.

We can see from this results that the linearity is not perfect.

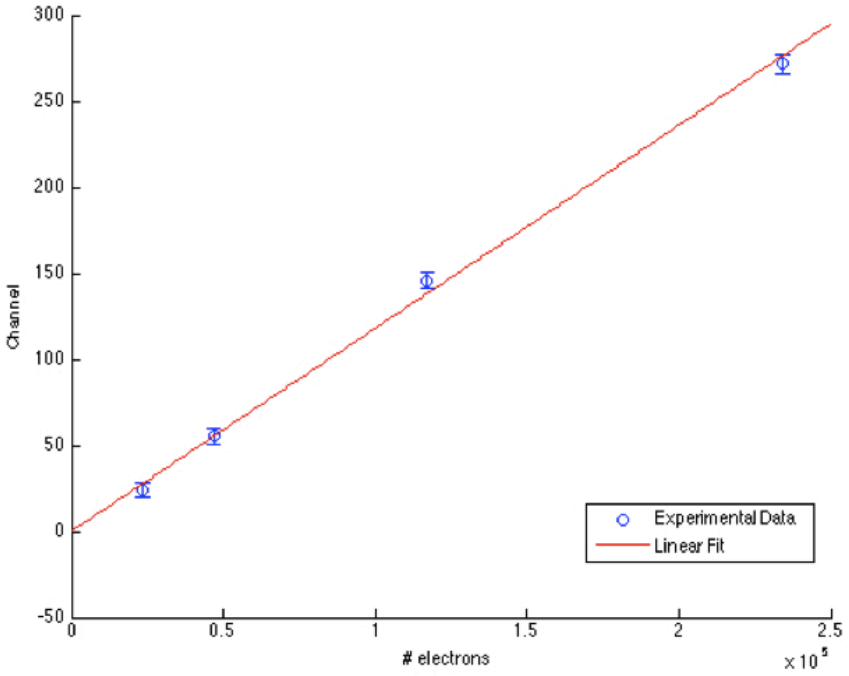

Figure 10.4: Linearity results for $\tau = 0.5\mu$s.

10.3 Gain Measurements

Another important parameter to test is the value of the voltage applied to the MOSFET in the feedback network, that is the bit_dac_reset. From qualitative measurements, we found an operative range of values to test. From the previous calculations, we decided to use a value of 1μs for the shaping time. The MCA range is set as before (10 V) and we used the offset removal circuit as described previously, which is now part of the electronics.

For determining the gain, expressed in terms of mV/fC, we performed a linear fit as before (ch = a + b $\cdot$ Qin), and calculated the gain as:

$$R = b \cdot \frac{mca_r}{mca_{ch}} \cdot \frac{1}{A_{off}} \tag{10.2}$$

where b is the results of the linear fit for each configuration, mca_r = 10V is the dynamic range of the MCA used, $mca_{ch} = 512$ is the number of channels of the MCA, and $A_{off} = 25$ is the amplification of the offset removal circuit. The result is expressed in mV/fC. The range of the bit_dac_reset is from '0101010100' (decimal = 340) to '0111001100' (decimal=460) with steps of 12. The results are reported in Table 10.5. The value of the FWHM was taken as the error.

In Figure 10.5 we can se the graph of the gain vs bit_dac_reset. We can see that for values between 340 and 412 we have a linear behavior, than it rapidly goes to zero. This means that increasing the value of the voltage applied to the reset transistor gate (that acts like a resistor), the discharge time of the feedback capacitor C_f decrease. Thus, C_f cannot reach its maximum, resulting in a lower gain value.

We valued also the resolution and ENC (Figure 10.6) vs bit_dac_reset.

We have a quite good resolution for high input values, as we saw before. It is interesting to see that we have a minimum for the ENC, that corresponds to a decimal value of about 388 and is in the linear region of the gain.

Since the gain depends on the feedback capacitor C_f , we estimated its value. The results is

BIT_DAC_RESET	(decimal equivalent)	GAIN (mV/fC)	error (mV/fC)
0101010100	340	5.0	0.2
0101100000	352	5.0	0.2
0101101100	364	5.1	0.2
0101111000	376	5.2	0.2
0110000100	388	5.0	0.1
0110010000	400	5.1	0.2
0110011100	412	5.0	0.2
0110101000	424	4.7	0.2
0110110100	436	4.0	0.1
0111000000	448	3.1	0.1
0111001100	460	1.8	0.2

Table 10.5: Gain results for different values of the parameter bit_dac_reset.

$$C_f = (200 \pm 10) fF \tag{10.3}$$

that is about 50 fF higher respect the value of the specifications (150 fF).

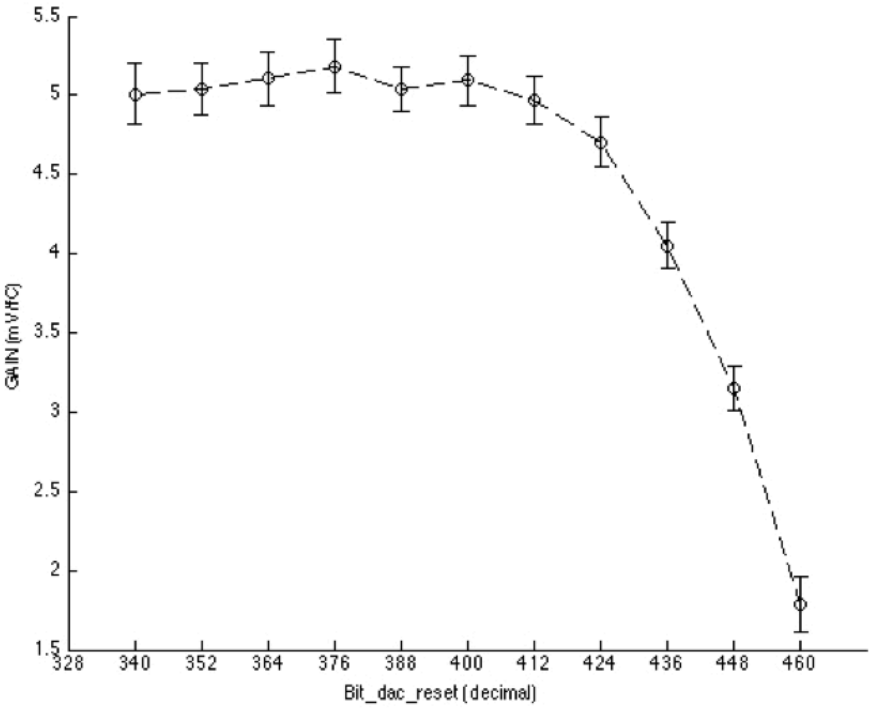

Figure 10.5: Gain vs bit_dac_reset.

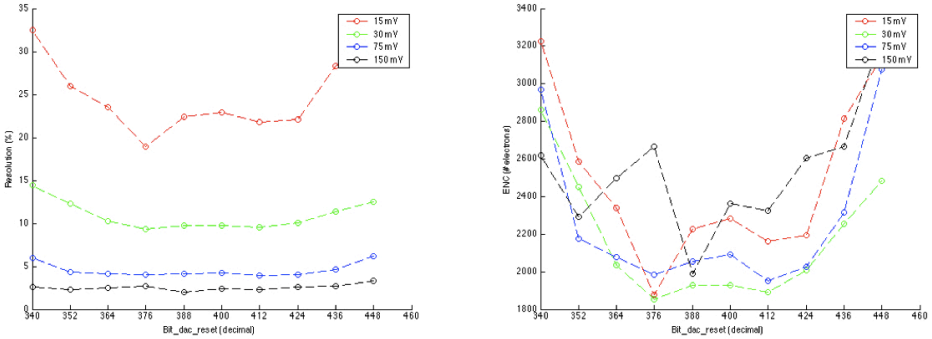

(a) (b)

Figure 10.6: Resolution (a) and ENC (b) vs bit_dac_reset.

Chapter 11

Discussion and conclusion

At the INAF-IASF section of Bologna, in collaboration with the INFN of Bologna, is held an experimental setup for the preliminary tests on the first version of the ASIC for the LOFT project. We were able to held up two different experimental setup: one with the National Instrument boards with a dedicated LabView software; one with a simpler configuration for noise measurements, with the use of a Pattern Generator and a MCA. The results of this first run ASIC clearly show several issues. First, we have a coupling of digital and analog signals. For this reason we had to disable all the logic stage for further measurements. Second, there is an offset of about 0.81 V at the output of the ASIC. This limits the dynamic range of the system. This offset can be caused by an inductive coupling of some nets (as stated from simulations), or by some glitch that prevent the complete discharge of the feedback capacitor C_f . All this problems can also be due to the different type of silicon bulk used for this run. The work continues with the aim to solve these problems and make large-area multi-anode SDDs coupled with low-noise, low-power integrated FEE suitable for space astrophysics and medical applications. Here, low resources in terms of weight, volume, and power, combined with good energy and position resolution, and large sensitive area are usually required. In the following sections a brief description of space and medical applications is presented.

11.1 LOFT ESA Mission

Large-area SDDs with low-noise, low-power ASIC readout are the fundamental keys to LOFT, the Large Observatory for X-ray Timing, (12) a new medium-class space mission that the European Space Agency has been assessing since February of 2011. The LOFT project was proposed as part of the Cosmic Vision Program (2015-2025). The LOFT payload consists of a Large Area Detector (LAD) (13), and a Wide Field Monitor (WFM) (14). An up-to-date table summarizing the anticipated performances of the LAD and WFM is provided on the mission web-site (15). LOFT is specifically designed to investigate "matter under extreme conditions". By taking advantage of the large collecting area and fine spectral resolution of its instruments, LOFT will exploit the technique of X-ray timing combined with spectroscopic measurements. The LAD instrument is a collimated non-imaging instrument performing pointed X-ray observations, mainly in the 2-30 keV energy band. It comprises six panels organized in 21 modules with 16 SDDs (sensitive area of $\sim$76 cm^2) per module. A total of 2016 detectors (i.e., 126 modules) are needed to complete the whole LAD, resulting in a total effective area $>$ 10 m^2 at $\sim$10 keV (geometric area of $\sim$18 m^2). The nominal energy resolution is 260 eV (200 eV achievable for single anode events). The LAD SDDs are equipped with lead-glass collimators [16] to limit the instrument field of view (FOV) to within $\sim$1 degree up to energies of $\sim$30-40 keV. The WFM detector is a coded-mask instrument whose main goal is to scan large fractions of the sky simultaneously to catch interesting targets that can be followed up by the LAD. The WFM comprises five units composed of ten single direction cameras orthogonally arranged. Each camera is equipped with its own coded-mask and four SDDs similar to those employed for the LAD (optimized for imaging purposes). The main operating energy range of the WFM is 2-50 keV. The ten cameras of the WFM together achieve a FOV comprising roughly a rectangular region of 180°$\times$ 90°. The on-board software of the WFM (LOFT Burst alert System) is able to identify and localize bright transient events with $\sim$arcmin accuracy.

11.2 Medical diagnostics

In medical applications, the use of SDDs is suggested for a Compton camera configuration, where the position of the primary interaction is determined by a tracker made of SDD detectors. Compton cameras are used to reconstruct gamma-ray emitting radioisotope distributions. The choice of detector material, the pixel size and the camera geometry all contribute to the overall performance. The use of a tracker made of large-area SDD detectors and ASICs provide an optimal angular resolution and efficiency of the camera. SDDs can also be used in radiology as detectors for X-ray monochromatic beams. A single beam composed of photons with three different energies invests the patient. The SDD, thanks to its high energy resolution performance, can be used in order to discriminate the different energies. In other applications the SDD may also be coated with a scintillator. The range of applications of such an instrument is vast and reaches beyond those of diagnosis in nuclear medicine: monitoring and decommissioning of nuclear power plants, homeland security, and materials study are just few example where a large area SDD can be profitably exploited.

Conclusion

The aim of the present thesis was to study X-ray production and detection for medical and space applications. Following an initial introduction to the projects and their objectives, two projects were presented.
In the first one, a parametric semi-empirical model capable of efficiently reconstructing diagnostic X-ray spectra in 'middle power' computers was developed and tested. In addition, different silicon diode detectors were tested as real-time detectors in order to provide a real-time evaluation of the spectrum during diagnostic procedures. This project contributes to the field by presenting an improved simulation of a realistic X-ray beam emerging from a common X-ray tube with a complete and detailed spectrum that lends itself to further studies of added filtration, thus providing an optimized beam for different diagnostic applications in medicine.
A prototype of the described real-time spectrometer is completely operative at the University of Bologna Physics department. The system is also capable of implementing a dosimetric card, equipped with a microchip, that can automatically register the anatomical region of interest, FOV dimension, tube-patient distance and photon fluence spectrum. This collection of information guarantees patient dosimetry and renders the diagnostic exam precisely repeatable. The system also has the potential to detect the inserted filtration, but we have not yet tested this capability. The project is currently being carried forward in attempt to further improve the accuracy of the measurements and to introduce useful parameters for medical diagnostics, such as the distortion of the size of the focal spot, which depend on the point of

view within the FOV.

In the second project, we performed preliminary tests with a low-noise and low-power ASIC, designed and optimized for analog pulse processing of signals from monolithic large-area SDDs, coupled to a 30.5 cm^2 SDD. The results described in this thesis were obtained as part of the INFN (Bologna Section) project ReDSoX (Research Detectors for Soft X-rays). At the end of this thesis, the final version of the Asic was completed. The results were presented to the European Space Agency and the Commission "LOFT Assessment Study Report (Yellow Book)" can be consulted in the website: http://sci.esa.int/loft/53447-loft-yellow-book/. This project is ongoing, with the aim of using the large-area SDDs with a low-noise, low-power ASIC readout on board the ESA M3 mission candidate LOFT satellite.

Appendix A

X-ray inverter generator

The majority of power supplies used in diagnostic radiology are medium and high frequency power supply, also named inverter generator, which uses an medium-high frequency current to produce nearly constant potential voltage to the X ray tube through a transformer (fig. A.1).

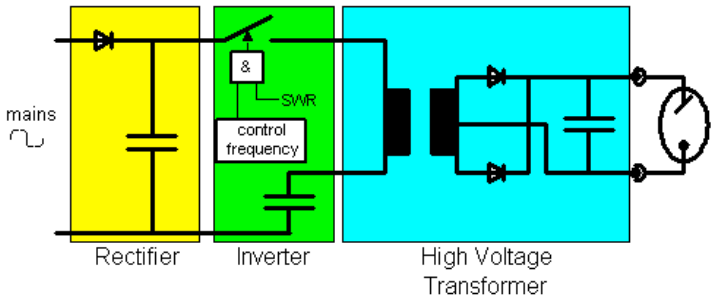

Figure A.1: First approximation of the block diagram of the X-ray inverter generator.

The incoming power supply to an inverter generator may be an ordinary 50 Hz, 220RMS voltage (311 peak voltage). This current is rectified and smoothed and then fed to a chopper and inverter circuit which transforms the smooth, direct current (DC) into a high-frequency (50 - 40000 Hz) alternating current (AC) through some SCR (Silicon Controlled Diode). A transformer converts the high-frequency low-voltage AC into high-voltage AC, which then is rectified and smoothed to provide a nearly constant potential high voltage

to the X-ray tube as shown in figure A.2. The voltage is controlled by varying the frequency of the chopper/inverter circuit, which determines the frequency of the current delivered to the transformer. Fast exposure switching, in the order of 1 ms, is easily obtained with the inverter generator.

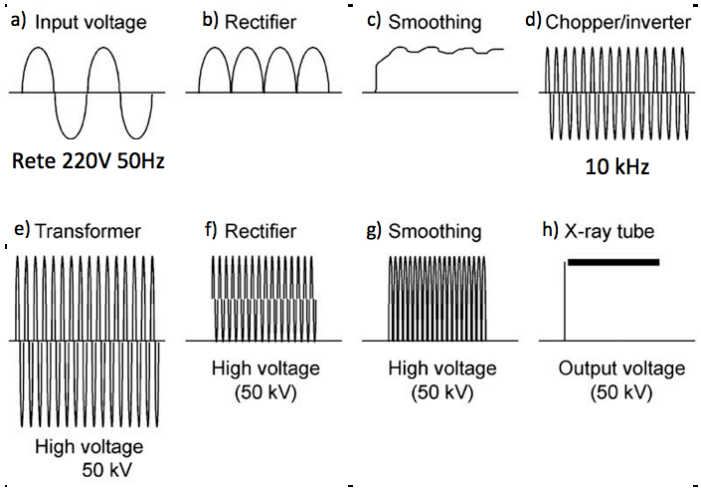

Figure A.2: Waveforms of an X-ray inverter generator.

Given the high frequency, the soft iron is no longer suitable for the realization of the transformer core as the magnetic domains have a friction too high and dissipate most of the energy into heat dramatically reducing the yield. The transformer must be made by ferrite, which present a low hysteresis at the working frequency. With such materials, the performance of the transformer can reach 98% at frequencies of the order of 10 kHz. The block of the transformer - in oil bath for isolation - will therefore be of small size (about 40 cm x 25 cm x 20 cm).

As can be seen in the block diagram of the X-ray inverter generator A.3 the high voltage is controlled by a circuit (called "kVp sense") that shows the output signal from the high voltage transformer to the inverter circuit: this is the feedback of the anode voltage. The circuit takes - through a voltage divider - the high voltage and compares it (in the "Voltage comparator") with the anode voltage set by the operator on the control panel. If the high

voltage is greater than the value set by the operator, then the inverter is "off", the high-frequency signal does not reach more on the transformer and the anode voltage begins to decrease. When the high voltage has reached a value less than that set by the operator, the circuit block "Voltage comparator" provides again the high frequency transformer.

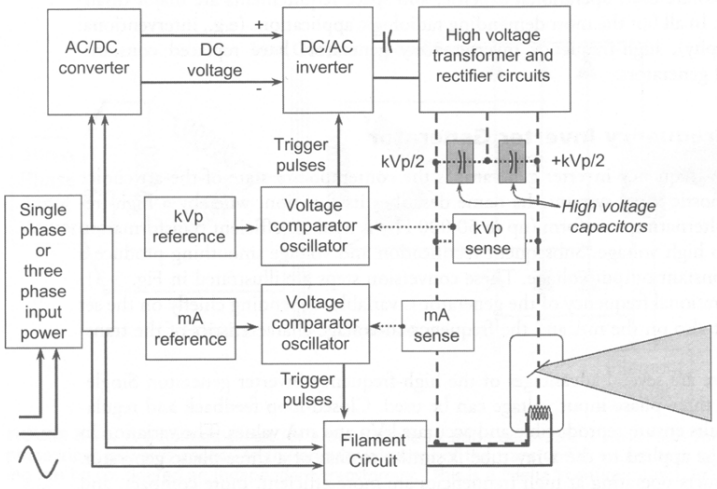

Figure A.3: Block diagram of the X-ray inverter generator.

The following are the feedback circuits A.4 and A.5.

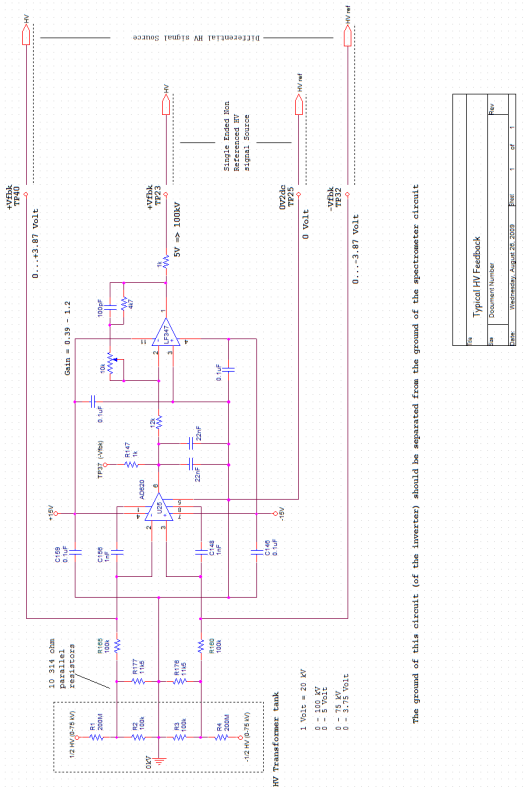

Figure A.4: High voltage feedback circuit.

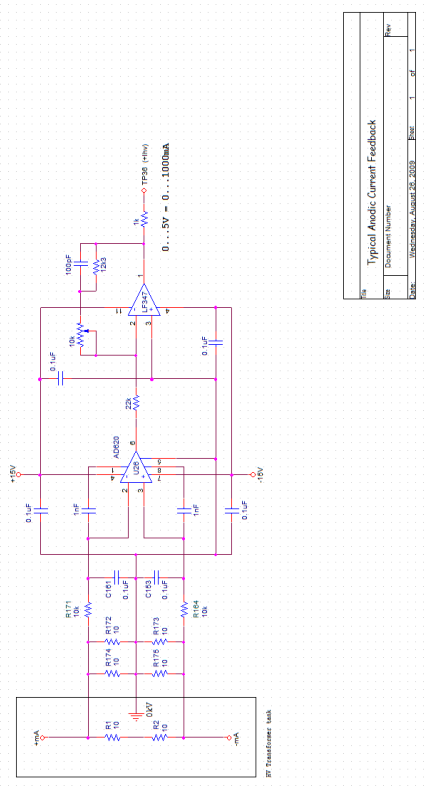

Figure A.5: Anode current feedback circuit.

Appendix B

Pin List of The ASIC

Pin Number	Signal	Pin Number	Signal
1	GND	43	GND
2	NC	44	GND
3	NC	45	NC
4	AGND	46	NC
5	AVDD	47	AVSS
6	AVSS	48	AVDD
7	AVDD2	49	AVSS_PRE
8	AVSS_PRE	50	AVDD2
9	DAC_THR	51	AVSS
10	IBN_250u	52	AVSS
11	GND	53	AVDD
12	OUT_CHANNEL < 19 >	54	EN_WR
13	OUT_CHANNEL_MUX	55	RESET
14	DAC_RESET	56	CK_IN
15	AVDD	57	DATA_SERIAL_IN
16	AVSS	58	TRG_MUX_OUT
17	AVSS	59	NC
18	AVDD2	60	SDC_CELL < 19 >
19	AVSS_PRE	61	SDC_CELL< 18 >
20	DVDD	62	SDC_CELL< 17 >
21	DVSS	63	SDC_CELL< 16 >
22	AVSS	64	SDC_CELL< 15 >
23	DVDD_PAD	65	SDC_CELL< 14 >
24	DVSS_PAD	66	SDC_CELL< 13 >
25	EOC	67	SDC_CELL< 12 >
26	ASYNC_RESET	68	NC
27	EXT_TRG	69	OUT_CHANNEL< 18 >
28	BIT_MUX< 0 >	70	OUT_CHANNEL< 17 >
29	BIT_MUX< 1 >	71	OUT_CHANNEL< 16 >
30	BIT_MUX< 2 >	72	OUT_CHANNEL< 15 >
31	BIT_MUX< 3 >	73	OUT_CHANNEL< 14 >
32	BIT_MUX< 4 >	74	OUT_CHANNEL< 13 >
33	GND	75	GND
34	DATA_SERIAL_OUT	76	OUT_CHANNEL< 12 >
35	DVDD	77	IBN_80u
36	DVSS	78	IBN_300u
37	DVDD_PAD	79	IBN_80u
38	DVSS_PAD	80	NC
39	NC	81	NC
40	NC	82	GND
41	GND	83	GND
42	GND	84	GND

Table B.1: Pin list of the packaged ASIC.

Bibliography

[1] P.L. Rossi et al. Imaging characterization of a multi-energy ct with quasi-monochromatic x-ray source. *Proceedings of IEEE*, MIC12M-7:2832–2835, 2011.

[2] M. Hoheisel et al. Advantages of monochromatic x-rays for imaging. *Proceedings of SPIE*, 5745:1087–1095, 2005.

[3] S. Masetti et al. Development of a multi-energy ct for small animals: Characterization of the quasi-monochromatic x-ray source. *IEEE Transactions on Nuclear Science*, 56:29–35, 2009.

[4] E. J. Harold and J. R. Cunningham. *The physics of radiology, fourth edition.* Charles C Thomas, 1983.

[5] R. Taleei and M. Shahriari. Monte carlo simulation of x-ray spectra and evaluation of filter effect using mcnp4c and fluka code. *Applied Radiation and Isotopes*, 67:266–271, 2009.

[6] M. R. Ay, M. Shahriart, S. Sarkar, M. Adib, and H. Zaidi. Monte carlo simulation of x-ray spectra radiology and mammography using mcnp4c. *Phys Med Biol*, 49:4897–4917, 2004.

[7] M. R. Ay and H. Zaibi. Development and validation of mcnp4c based monte carlo simulation for fan- and cone-beam x-ray ct. *Phys Med Biol*, 50(20):4863–4885, 2005.

[8] J. Sempau, J. M. Fernández-Varea, E. Acosta, and F. Salvat. Experimental benchmarks of monte carlo code penelope. *Nucl Instr and Meth in Phys Res B*, 207:107–123, 2003.

[9] X. Liovet, L. Sorbier, C. S. Campos, E. Acosta, and F. Salvat. Monte carlo simulation of x-ray spectra generated by kilo-electron-volt electrons. *J Appl Phys*, 93(7):3844–, Apr 2003.

[10] N. Jabbari et al. Comparison of mcnp4c and egsnrc monte carlo codes in depth-dose calculation of low energy clinical electron beams. *Journal of Physics D: Applied Physics*, 40:4519–4524, 2007.

[11] R. Jeraj et al. Comparisons between mcnp, egs4 and experiment for clinical electron beams. *Physics in Medicine and Biology*, 44(3):705–717, 1999.

[12] P.A. Love et al. Comparison of egs4 and mcnp monte carlo codes when calculating radiotherapy depth doses. *Physics in Medicine and Biology*, 43(5):1351–1357, 1998.

[13] R. Birch and M. Marshall. Computation of bremsstrahlung x-ray spectra and comparison with spectra measured with a ge(li) detector. *Phys Med Biol*, 24(3):505–517, 1979.

[14] D. M. Tucker. Semiempirical model for generating tungsten target x-ray spectra. *Med Phys*, 18(2):211–218, 1991.

[15] G. G. Poludniowski. Calculation of x-ray spectra emerging from an x-ray tube. part ii. x-ray production and filtration in x-ray targets. *Med Phys*, 34(6):2175–2186, 2007.

[16] A. Della Rocca et al. Computer simulation of the radiograohic image forming process: implementation and application. *NDT and E International*, 28(3):163–170, 1995.

[17] A. Malusek et al. Ctmod-a toolkit for monte carlo simulation of projections including scatter in computer tomography. *Comput Methods Programs Biomed*, 90:167–178, 2008.

[18] R. Fanti, V. Marzeddu and G. Massazza. A simulation tool to support teaching and learning the operation of x-ray imaging system. *Medical Eng and Phys*, 27:555–559, 2005.

[19] H. A. Kramers. On the theory of x-ray absorption and of the continuous x-ray spectrum. *Philos. Mag.*, 46:836–871, 1923.

[20] R. Whiddington. The transmission of cathode rays through matter. *Proc R Soc Lond A*, 86:360–370, 1912.

[21] G. G. Poludniowski and P. M. Evans. Calculation of x-ray spectra emerging from an x-ray tube. part i. electron penetration characteristics in x-ray targets. *Med Phys*, 34(6):2164–2174, 2007.

[22] M. Bontempi, L. Andreani, P.L. Rossi, and A. Visani. Monte carlo simulator of realistic x-ray beam for diagnostic applications. *Medical Physics*, 37(8):4201–4209, Aug 2010.

[23] R. Nowotny and A. Hyfer. Ein programm für die berechnung von diagnostischen roentgenspektren. *Fortschr Roentgenstr*, 142:685–689, 1985.

[24] P. Meyer, E. Buffard, L. Mertz, C. Kennel, and A. Constantinesco. Evaluation of the use of six diagnostic x-ray spectra computer codes. *Br J Radiol*, 77:224–230, 2004.

[25] M. Caon, G. Bibbo, Pattison J., and M. Bhat. The effect on dose to computed tomography phantoms of varying the theoretical x-ray spectrum: A comparison of four diagnostic x-ray spectrum calculating codes. *Med Phys*, 25(6):1021–1027, Jun 1998.

[26] M. Green and V. E. Cosslett. Measurements of k, l and m shell x-ray production efficiencies. *J. Phys. D: Appl. Phys.*, 1:425–436, 1968.

[27] E. Storm and H. I. Israel. *Nuclear Data Tables*, A7:565, 1970.

[28] T. R. Fewell, R. E. Shuping, and K. R. Hawkins. *Handbook of computed tomography x-ray spectra*. DHHS publication; no. (FDA) 81-8162. Rockville, Md; U.S. Dept. of Healt and Human Services, Public Healt Service, FDA, Bureau of Radiological Health, U.S. Governement Printing Office, Washongton D.C., 1981.

[29] M. Bhat and J. Pattison. Diagnostic x-ray spectra: a comparison of spectra generated by different computation methods with a measured spectrum. *Med Phys*, 25(1):114–120, Jan 1998.

[30] T. R. Fewell and R. E. Shuping. Photon energy distribution of some typical diagnostic x-ray beams. *Med Phys*, 4(3):187–197, May/Jun 1977.

[31] M. Bhat, J. Pattison, G. Bibbo, and M. Caon. Off-axis x-ray spectra: a comparison of monte carlo simulated and computed x-ray spectra with measured spectra. *Med Phys*, 26(2):303–309, Feb 1999.

[32] J. M. Boone and J. A. Seibert. An accurate method for computer-generating tungsten anode x-ray spectra from 30 to 140 kv. *Medical Physics*, 24(11):1661–1670, November 1997.

[33] M. Pelliccioni. *Fondamenti fisici della radioprotezione*. Pitagora Editrice Bologna, 1993.

[34] M. Green and V. E. Cosslett. The efficiency of production of characteristic x-radiation in thick targets of a pure element. *Proc. Phys. Soc.*, 78:1206–1214, 1961.

[35] A. Vignes and G. Dez. Distribution in depth of the primary x-ray emission in anticathodes of titanium and lead. *J. Phys. D: Appl. Phys.*, 1:1309–1322, 1968.

[36] N.A. Dyson. *X rays in atomic and nuclear physics*. Cambridge University Press, 1990.

[37] California Berkeley, editor. *X-Ray data booklet*. Center for X-ray optics advanced light source, Oct 2009.

[38] M. Gryzinski. Classic theory of atomic collisions. i. theory of inelastic collisions. *Physical Review*, 138(2A):A336–A358, 1965.

[39] H. Deutsch, P. Scheier, K. Becker, and Märk T. D. Revised high energy behavior of the deutsch-märk (dm) formula for the calculation of electron impact ionization cross sections of atoms. *International Journal of Mass Spectrometry*, (233):13–17, 2004.

[40] E. Casnati, A. Tartari, and C. Baraldi. An empirical approach to k-shell ionisation cross section by electrons. *J. Phys. B: At. Mol. Phys*, 15:155–167, 1982.

[41] C. Hombourger. An empirical expression for k-shell ionization cross section by electron impact. *J. Phys. B: At. Mol. Opt. Phys.*, 31:3693–3702, 1998.

[42] M.R. Talukder, S. Bose, and S. Takamura. Calculated electron impact k-shell ionization cross sections for atoms. *International Journal of Mass Spectrometry*, 269:118–130, 2008.

[43] C. H. Tang, Z. An, X. Q. Fan, and Z. M. Luo. An empirical formula of atomic k-shell ionization cross sections by electron impact. *Chin.Phys.Lett.*, 18(8):1053–1055, February 2001.

[44] M. Gryzinski. Two-particle collisions.ii. coulomb collisions in the laboratory system of coordinates. *Physical Review*, 138(2A):A322–A335, 1965.

[45] P. Cruz-Estrada F.J. Ramírez-Jiménez, L. Mondragón-Contreras. Application of pin diodes in physics research. In *AIP Conference Proceedings*, volume 857, pages 395–406, 2006.

[46] J.S. Benìtez-Read J.O. Pacheco-Sotelo F.J. Ramírez-Jiménez, R. Lòpez-Callejas. Considerations on the measurement of practical peak voltage in diagnostic radiology. *The British Journal of Radiology*, 921(77):745–750, September 2004.

[47] F. Rego and L. Peralta. Si-pin photodiode readout for a scintillating optical fiber dosimeter. *Radiation measurements*, 47:947–950, 2012.

[48] C.C. Bueno et al. Response of pin diodes as room temperature photon detectors. *Applied Radiation and Isotopes*, 61:1343–1347, 2004.

[49] G.F. Knoll. *Radiation Detection and Measurement, fourth ed.* Wiley, New York, 2010.

[50] I. Valais. A systematic study of the performance of the csi:tl single-crystal scintillator under x-ray excitation. *Nuclear Instruments and Methods in Physics Research A*, 571:343–345, 2007.

[51] J.R. Taylor. *An Introduction to Error Analysis: The Study of Uncertainties in Physical Measurements*. University Science Books, Sausalito, 1996.

[52] G. Baldazzi et al. X-rays spectroscopy with a portable compton selection chamber: detector design and results. *Nuclear Instruments and Methods in Physics Research B*, 213:223–226, 2004.

[53] P. Tothill. The ratio of k characteristic to total radiation emitted from a tungsten target x-ray tube. *J Phys D: Appl Phys*, 1(2):1093–1107, 1968.

[54] Z.B. Alfassi et al. On the elimination of the afterglow of csi(tl) scintillation detector. *Nuclear Instruments and Methods in Physics Research A*, 606:585–588, 2009.

[55] F.J. Ramírez-Jiménez et al. Considerations on the measurement of pratical peak voltage in diagnostic radiology. *The British Journal of Radiology*, 77:745–750, 2004.

[56] G. Zampa et al. Room temperature spectroscopic performance of a very-large area silicon drift detector. *Nuclear Instruments and Methods in Physics Research A*, 633:15–21, 2011.

[57] R. Campana et al. Imaging performance of a large-area silicon drift detector for x-ray astronomy. *Nuclear Instruments and Methods in Physics Research A*, 633:22–30, 2011.

[58] A.Vacchi et al. Performance of the ua6 large-area silicon drift chamber prototype. *Nuclear Instruments and Methods in Physics Research A*, 306:187–193, 1991.

[59] A. Rashevsky et al. Large area silicon drift detector for the alice experiment. *Nuclear Instruments and Methods in Physics Research A*, 485:54–60, 2002.

[60] C. Piemonte et al. Device simulation of the alice silicon drift detector. *Microelectronics Journal*, 37(12):1629–1638, 2006.

[61] S. Beolè et al. The alice silicon drift detectors: Production and assembly. *Nuclear Instruments and Methods in Physics Research A*, 582:733–738, 2007.

[62] E. Crescio et al. Results from beam tests of large area silicon drift detectors. *Nuclear Instruments and Methods in Physics Research A*, 539:250–261, 2005.

[63] E. Gatti and P. Rehak. Semiconductor drift chamber. an application of a novel charge transport scheme. *Nuclear Instruments and Methods in Physics Research A*, 225:608–614, 1984.

[64] M. Ahangarianabhari et al. Vega-1: A low-power front-end asic for large area multi-linear x-ray silicon drift detectors: design and first experimental characterization. to be published 2014.

Acknowledgments

I wish to thank my supervisor Prof. Giuseppe Baldazzi for his contribution to my personal and intellectual formation in the last three years of my life. His long-standing experience in this fascinating field along with his wisdom and guidance have allowed me to fill the gaps in my knowledge and find the strength, direction and purpose in my research.

I also wish to thank Dr. Claudio Labanti of the INAF/IASF in Bologna for his precious help in the experimental measurements.

I want to express my gratitude to the invaluable assistance of Dr. Marco Bontempi and of Dr. Pier Luca Rossi.

Finally, I acknowledge the help of my family, my friends and my colleague Luigi.